Time Calibration of IWCD: A new water Cherenkov near detector for Hyper-Kamkiokande

by

Jashanjot Kaur Brar

A Thesis submitted to the Faculty of Graduate Studies of

The University of Manitoba

in partial fulfillment of the requirements for the degree of

MASTER OF SCIENCE

Department of Physics and Astronomy

University of Manitoba

Winnipeg

ABSTRACT

This thesis has explored calibration of a new Intermediate Distance Water Cherenkov Detector (IWCD) for the long-baseline neutrino oscillation experiment from Tokai to Hyper-Kamiokande. The timing calibration method studied for water Cherenkov detectors uses a flash of light in the detector and can be applied in any water Cherenkov detector. The method accounts for the propagation of light from the source to the photomultiplier tubes, and accounts for the geometry of the detector, reaching a timing resolution of 0.01 ns using true time, and about 0.68 ns using digitized times. The thesis also describes measurements using the TRIUMF photomultiplier test facility of the first multi-photomultiplier tube module that will be used in IWCD.

ACKNOWLEDGMENTS

This thesis is written with the support of so many people. I am grateful to my supervisor, Blair Jamieson for providing extraordinary help and guidance during the journey of research. He always remained humble and calm while teaching and providing versatile approaches to the problem solving.

I am highly thankful to John Walker, postdoctral fellow at TRIUMF for being source of information and encouragement during research. He was always readily available for discussions about timing calibration studies and the possible tests that could be made for this approach.

The neutrino group at TRIUMF was very special to work with. They are an amazing group of genius, passionate scientists working on a new detector Hyper Kamiokande and Intermediate distance Water Cherenkov Detector (IWCD). I would like to thank everyone, in particular: Akira Konaka, Mark Scott, Thomas Lindner, Tom Feusels and Matej Pavin.

I am also thankful to the internship students who attended TRIUMF as part of their degree and worked at Photosensor Test Facility (PTF).

Thanks to Physics and Astronomy department and in particular, secretary Susan Beshta who provided incredible support and updated information about the official routines and fulfillment of requirements.

I am very thankful to my friends for constantly keeping me emotionally fit while living in different parts of the world.

I finally want to thank my (Brar) family for being so lovable and supportive while staying on the opposite side of the globe. My husband Sukhvir Singh Malhi remained a strong support and believed in me throughout. Special Thanks to my in-laws (Malhi) family. Finally, thank you to all my near and dear ones for providing me everything required to reach at this level.

TABLE OF CONTENTS

Page

LIST OF FIGURES

FIGURE Page

1. Introduction

1.1 Introduction

Among many questions in the vast field of physics, one of the main interests in particle physics today is to understand the composition of the universe. Ordinary matter described by the standard model of particle physics is being measured at ever increasing levels of precision. There is a mysterious matter which is part of the universe, that is invisible or unknown. This stuff that accounts for non-baryonic part of the universe is known as dark matter. Searching for dark matter is an interesting problem, however, it is not the main problem that can be studied by the T2K (Tokai to Kamioka) or the T2HK (Hyper Kamiokande) experiments.

T2HK will probe neutrinos for an antimatter/matter asymmetry. The Dirac equation suggests the amount of matter and antimatter to be equal in the universe [1]. In the big bang leptonic and baryonic matter and antimatter were in thermal equilibrium with radiation, causing a fully mixed dense state of matter and antimatter. Both matter and antimatter annihilated as the universe expanded. The difference found in the predicted amount of remaining matter in electroweak baryogenesis compared with the observed amount of baryonic matter in the universe is of nine orders of magnitude different [2]. The missing link is breaking the symmetry between matter and antimatter. Sakharov [3] postulated that the concentration of baryons observed today is dependant on three conditions: Violation of Baryon Number, Violation of C and CP, and conditions in which thermodynamics equilibrium does not hold. CP violation in neutrinos could explain why only matter remains in the present universe.

This introductory chapter will describe the particles in the standard model, followed by a history of neutrino and neutrino oscillation physics. This chapter will also give an overview of long-baseline neutrino experiments. Chapter 2 will describe the need for a new intermediate distance detector, its design, and motivation for investigating the timing calibration. Chapter 3 will detail the Photomultiplier Test Facility (PTF) measurements of the Super Kamiokande photomultiplier

tube (PMT). Also, it gives a brief description of the construction of the photomultiplier tube prototype. In chapter 4 the framework used to simulate water Cherenkov detectors will be examined. Chapter 5 will describe the method of studying the time calibration of water Cherenkov detectors. Finally, chapter 6 will give the results of the timing calibration.

The focus of this thesis is on developing a method for the time calibration of water Cherenkov detectors. Cherenkov detectors detect electromagnetic radiations which are produced when a charged particle moves faster than the speed of light in a medium, also known as cherenkov radiation. Cherenkov detectors are used to discriminate between a lighter particle and a heavy particle of the same energy and momentum, fast timing, and time of flight measurements of particles. This is completely dependent on the velocity of light in water. Using the time between when a flash of light is applied and a hit in a PMT is recorded, we can calculate the distance to where the Cherenkov light was produced. Properties of the water can change with time and location in the detector due to temperature and water quality variations. The timing measurement is affected by various processes that could occur due to the interaction of light with water, such as Rayleigh scattering, or Mie scattering.

1.2 Overview of the standard model of particle physics

The fundamental building blocks of known matter are arranged according to their properties, and interact via the four fundamental forces (strong nuclear force, electromagnetic force, weak force and gravitational force) as shown in Figure 1.1. The standard model classifies particles based on spin. The mediators of interactions are all bosons with integral spin, and building blocks of matter are all fermions with half-integral spin.

Bosons with spin 1 are the force carriers. In the standard model, force carriers are responsible for the transfer of force between quarks and leptons. Figure 1.2 shows a weak interaction with a W^- as the force carrier. In the strong force, Gluons are the mediators of strong nuclear forces. Z^0, $Z^\pm$ and $W^\pm$ bosons are the heavy particles that participate in weak interactions. Photons are the force carriers in electroweak interactions between charged particles. The Higgs boson is a spin 0 particle which interacts with all of the building blocks of all fundamental matter to give them mass.

Figure 1.1: The elementary particles of the Standard Model.

Elementary particles for the gravitational force are not part of the standard model. This is because there is no quantum description for gravity. Instead particles interact with gravity by the curvature of space time which is separately described by General Relativity.

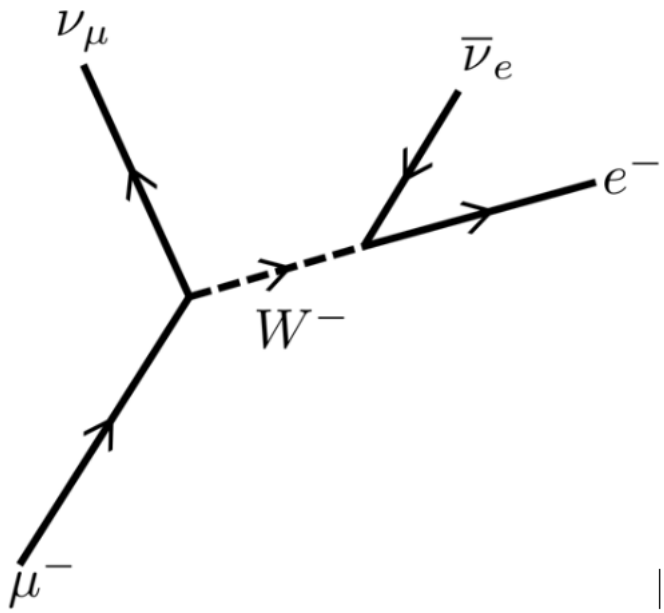

Figure 1.2: W^- boson is involved in the interaction between a muon and an electron anti-neutrino creating an electron and electron neutrino.

Fermions have a half-integral spin and are the building blocks of matter. Fermions are constrained by Pauli's exclusion principle, such that only one can be in a single particle state at a time. Fermions are categorized into quarks and leptons. Quarks, having an electric charge in units of 1/3 and 2/3 exist in six flavors: up, down, strange, charm, top, bottom. Gluons bind these in pairs of quarks and anti-quarks through strong forces to form mesons like pions or combine in a set of three to form baryons like protons and neutrons.

Leptons have an integral charge and interact through electromagnetic or weak interactions. There are 6 leptons in total (charged leptons - electron, muon and tau, and three neutral leptons - ν_e, ν_μ, and ν_τ). Three charged leptons and their antiparticles respectively as: electron and positron, muon and anti-muon, and tau and anti-tau. These have their corresponding neutrinos which forms the other part of lepton category being neutral leptons: ν_e, $\overline{\nu_e}$, ν_μ, $\overline{\nu_\mu}$, ν_τ, and $\overline{\nu_\tau}$. Neutrinos are produced in a given flavor that matches the charged lepton. For example, a positively charged pion decays into an anti-muon and a muon neutrino. Neutrinos, through their oscillations, have been deduced to have masses much smaller than that of the other particles in the standard model [4]. The oscillation of neutrinos is discussed in the section 1.4.

1.3 A brief history of neutrino physics

Neutrinos are neutral elementary particles, subject only to weak interactions (and even more weakly to gravity). Therefore, their detection requires detectors of a hundred tons. The neutrino was first hypothesized as a particle in 1930 by Wolfgang Pauli [5] to allow the law of conservation of energy in beta decay measurements to be upheld. Electrons were not mono-energetic in beta decay that suggested a three-body decay instead of two body decay and instead exhibit a continuous spectrum.

$$n \rightarrow p + e^- + \overline{\nu}_e.$$

Three-particle decay and other related problems were solved in 1932 with the discovery of the neutron by Chadwick [6]. Fermi incorporated the new particle into his theory of beta decay and named the third particle, neutrino, meaning 'little neutron' in Italian.

Neutrinos were first discovered in 1956 by Clyde Cowan and Fred Reines. They detected neutrons from the huge neutrino flux coming from the Savannah River nuclear power plant. They used inverse beta decay to detect the reactor electron anti-neutrinos:

$$\overline{\nu}_e + p \rightarrow e^+ + n, \text{followed by}$$
$$e^+ + e^- \rightarrow \gamma$$

They observed a delayed coincidence between an instantaneous positron capture, followed by a neutron capture several ms later. The newly developed technology of organic liquid scintillator next to a nuclear reactor proved to be a practical experiment. The detector was composed of water, doped with 40 kg of $CdCl_2$, and was instrumented with PMTs to observe the scintillation light produced. The $CdCl_2$ made it possible to observe a delayed coincidence signal between a positron annihilation and photons produced by neutron capture on cadmium, via the reaction:

$$n + {}^{112}_{48}Cd \rightarrow {}^{113}_{48}Cd + \gamma$$

The first observation of neutrinos won Reines the Nobel Prize in 1995.

Neutrinos exist in three leptonic flavours corresponding to the lepton names they couple to: electron-neutrinos (ν_e), muon-neutrinos (ν_μ), and tau-neutrinos (ν_τ). Neutrinos can be produced by nuclear reactions in the stars like sun, nuclear reactors on the Earth, during a supernovae, accelerated particle beams, cosmic rays, etc.

1.4 Neutrino oscillations

Neutrino oscillations are quantum mechanical transitions from one flavour to another $\nu_\alpha \leftrightarrow \nu_\beta$ $(\alpha, \beta = e, \mu, \tau)$ where α and β distinguish the different leptonic flavours.

Neutrino oscillations were first observed in atmospheric neutrinos and then in solar neutrinos. Solar ν_e are produced through fusion reactions in the Sun. In 1968, Ray Davis performed the first experiment to measure solar neutrinos. The overall rate of solar neutrinos was found to be

about 30% that of the expected flux [7]. The idea of neutrino mixing emerged around the time of discovery of muon neutrinos in a paper by Maki, Nakagawa and Sakata [8]. In 1969 Gribov and Pontecorvo developed a theory for neutrino flavor oscillations [9]. Their theory suggested that the neutrinos traveling from sun change into a different flavor to which Davis' experiment was insensitive. This discrepancy was observed in other experiments like the GALLAX [10] and Sage experiments [11] which captured neutrinos on gallium and germanium, respectively. The water Cherenkov detector Kamiokande was one of the experiments to observe the defect of solar neutrinos [12][13].

The discrepancy in solar neutrinos was solved by the SNO experiment. This experiment could detect all three flavours of neutrino interactions from solar neutrinos, i.e. Charged current interactions (ν_e only), neutral current interactions (ν_e, ν_μ, ν_τ) and elastic scattering (mainly ν_e, some $\nu\mu, \nu_\tau$). The SNO experiment observed neutral and charged current interactions, which made it possible to measure the total neutrino flux of solar neutrinos, independent of neutrino flavor [14].

Neutrino oscillations are detected in two ways:

1. Appearance - When a flavor of neutrino which should not be present in a source of neutrino is detected. For example - P($\nu_\mu \rightarrow \nu_e$) These types of experiments are particularly sensitive to mixing angles.

2. When an initial flux of neutrinos disappears from a beam before detection. The design of these experiments shows sensitivity to small energies and thus small mass values. T2K uses P($\nu_\mu \rightarrow \nu_\mu$).

Each flavor of a neutrino is a quantum superposition of three mass states. The theory for neutrino oscillations is explained quantum mechanically. Neutrinos have mass states $\mid \nu_i\rangle$ for i=1,2,3, and flavor states $\mid \nu_j\rangle$ for j=e, μ, τ. The neutrino flavor states are a coherent superposition of different neutrino mass states and are related by a unitary matrix U as:

$$\mid \nu_j\rangle = \sum_i U^*_{ji} \mid \nu_i\rangle, \tag{1.1}$$

and its inverse as:

$$\mid \nu_i\rangle = \sum_j U_{ij}^{\dagger} \mid \nu_j\rangle \tag{1.2}$$

$$= \sum_j U_{ji}^{*} \mid \nu_j\rangle \tag{1.3}$$

where $U^{\dagger}U$ = 1.

The transition from a definite flavor state to mixed flavor state gives rise to neutrino oscillations. If j is the initial flavor at (x, t) = (0, 0), then probability of measuring another flavor k at (x, t) is given by:

$$P(\nu_j \rightarrow \nu_k) = \mid \langle \nu_k \nu_j(x,t)\rangle \mid^2, \tag{1.4}$$

where we have set $\hbar$= c = 1

The time dependence $e^{-i(E_i t)}$ of the eigenstates evolved over time, and is given by the time dependent Schrodinger equation:

$$\mid \nu_j(x,t)\rangle = \sum_i U_{ji}^{*} e^{-i(E_i t - p_i x)} \mid \nu_j\rangle. \tag{1.5}$$

The probability can be written as:

$$P(\nu_j \rightarrow \nu_k) = \left| \sum_i \sum_l \langle \nu_l \mid U_{kl} U_{ji}^{*} e^{-i(E_i t - p_i x)} \mid \nu_j\rangle \right|^2 \tag{1.6}$$

$$= \left| \sum_i U_{ki} U_{ji}^{*} e^{-i(E_i t - p_i x)} \right|^2 \tag{1.7}$$

$$= \sum_i \sum_l U_{ki} U_{ji}^{*} U_{kl}^{*} U_{jl} e^{-i((E_i - E_l)t - (p_i - p_l)x)}. \tag{1.8}$$

The momentum of ith mass-state of the neutrino in terms of energy is:

$$p_i = \sqrt{E_i^2 - m_i^2} \tag{1.9}$$

$$= E_i\left(1 - \frac{m_i^2}{E_i^2}\right)^{\frac{1}{2}}. \tag{1.10}$$

The neutrino's mass is much less than its momentum, which allows this expression to be approximated by Taylor expansion, giving:

$$p_i \approx E_i + \frac{m_i^2}{2E_i}. \tag{1.11}$$

Neutrinos are ultra-relativistic particles. Neutrinos of different mass having initial energy E travel a distance L in approximately the same time t. Using eq. 1.8, the oscillation probability can be thus written as:

$$P(\nu_j \to \nu_k) = \sum_i \sum_l U_{ki} U_{ji}^* U_{kl}^* U_{jl} e^{\frac{-i\Delta m_{ji}^2 L}{2E}}, \tag{1.12}$$

where $\Delta m_{ji}^2 = m_i^2 - m_j^2$ is the difference in the mass-squared of the ith and jth mass states.

By expanding these the probability of neutrino oscillation is given by:

$$\begin{aligned} P(\alpha \to \beta) =& \mid \langle \nu_\beta(x) \mid \nu_\alpha(0) \rangle \mid^2 \\ &= \delta_{\alpha\beta} - 4\sum_{i>l} Re[U_{\beta i} U_{\alpha i}^* U_{\beta j}^* U\alpha j] sin^2\left(\frac{\Delta m_{ij}^2 L}{4E}\right) \\ &+ 2\sum_{i>l} Im[U_{\beta i} U_{\alpha i}^* U_{\beta j}^* U_{\alpha j}] sin\left(\frac{\Delta m_{ij}^2 L}{2E}\right). \end{aligned} \tag{1.13}$$

The oscillation probability depends on the differences in the square of the masses. The probability for anti-neutrino oscillation is the same, except that the sign of the last term of eq. 1.13 is flipped. The imaginary component in the mass matrix causes a charge-parity (CP) violation in leptons.

U is called the Pontocorvo-Maki-Nakagawa-Sakata(PMNS) matrix and is written as the product of three unitary transformations which is parameterized by three mixing angles $(\theta_{12}, \theta_{13}, \theta_{23})$, and one overall phase (δ_{CP}). The PMNS matrix is:

$$U = \begin{pmatrix} e1 & e2 & e3 \\ \mu 1 & \mu 2 & \mu 3 \\ \tau 1 & \tau 2 & \tau 3 \end{pmatrix} = \begin{pmatrix} 1 & 0 & 0 \\ 0 & c_{23} & s_{23} \\ 0 & -s_{23} & c_{23} \end{pmatrix} \begin{pmatrix} c_{13} & 0 & s_{13}e^{-i\delta_{CP}} \\ 0 & 1 & 0 \\ -s_{13}e^{i\delta_{CP}} & 0 & c_{13} \end{pmatrix} \begin{pmatrix} c_{12} & s_{12} & 0 \\ -s_{12} & c_{12} & 0 \\ 0 & 0 & 1 \end{pmatrix}, \tag{1.14}$$

where $c_{ij} = \cos(\theta_{ij})$ and $s_{ij} = \sin(\theta_{ij})$, for i, j = 1, 2, 3 and δ_{CP} is responsible for CP violation. A matrix of Majorana phases is left off as it does not affect the oscillations. Originally θ_{23} in first term was measured using atmospheric neutrinos, but now measurements can also be made using accelerator produced neutrinos. In the second term θ_{13} could be measured using reactor neutrinos and neutrinos produced at accelerator. Solar and reactor neutrinos measure θ_{12}. The mass splittings can be described by taking differences in two mass states. For example $\Delta m^2_{31} = \Delta m^2_{21} + \Delta m^2_{32}$.

The probability of finding an electron neutrino in a beam comprised of muon neutrinos can be approximated as:

$$\begin{aligned} P(\nu_\mu \to \nu_e) \approx & \sin^2(2\theta_{13})\sin^2(\theta_{23})\sin^2\left(\frac{\Delta m^2_{31} L}{4E}\right) \\ & + \sin(2\theta_{12})\sin(2\theta_{23})\cos(\theta_{13})\sin\left(\Delta\frac{m^2_{21} L}{4E}\right)\sin\left(\frac{\Delta m^2_{31} L}{4E}\right) \\ & \times \left[\cos\left(\frac{\Delta m^2_{32} L}{4E}\right)\cos\delta_{\text{CP}} - \sin\left(\frac{\Delta m^2_{32} L}{4E}\right)\sin\delta_{\text{CP}}\right] \\ & + \text{solar and matter effect terms.} \end{aligned} \tag{1.15}$$

Some ν_μ disappear from the initial neutrino flux because they have oscillated into other neutrino flavors. The probability of finding a given ν_μ after travelling a distance L with energy E is:

$$\begin{aligned} P(\nu_\mu \to \nu_\mu) \approx & 1 - [\cos^2(\theta_{13})\sin^2(2\theta_{23}) + \sin^4(\theta_{23})\sin^2(\theta_{23})]\sin^2\left(\frac{\Delta m^2_{32} L}{4E}\right) \\ & + \text{solar and matter effect terms.} \end{aligned} \tag{1.16}$$

Neutrino oscillations are also affected by neutrino interactions with the matter through which neutrinos pass. For instance, solar neutrinos pass through part of the sun, Earth's atmosphere and Earth's crust to reach a detector. Neutral current interactions can happen for all flavors when interacting with matter. These give an overall phase shift, which can be factored out. Charge current interactions can only occur for electron neutrinos because matter contains electrons and not muons and taus. Oscillation probabilities in matter depend on mass squared differences, $\Delta \mathrm{m}^2$, which are sensitive to the mass hierarchy. Thus atmospheric neutrinos in Super-Kamiokande are sensitive to mass hierarchy, as neutrinos traveling through the earth have more possibilities to interact than those that come from directly overhead.

1.5 Long-baseline neutrino experiments

To understand neutrino oscillations better, neutrinos are studied from all sorts of sources. The sensitivity of a particular neutrino experiment is determined by the neutrino mass splitting squared, neutrino energy and the distance to the detector L by satisfying the condition $\Delta m^2 \frac{L}{E} \gtrsim 1$, one mass squared mass difference. Usually, a broad energy spectrum of neutrinos is used to detect the oscillations by observing the distortion of the energy distribution. For solar neutrino experiments ($\mathrm{L} \simeq 10^{11}$ m, $\mathrm{E} \lesssim 15$ MeV), for atmospheric neutrinos ($2 < \mathrm{L} < 10000$ km, $\mathrm{E} \simeq 1$ GeV), for reactor neutrino experiments (L $\simeq$ 10-100,000 m, E $\simeq$ 3 MeV), and for accelerator neutrino experiments (L $\gtrsim$ 500 km, E $\simeq$ 1 GeV), the sensitivity ranges of the above h/E values are $\Delta \mathrm{m}^2 \gtrsim 10^{-10}, 10^{-4}, 10^{-5}$ and 10^{-3} eV^2, respectively [15]. Neutrino interaction cross sections are small, thus the event rate per ton of detector is very low. Signal and background characteristics rely on shielding from cosmic ray muons coming from the atmosphere, which is done by placing detectors deep underground. Often an active shielding of the outer detector is also used to veto events coming from outside of the detector. These techniques are currently used in various detectors worldwide.

1.5.1 Current program: Tokai to Kamioka

To confirm the observation of unusually large neutrino mixing in the atmospheric oscillations, accelerator neutrino experiments with neutrino beam of high purity and tuneability was required.

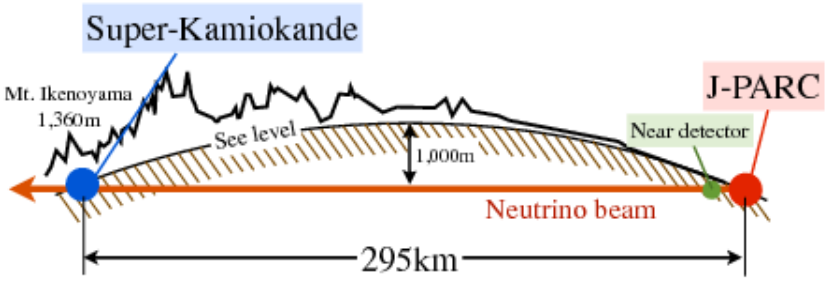

Figure 1.3: T2K experiment, where a neutrino beam starts at J-Parc, passes through the near detector on its way towards Super-Kamiokande at Mt. Ikenoyama. Figure from [16]

.

The T2K experiment was originally built to measure the mixing angle θ_{13} and to make a precision measurement of θ_{23}. Once the angle θ_{13} was determined the goal of T2K has been to search for δ_{CP}. T2K [17] is one of the experiments in which the disappearance of muon neutrinos was observed with a laboratory-produced beam. T2K is also the first experiment to observe the appearance of the flavor of ν_e from a beam with a different flavor (ν_μ). The T2K experiment uses a 30 GeV proton beam from J-PARC (Japan Proton Accelerator Research Complex) accelerator facility as shown in figure1.3. T2K consists of a muon neutrino beamline, near detector complex (ND280), and a far detector, Super Kamiokande.

ND280 is located 280 m downstream of the neutrino production target and measures the neutrino beam before oscillation. Figure 1.4 shows the off-axis near detector ND280. The detector is composed of a central tracker region with Fine-Grained Detectors (FGDs) [18] that are surrounded by three time projection chambers (TPCs) [19]. FGDs are the primary target for neutrino interactions and contains planes of plastic scintillator bars, that provide a carbon interaction target. Charged particles produces tracks of ionization in the TPCs. The TPCs allow charge particles to be tracked, and energy deposited allows for e/μ particle ID. TPCs and FGDs are surrounded by barrel ECALs and a magnet. The π^0 detector (P0D) is used to measure neutral current single π^0 cross section. An electromagnetic calorimeter (ECAL) is placed downstream of the tracking detectors surrounding the P0d, TPC and FGD. Scintillator bars act as a side muon range detector (SMRD).

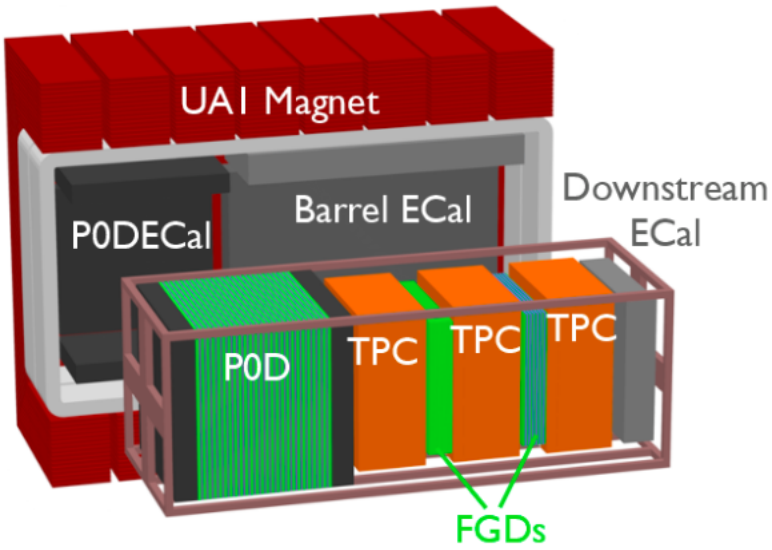

Figure 1.4: Visual of ND280 off-axis near detector. It shows the TPCs (Time projection chambers) in orange, the FGDs (Fine grained detectors) in green, π^0 detector(P0D), the electromagnetic calorimeter and the UA1 magnet yoke and solenoid coils with muon range detectors surrounding the inner detector. Figure from [20]

Super Kamiokande is a 50 kt water Cherenkov detector located at a baseline distance of 295 km, which samples the oscillated neutrino beam. To obtain a narrow energy spectrum beam with maximum at 0.6 GeV [21], and width of $\sim$ 0.3 GeV, the direction of beam is aimed off-axis by 2.5° [22]. This technique maximizes the ν_μ oscillation (disappearance) for the 295 km baseline which provides the best determination of $\sin^2 2\theta_{23}$.

The distribution of reconstructed muon neutrino energy, and anti-muon neutrino energy at the far detector for the data collected from January 2010 to May 2017, and best-fit Monte Carlo calculations are shown in Fig. 1.5.

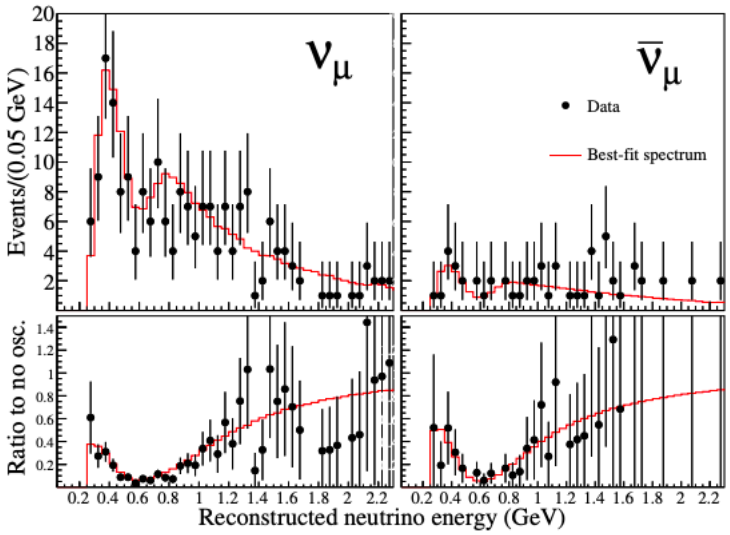

Figure 1.5: Reconstructed neutrino energy distribution at the far detector for the ν_μ CCQE (left) and $\overline{\nu}_\mu$ CCQE (right) -enriched samples with the total predicted event rate shown in red [23].

Similarly, reconstructed energy for the ν_e, $\overline{\nu}_e$, and ν_e CC1π^+ samples are compared to Monte Carlo predictions, as shown in Fig. 1.6. These ν_e events represent the first observation of neutrino appearance.

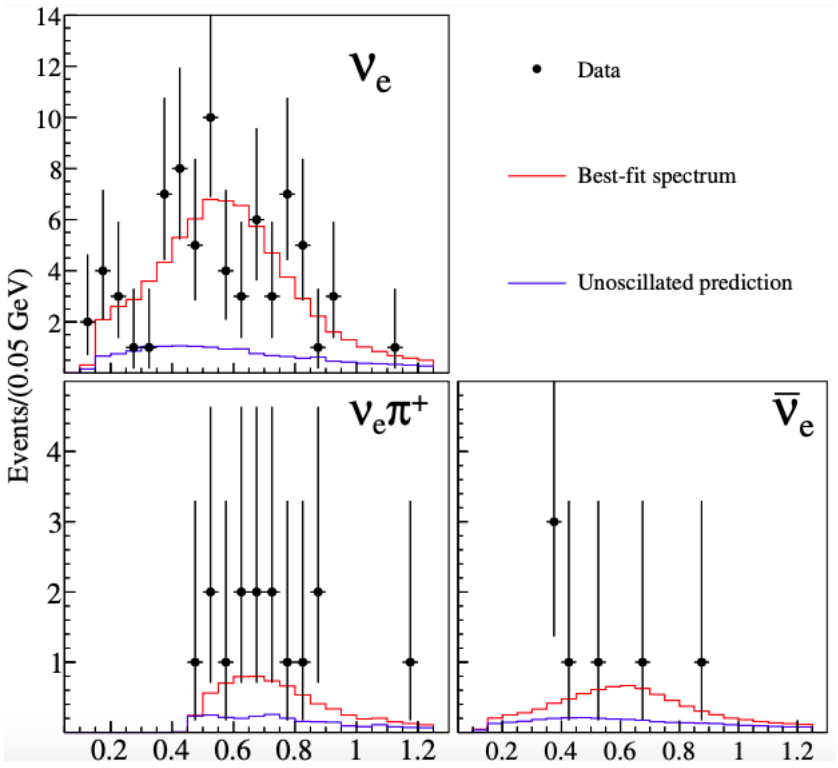

Figure 1.6: Reconstructed neutrino energy distribution at the far detector for the ν_e CCQE (top left), ν_e CC1π^+ (bottom left), and $\overline{\nu}_e$ CCQE (bottom right) -enriched samples. Prediction under the no oscillation hypothesis are shown in blue and best-fit spectra in red [23].

1.5.2 Future program: Tokai to Hyper-Kamiokande

To improve the sensitivity of neutrino physics experiments, new facilities are proposed. In Japan, there are two new proposed detectors, IWCD, and Hyper-Kamiokande (Hyper-K). Hyper-K will serve as a far detector. It will be capable of precision measurements of neutrino oscillation parameters and probe for CP-violation in the lepton sector [24]. Hyper-K is a 260 kton version of Super-K with 8 times the fiducial mass of ultra-pure water. Hyper-K is about 8 times larger in mass, placed about 8 km south of Super-K at an underground depth of 1,750 meters water equivalent (m.w.e.) [24]. It will extend the sensitivity to nucleon decays. It will also study solar neutrinos, supernovae burst neutrinos and supernovae relic neutrinos. IWCD will act as a probe for sterile neutrino oscillations with measurements for multiple energy spectra [25]. This is further elaborated upon in chapter 2.

2. The Intermediate Distance Water Cherenkov Detector for Hyper-Kamiokande

To get more precise measurements of neutrino oscillations, long-baseline neutrino experiments will be required to reduce the effect of the theoretical uncertainties. Current experiments relate experimental observables to the incident neutrino energy which rely on theoretical models of neutrino-nucleus interactions. A new Intermediate Distance Water Cherenkov Detector (IWCD), previously called nuPRISM and E61 will address these uncertainties when Hyper-Kamiokande is collecting data. The IWCD will reduce flux and cross-section uncertainties in the HK oscillation analysis by measuring neutrino properties in the same nuclear target as the far detector. The IWCD will observe the charge current ν_μ interactions over a range of off-axis angles from 1° to 4°. The IWCD will measure the lepton kinematics for the same neutrinos flux spectrum, which largely removes neutrino interaction modeling uncertainties from T2K oscillation measurements. The IWCD makes measurements of neutrino cross-section, and measurements of neutral current interactions as a function of neutrino energy on the water possible. The IWCD is also a sensitive probe of sterile neutrino oscillations with multiple energy spectra.

2.1 Motivation for a new near detector

T2K experiment has collected $\sim 3\times10^{21}$ protons on target and published the world's most precise measurement of θ_{23} [25]. To get more precise measurements of ν_e appearance and ν_μ disappearance, more data is required to reduce the statistical uncertainties. By the time Hyper-Kamiokande starts to collect data, measurements will be limited by neutrino interaction systematic uncertainties.

The present experiments rely on neutrino interaction generators to translate the experiment's observables into constraints on the neutrino energy spectrum, which depend on the value of the oscillation parameters. Some of the backgrounds at the far detector, Super-Kamiokande (Super-K), are poorly constrained at existing near detector ND280. Measurement of ν_μ, π^+ interactions in

water with IWCD could help understand event reconstruction uncertainties and the expected rate for the interaction at Super-K.

Calculating the energy of the incident neutrino from the lepton kinematics is the least constrained component in neutrino interaction measurements. Currently the largest systematic uncertainty in T2K is an experimentally-unconstrained nuclear binding energy parameter with a potentially large bias in the ability to translate lepton kinematics to neutrino energy. Charged pions undergo a two-body decay-in-flight to form a conventional neutrino beam. Moving to further beam axis angles, the neutrino energy spectrum narrows and peaks at lower energies. This is called the "off-axis" effect. IWCD takes advantage of the energy dependence of the neutrino flux and these measurements will provide a constraint on the relationship between lepton kinematics and neutrino energy by measuring final state muons at different off-axis angles over a continuous range from 1 to 4 degrees.

The dynamics of charge-current quasi-elastic (CCQE) interactions ($\nu_\mu + n \rightarrow \mu^- + p$), when the target neutron is converted into an outgoing proton are summarized in a set of three vector and three axial vector form factors. The vector form factors are tightly constrained from external electron and pion scattering experiments [26]. The axial-vector form factor has the largest remaining uncertainty, which is often modelled as having a dipole form,

$$F_A(Q^2) = \frac{F_A(0)}{(1 + \frac{Q^2}{M_a^2})^2}. \tag{2.1}$$

The parameter $F_A(0)$ is precisely known from nuclear beta decay, which leaves M_A as the remaining uncertain parameter. Modifying M_A simultaneously alters both the overall CCQE cross-section and the shape of the Q^2 distribution.

The reaction mechanism in electron scattering is different due to the absence of an axial-vector current component. In neutrino scattering experiments with broadband beams, we must rely on the model predictions to extract neutrino energy for any given event. Measurements of the hadronic final state are not precise because these are limited by a lack of theoretical understanding of the expected hadron kinematics for multi-nucleon events. Also, the nuclear effects modify the final

state hadron spectra for CCQE, which are not well understood so far.

Other than multi-nucleon effects, other effects such as long-range correlations and final state interactions within the target nucleus can also produce distortions to the neutrino energy spectrum that can be difficult to model [25].

2.1.1 Current Near Detector: ND280 capabilities and limitations

Constraints on flux and cross-section model parameters from ND280 are used in T2K oscillation analyses. Uncertainty on the predicted number of electron neutrinos at the far detector is 3.2% when using data from ND280 to constrain the flux and cross-section parameters, i.e. flux and cross-section. The remaining uncertainty of 4.7% is due to unconstrained cross-section parameters.

Near detector, analyses have thus far used interactions in the most-upstream Fine-Grained Detector (FGD1), which is composed of carbon and hydrogen. As FGD1, is composed entirely of alternating layers of horizontally- and vertically- oriented scintillator bars, it cannot directly probe interactions on oxygen. FGD2 contains water layers interspersed within its scintillator layers. A simultaneous fit on both FGDs can provide a constraint on nuclear uncertainties in oxygen, and may potentially reduce the corresponding nuclear model uncertainties.

ND280 requires to extend the phase space over which it can measure the outgoing lepton kinematics from a charge-current neutrino interaction. Currently, muons are required to be produced in an FGD and travel a minimum distance through the downstream TPC to measure both muon momentum and be identified as muons. This limits the muon acceptance to forward angles. Improving detector timing calibration and track matching to the Electromagnetic Calorimeters and Side Muon Range Detectors surrounding the FGDs and TPCs will allow reconstructing charged-current events with backward going and sideways-going muons. These additional samples may be able to improve constraints on the cross-section modeling.

Charged current interactions in the Pi-Zero Detector (P0D) are yet not included in the oscillation analysis. P0D can measure the event rate with and without water targets dispersed throughout, and thus can extract constraints on interactions in water is possible. The larger fiducial volume of the P0D produces a higher event sample. It is necessary to choose a neutrino interaction model that

can characterize all possible variations of the neutrino cross-sections as a function of both neutrino energy and final state particle kinematics to reduce systematic uncertainties. To further reduce uncertainties in neutrino cross-section interactions systematic uncertainties due to neutrino-nucleus interactions, measurements better than their their current level are required.

2.2 The IWCD design

The IWCD detector is a proposed water Cherenkov detector around 1 km or 2 km from the T2K neutrino beam production point. It will be a 50 m tall cylindrical volume filled with water with a diameter of 10 m. Good water quality will be maintained in the detector to allow the light generated by physics processes to propagate long distances with minimal attenuation and scattering allowing event vertices to be precisely reconstructed [25]. The water will be doped with gadolinium [27]. The neutron capture cross-section of gadolinium is much greater than the neutron capture of hydrogen. An excited state of gadolinium is produced by neutron capture, and promptly decays by emitting a cascade of gamma rays, which is visible in the water Cherenkov detector [27]. An example of an anti-neutrino interacting with a proton is shown in Figure 2.1. The detector will span an off-axis range of (1-4)°, and its diameter is large enough to contain muons with momenta up to 1 GeV/c.

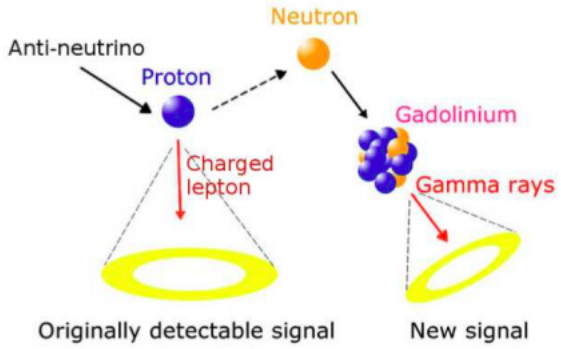

Figure 2.1: Anti-neutrino interaction followed by the capture of the produced neutron on gadolinium [27].

The inner detector contains 3-inch multi photomultiplier tubes (mPMT) placed inside a transparent pressure vessel along with with their readout electronics. The electronics in the mPMT modules in Hyper-K and IWCD will be the same. By having electronics closer to the PMTs, the number of feedthroughs and cables needed to readout the detector is reduced. The electronics will send information about all of the hits from a single mPMT module to the backend electronics. This detector can raise and lower the instrumented section of the tank to span the full off-axis range. The movement of the detector to the large off-axis angles relative to the beam direction lowers the peak energy of the neutrino energy spectrum and reduces the number of neutrinos in the high-energy tail. Fig. 2.2 represents the neutrino energy spectra at several different off-axis angle span over (1-4)$^{\circ}$ for IWCD detector.

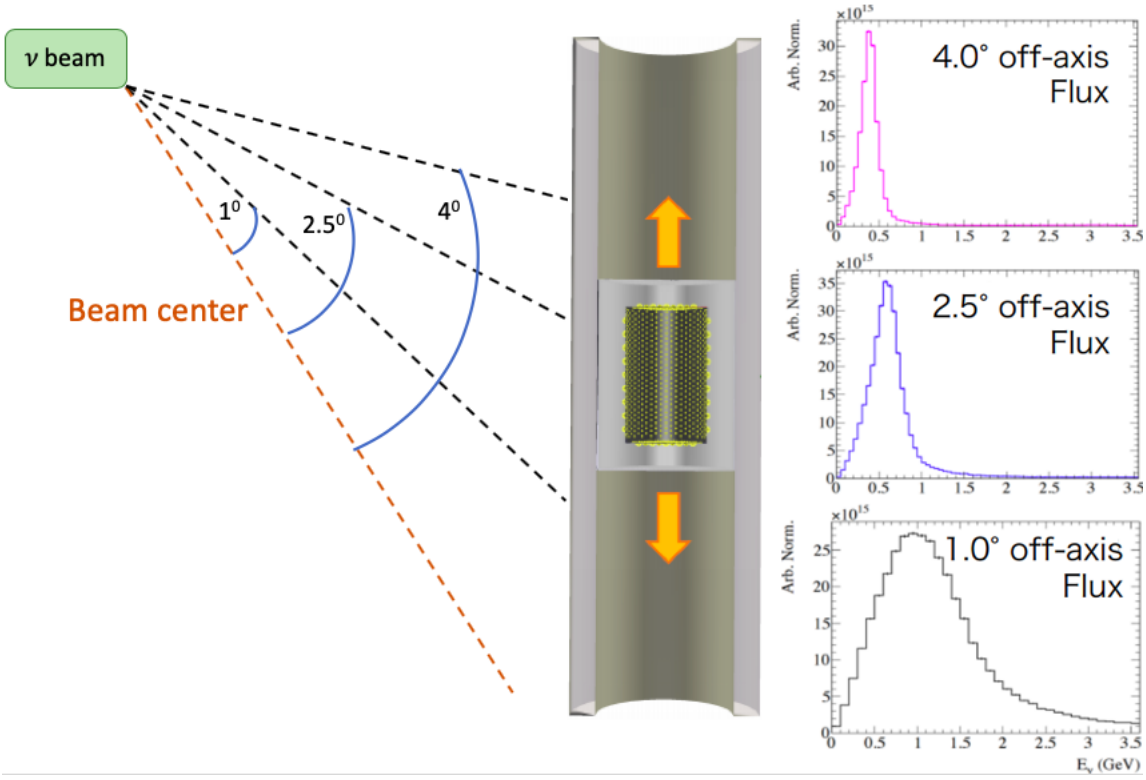

Figure 2.2: Neutrino energy spectra at three different off-axis angles between 1-4° [25].

IWCD provides a water target, identical signal and background interaction modes as at Super-

K, a 4π solid angle acceptance, and a smaller error on the flux extrapolation from the near to the far detector [27].

This detector is designed to reduce systematic uncertainties on the T2K oscillation analysis. It does so by constraining ν_μ flux and cross-section on water. Also it provides lepton kinematics template for a given ν_μ energy for each event selection. The IWCD will also constrain electron neutrino cross-sections, making the first-ever energy-dependent neutral current (NC) and charge current (CC) cross-section measurements. The IWCD will allow HK to not rely on neutrino generators to provide incident neutrino energy.

2.3 The multi-photomultiplier tube design for IWCD

Photomultiplier tubes are the vacuum tubes which are very sensitive light detectors. To detect high-energy particles that result from neutrino interactions, the detector exploits a phenomenon known as Cherenkov radiation. Charged particles traversing at speeds faster than light in water radiate light in a conical pattern around the direction of the track. This light eventually falls on the inner wall of the detector, which is covered with PMTs. These PMTs measure the amount of light reaching them and the time of arrival, which helps to reconstruct the energy and starting position of the particles.

IWCD detector uses 3-inch PMTs in multi-PMT modules to ensure higher resolution timing measurements, and finer granularity for the shorter light propagation distances. This allows the Cherenkov rings to be imaged with better resolution, and thus reconstruction improvements are expected. Smaller PMTs have better timing resolution for event reconstruction. Reflectors and PMT orientation might provide additional directional information. These PMTS have a lower dark noise rate which improves vertex resolution and directionality. Improved vertex resolution with mPMTs would allow a lower threshold for the low-energy trigger. The PMTs are embedded in a module in a hexagonal array. The Inner Detector (ID) consists of 19 PMTs and the outer detector (OD) has 7 PMTs. Having the PMTs in modules reduces cabling, allows simpler installation of smaller PMTs in a detector. Also, these modules protect the PMTs with an acrylic dome.

The multi-PMT module is assembled in a vessel with a stainless steel ring and back-plate.

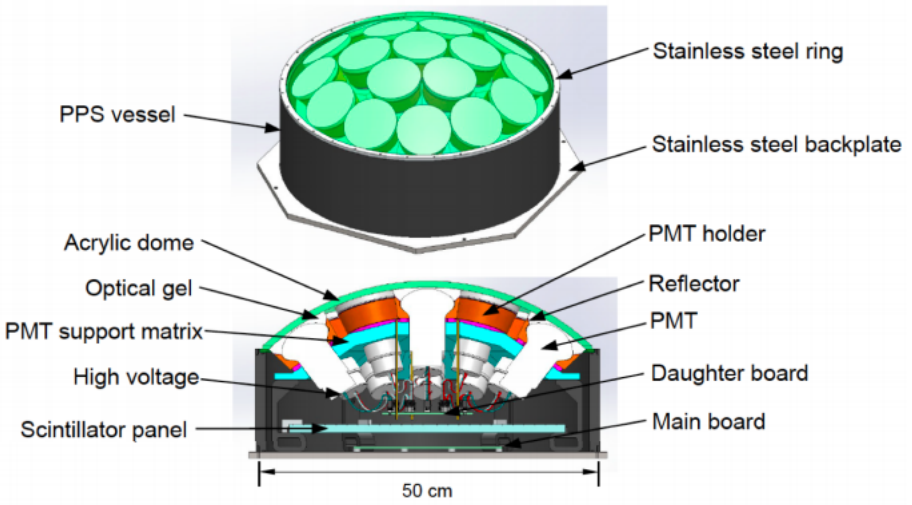

Figure 2.3: mPMT module and its components. [Source: TRIUMF neutrino group]

The PMTs are held in a PMT support matrix. The PMTs are covered with optical gel and are surrounded by reflectors. Integrated high voltage is supplied from the bottom of the PMTs and is connected to a daughter-board. The scintillator is between the PMTs and the main board. The mPMT assembly and components are shown in Figure 2.3.

The PMTs are covered with gel on the top to create a smooth contact between 3-inch PMT and acrylic dome. The aluminum reflectors give an effective increase in photosensor are of 20%. Finally, the multi-PMT modules improve the timing resolution over use of a single PMT, which helps resolve inter-bunch pileup.

2.4 Motivation for investigating the timing calibration

The sensitivity of future experiments to CP violation depends on the control of systematic uncertainties. Next-generation experiments like Hyper-Kamiokande (Hyper-K) [28] require systematic uncertainties on their far detector event rate production to be less than T2K experiment [29]. To reduce the detector uncertainties requires bottom-up calibration for detector systematic uncertainty estimation in both the near and far detector. Achieving a precision bottom-up detector calibration requires measurement of the basic detector performance such as: the photosensor response, absorption/scattering in the water, and light reflection on the wall. Bottom-up calibration

can reduce the largest detector uncertainty which is the angular response of the PMTs. To study the uncertainty, a photosensor test facility was built at TRIUMF, Canada's national particle accelerator center in Vancouver. This facility can study the photosensor response by injecting laser light at a different angles and positions using a robotic gantry arm. This is discussed in more detail in Chapter 3.

The timing calibration determines the size of the vertex resolution, which then affects how well the fiducial volume can be defined. The fiducial volume goes into any calculation of the number of nuclei that neutrinos could interact for cross-section or flux-times-cross-section measurements.

2.5 Concluding remarks

Systematic uncertainties estimated for long-baseline oscillation experiments in the present era have a noticeable effect on the achievable precision. To measure Charge-Parity Violation (CPV) in the lepton sector systematic uncertainties are required to be further reduced and understood. The proposed IWCD can address many of the shortcomings of the present near detector, can act as a probe of short baseline neutrino oscillations, and can provide unique measurements of neutrino scattering.

3. The photosensor test facility measurements at TRIUMF

Physics experiments require a detailed understanding of systematic uncertainties. Detector systems including photomultiplier tubes to detect Cherenkov light from neutrino interactions need to have their individual responses accurately measured. The Super-K detector contains 11,000 photomultiplier tubes and the Hyper-K detector will contain up to 90,000 photomultiplier tubes in two water tanks. Thus a study of the individual PMTs is necessary to accurately simulate, model and understand the large-scale behavior of the detectors and the data they collect. Such a facility the Photosensor Testing Facility (PTF) is in operation at TRIUMF, Canada's National Laboratory for nuclear and particle physics in Vancouver.

3.1 The photosensor test facility at TRIUMF

Photosensor test facility (PTF) at TRIUMF is focused on the study of the PMTs used in SK and the proposed IWCD. The currently operating far detector for T2K is Super-K, which includes 11,000 20-inch PMTs. The first measurements at the PTF were conducted to study the 20-inch PMTs used in SK, but it is capable of measuring the response of a wide range of photomultiplier tubes of various sizes. The PTF involves the use of the hardware which is accessible through a software interface that can be accessed through a webpage hosted on one of the local computers at TRIUMF.

A number of equipment actively participate in taking scans to record data.

The PMTs under test are scanned to record their behavior. The principle for the operation of the PMTs is the photoelectric effect, which means photoelectrons are emitted when photons are incident on the surface. The liberated photoelectrons are accelerated and multiplied using an electron multiplier to produce an output signal. From the photocathode the electron(s) are focused onto the dynodes and are collected at the anode to produce the output signal.

The gantry is a servo-driven system capable of motion in 5 axes (x, y, z, θ (rotation), ϕ(tilt)). The PTF consists of two independent gantry systems capable of simultaneous motion across the

PMT surface (Gantry 0 and Gantry 1) used to move and aim the optical boxes. Stepper motors are used to control the movement of the gantry system.

The optical box contains both the monitor and receiver PMTs, laser, polarizer, collimator, beam splitter, the phidget accelerometer and the magnetometers. One optical box is mounted on each gantry. Optical Box 0 and Optical Box 1 are mounted to Gantry 0 and Gantry 1 respectively.

Six coils as 3 pairs of Helmholtz coils of wire are arranged along the three axes. The photomultiplier tube is affected by the ambient magnetic fields present outside or inside the facility. These coils actively compensate for the ambient magnetic fields in the PTF.

G-Iron is placed around the tank holding the PMT in the middle of the facility. G-Iron is a layer with high magnetic permeability (high μ) material similar to Mu-Metal in functionality that shields the PMT. By placing the G-Iron around the PMT the homogeneity of the field is improved.

High voltage (HV) is delivered to all the required components (receiver, monitor, SK 20-inch PMTs) of the PTF through high voltage system manufactured by Weiner GmbH.

The Phidget is a magnetometer, accelerometer, and tilt axis measurement used to know the status of the optical box. Phidget 0 and Phidget 1 are contained in Optical Box 0 and Optical Box 1 respectively. Phidget 3 and Phidget 4 are portable and used for environmental monitoring.

The PTF laser consists of a $\sim$405 nm laser with an attenuator. Laser light travels through an attenuator to the optical boxes. The laser beam received by the optical box is collimated, linear polarized and divided into two equal parts through the beam splitter. One part is given to the monitor PMT and the other part is directed at the PMT under test. The laser beam is selected manually before the experiment is performed.

The PMT is placed in the tank on fixed supports. The tank and PMTs are placed in the middle of the coils.

A small monitor PMT is located inside of each Optical Box and is used to calibrate the intensity of incident photons to the primary PMT.

The receiver PMT is another small PMT located in each Optical Box that can be used for reflectivity measurements.

The SK PMT is protected on the top with a large acrylic cover. Tape markers are on the acrylic cover to allow the PMT orientation relative to the dynode structure to be determined.

The Power Distribution Unit (PDU) in the facility is used to control the Wiener Crate, Laser, Galil Motor Controller, NIM crate, VME crate, and DAQ.

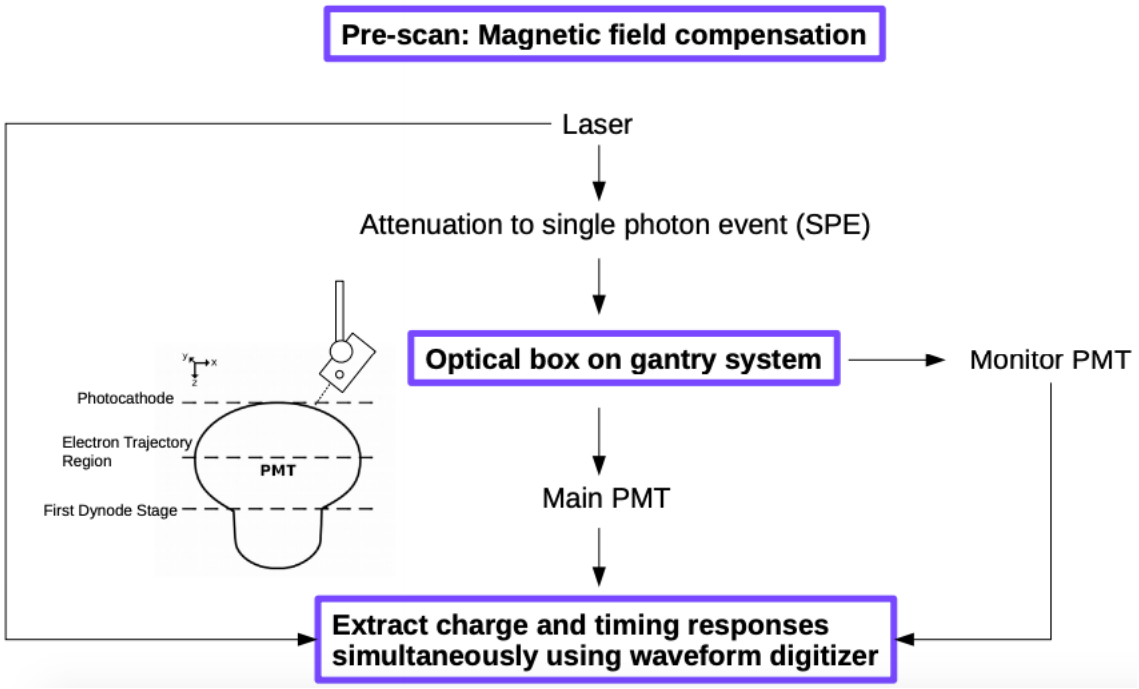

Figure 3.1: PTF scan setup

All the components are actively controlled and monitored to study the properties of the PMT [Figure 3.1]. The magnetic field is compensated to avoid stray magnetic fields affecting the PMT by surrwounding the PMT in the tank using Helmholtz coils as shown in Figure 3.2. The laser is pulsed, attenuated to the desired light level and allowed to travel through fiber optical cable towards the optical box in the gantry system. The beam splitter splits the laser beam into two halves and supplies one part to the monitor PMT and the other part to the primary PMT placed in the tank. Charge and timing response from the laser, monitor PMT and primary PMT are determined by waveform digitizer signals and further analysis.

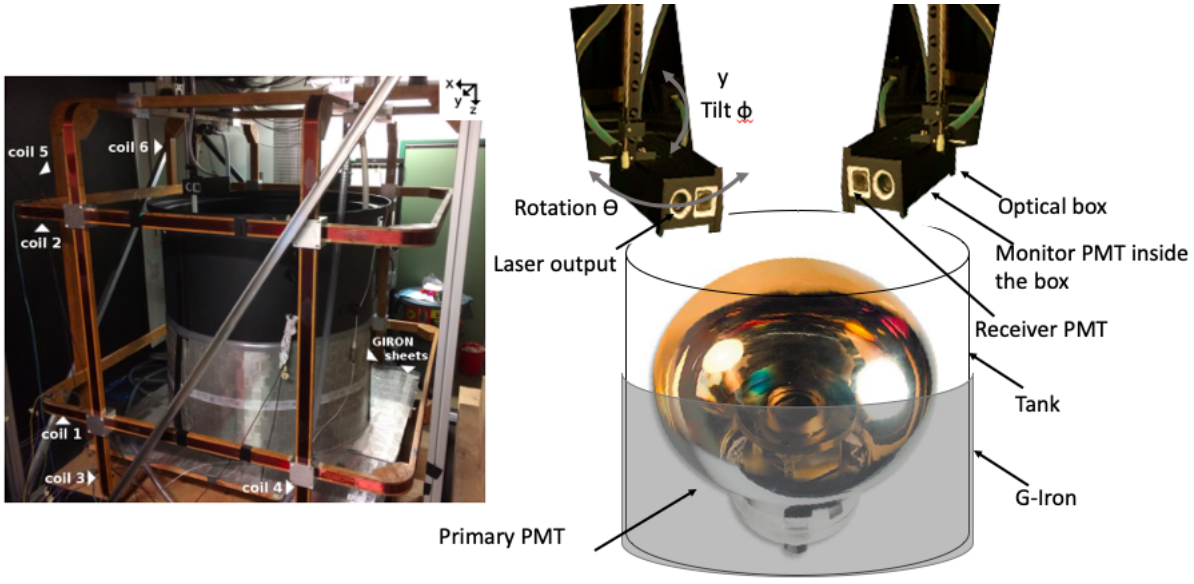

Figure 3.2: Photosensor Test Facility and the components used in the facility.

The hardware components described below work together for the efficient functioning of the facility.

The Weiner Crate HV modules provide a constant voltage output to the PMTs and the Helmholtz coil system. Power is delivered by several individually controllable channels. Control of this equipment can be accessed completely through either HV or Coil Control navigation tab of the software interface.

The Galil Motor Controller controls the gantry motion using a accessed from the movement navigation tab. The programs control the motors providing the motion of the gantry system itself. The Gallil controller can change the power to the motors and the power distribution unit.

The Hamamatsu Laser is a picosecond light pulser operating at 405 nm and provide the light pulse to the optical box.

The VME and NIM crates hold the data acquisition and triggering. The VME crate provides power to the electronics which process and capture the PMT signals (waveform digitizer, pulse generator, etc). The signal from all of the PMTs are read by the digitizer.

The pulse generator and a counter sets the frequency of the laser pulses incident to the PMT.

The desired data acquisition speeds can be achieved by reading out from the digitizer appropriately. The frequency dial is scaled by about a factor of 10 so the actual trigger frequency should be read from the events/second. The scans performed during studies are at about 1600 Hz. Scans use a default 3 seconds per point to provide a total of about 5000 waveforms per point.

The facility can be used for long term measurements at a single point on the PMT surface, over a two dimensional surface of the PMT surface at a fixed height from the PMT top (vertical injection scan), or over a two dimensional surface normal to the PMT face (normal incidence scan). After setting the desired attenuation level of the laser light, the magnetic field inside the coils, degaussing and setting the scan position, rotation, tilt angle of the chosen gantry, and surface coverage of the PMT in the desired number of points, the scan is started, and data is written in the form of a ROOT file. The time and charge produced in the PMTs are recorded by the digitizer.

Measurement of the response of the PMT at each point is done by analyzing the ADC (analog to digital converter) and the TDC (time digital converter) spectrum of the PMT at that particular point.

3.2 Measurements of a Super-Kamiokande photomultiplier tube

The 20-inch Super Kamiokande PMT response was measured in the PTF. The response of this PMT is corrected by and compared to the monitor PMT. The correction is necessary to account for the environmental factors such as changes in the temperature and light attenuation. The waveform digitizer plays a vital role as it allows simultaneous charge and timing measurements of both the PMT under test and the monitor PMT.

The amplitude of the recorded waveform in the ADC is proportional to number of photoelectrons incident on the PMT. This amplitude in ADC is histogrammed to make an ADC spectrum. The horizontal axis of the histogram represents the measured charge, and the vertical axis is a count of the events in each bin. One of the ADC histograms is shown in Figure 3.3

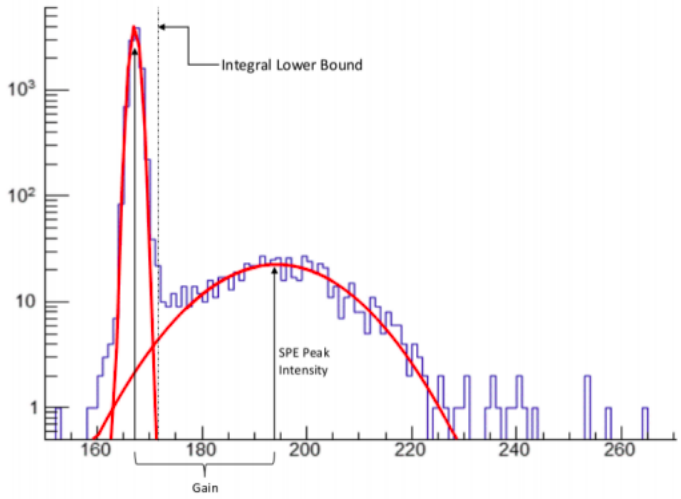

Figure 3.3: Example of ADC spectrum with no or low light levels. The sharp peak on the left is the pedestal and the broad peak on the right is the single photoelectron peak [30].

The pedestal is the signal observed with no incident photon, and represents the noise readout. The often peak in Figure 3.3 is due to single photoelectrons.

The spectrum is analyzed by fitting both the pedestal and photoelectron peak distributions with Gaussian functions and extracting the fit parameters.

Another way of studying PMT response is by analyzing the time distribution. Timing information for the PMT is acquired by measuring the difference in time between the signal from the monitor PMT and the time at which the PMT under test pulse crosses a certain voltage threshold. By plotting the distribution of the time differences, a skewed Gaussian can be obtained and fitted. The sigma of the fitted Gaussian provides a measurement of the Transit Time Spread (TTS) for that position on the PMT. The TTS of the monitor PMT is small [30].

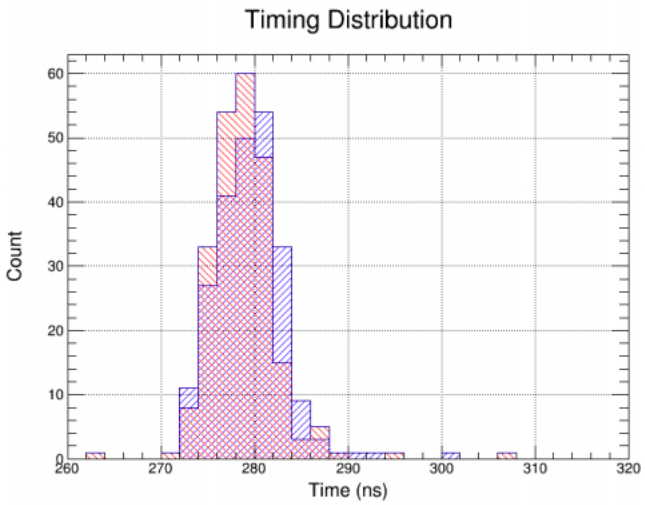

Figure 3.4: Distribution of time differences between the monitor PMT and SK PMT. Transit time distribution, with the blue showing the raw peak time differences and the red overlay shows the difference between the mean of the waveform fits [30].

Figure 3.4 depicts a sample Transit Time Distribution, with the blue showing the raw peak time differences and the red overlay showing the difference between the mean of the waveform fits.

The transit time spread measurement is important because it gives the time resolution of the detector, which in turn determines the location of an event in a large water Cherenkov detector such as Super-K. The time of flight of a photon incident to that PMT can only be known with uncertainty given by the transit time spread for a single PMT and can be corrected for the absolute transit time. Therefore knowing the transit time spread, allows a more accurate understanding of the position resolution achievable in the detector.

The detection efficiency is the ratio of the number of laser events observed by the PMT over the total number of laser flashes. This is measured by counting the number of times a single emitted electron results when there is a single incident photon. A photoelectron produced at photocathode generates an electron at anode. The count of electrons at the anode defines the overall gain of the PMT. It is equivalent to the anode current over the cathode current [31].

Terminology used in conducting scans of the PMT under test are:

1. Scan point - It is one location on the PMT, where a laser is flashed. One scan point can

contain about 5,000 laser flashes.

2. Event - An event is defined as one laser trigger observed by the PMT, resulting in one waveform for that event. An event is not a scan point. A scan point can have several events.

3. Low-intensity scan - A scans taken over the surface of PMT with low-intensity laser light (about 1 photoelectron(pe) level).

4. High Intensity scan - The PMT surface is scanned using a high intensity of laser light, provided the lowest attenuation to the laser. This is generally 100 pe level.

3.3 Efficiency of the Super-K PMT

The Super-K PMT output seems to be affected by the temperature variation in the environment. This is observed when shining the laser at one particular location on the PMT (single point scan) for hours and analyzing the efficiency. A graph of the gain is plotted to observe the behavior of the gain with temperature over a period of time. Figure 3.5 shows the behavior of detection efficiency due to the effects of temperature. In Figure 3.5 point shows the detection efficiency measured for about 5,000 laser triggers. The detection efficiency is directly affected by the change in the temperature in the facility.

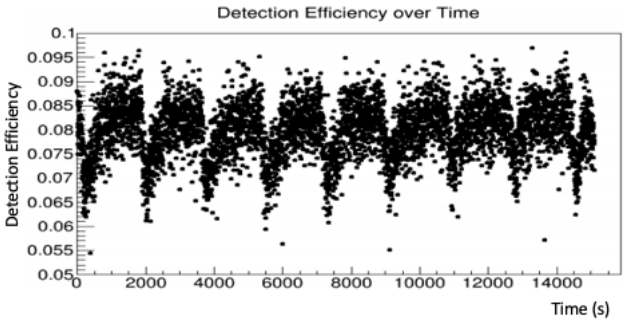

Figure 3.5: Detection efficiency at a single location on PMT hit by laser for about 15,000 scan point events. Each detection efficiency is measured using about 5,000 laser triggers [32].

The distribution of measured detection efficiencies is shown in Figure 3.6. The histogram

shows that there is a skew caused by variation in temperature.

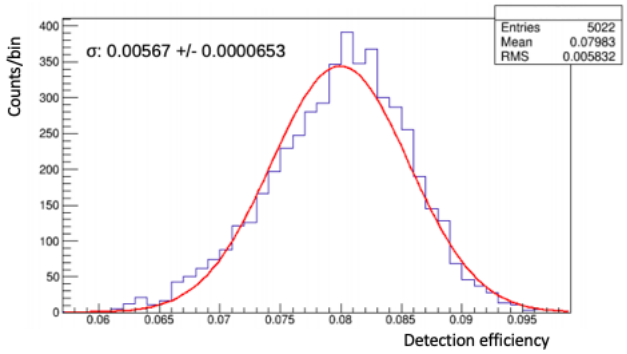

Figure 3.6: Detection efficiency histogram showing a skew due to changes in temperature [32].

Other parameters like gain, and transit time spread do not show this behavior, which suggests that it might be a property of the laser or attenuator. This effect is corrected by observing the light intensity seen by the monitor PMT (acting as a reference PMT). The monitor PMT shows the same behavior as the Primary PMT. A baseline is chosen from the monitor PMT efficiency distribution using the maximum bin of its efficiency histogram. Averaging over each minute of efficiency data of the monitor PMT to correct the PMT under test reduces the temperature dependence. The observed temperature periodicity is typically $\sim$ 30 minutes, which matches the period of the air conditioning of the room. The corrected detection efficiency as a function of time is shown in Figure 3.7(a). The correction applied can be verified by looking at the histogram of efficiency, which is more Gaussian and has a reduced sigma as shown in Figure 3.7(b).

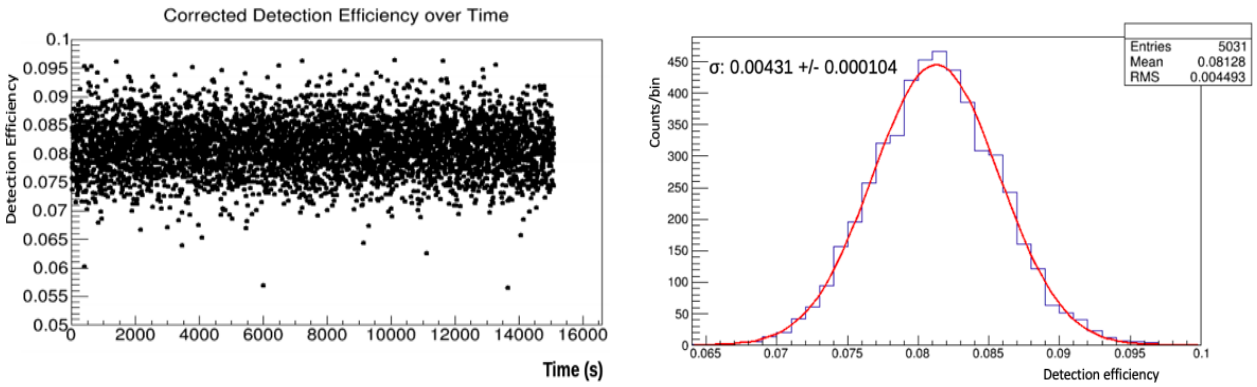

(a) (b)

Figure 3.7: (a) Detection efficiency as a function of time after temperature correction.(b)Histogram of detection efficiencies after temperature correction [32].

Figure 3.6 and 3.7(b) show single point scans, performed at one single position on the PMT surface over a long period of time. The full surface scans taken showed periodic banding, which was due to temperature variation in the facility as shown in Figure 3.8. The banding was periodic and distributed regularly all over the PMT surface.

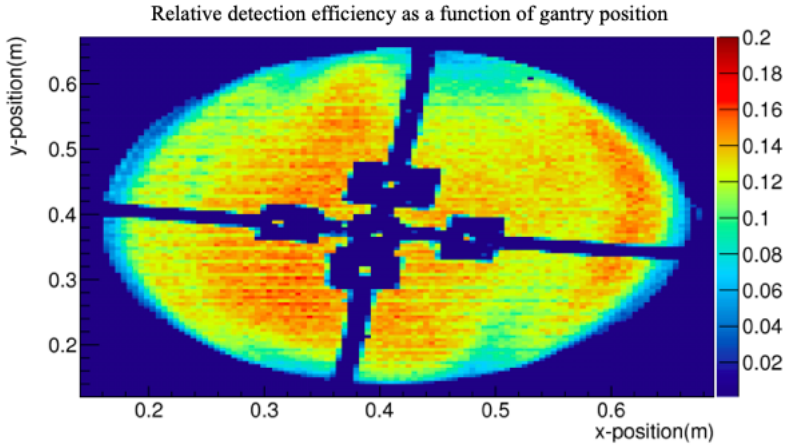

Figure 3.8: Two dimensional detection efficiency histogram showing the bandings due to temperature variations in the facility. This is Super-K PMT with acrylic cover on. The cross was marked on the cover by opaque tape [32].

The test is repeated by taking the acrylic cover on the top of the PMT off and further scans for cross verification were taken. Fig.3.9(a) shows the persistence of banding without cover too.

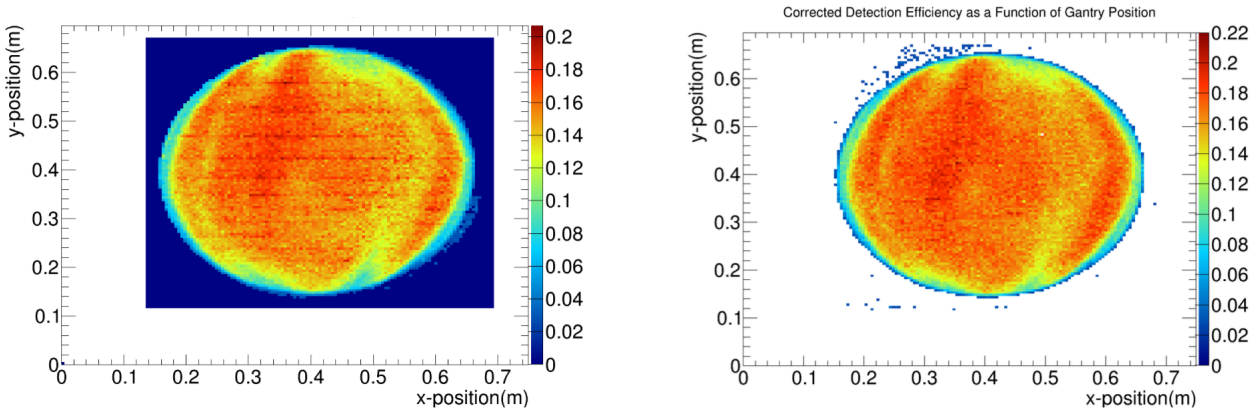

(a)

(b) Corrected cover-off detection efficiency of Super-K PMT

Figure 3.9: (a) Detection efficiency over the full surface of the Super-K PMT without acrylic cover on it. The periodic banding shows the temperature dependence of the efficiency. (b) Detection efficiency of the Super-K PMT without acrylic cover, after applying the monitor PMT correction. It removed the banding completely [32].

The monitor PMT was successfully used to correct the data taken in the single point scan, it was applied to the full surface scan. Fig.3.9(b) shows that the correction procedure works very well to remove the periodic banding due to temperature over the surface of the PMT.

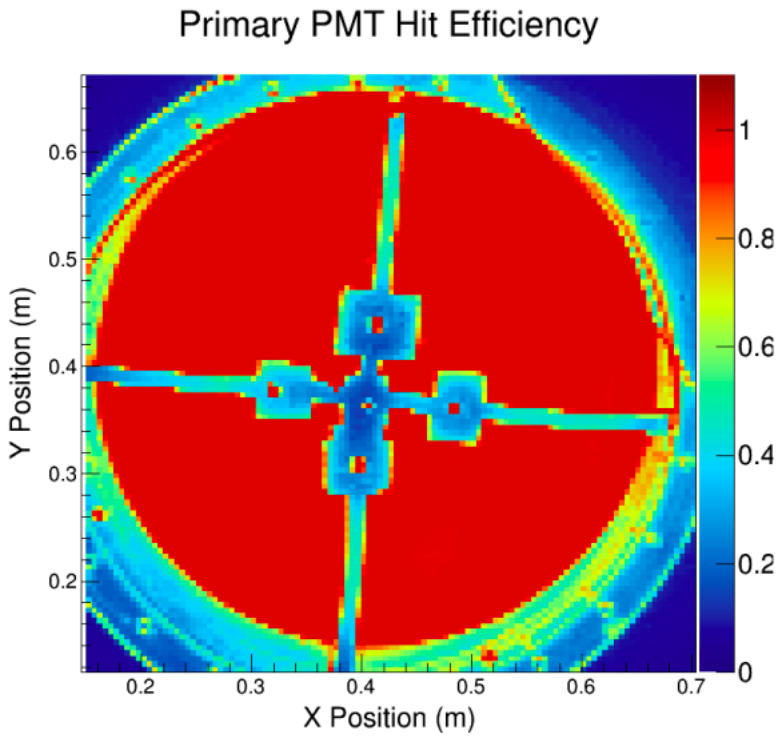

Figure 3.10: Two dimensional detection efficiency of Super-K PMT with acrylic cover on. The cross was marked on the cover by opaque tape. Efficiency is 100% for high intensity laser light.

The efficiency is also studied for high-intensity scans, where the laser light is attenuated to the minimum possible level and laser light produces about 100 photoelectrons. Figure 3.10 shows that efficiency reaches 100% for high-intensity laser injection. For in air scans reflection from the acrylic cover reflects the laser light and produces hits on the PMT surface generating non-zero efficiency for locations outside of the PMT.

3.4 Gain of the Super-K PMT

The measurement of the PMT is affected by the temperature. The low-intensity gain is corrected using the same procedure as the one used for efficiency. Again the baseline is determined from the maximum bin of the gain of the monitor PMT and averaged over every minute. The process removes the periodic banding that appeared in the gain of the primary PMT. Fig.3.11 (a) and (b) show the two-dimensional histograms for low-intensity laser injection with and without cover respectively after correction.

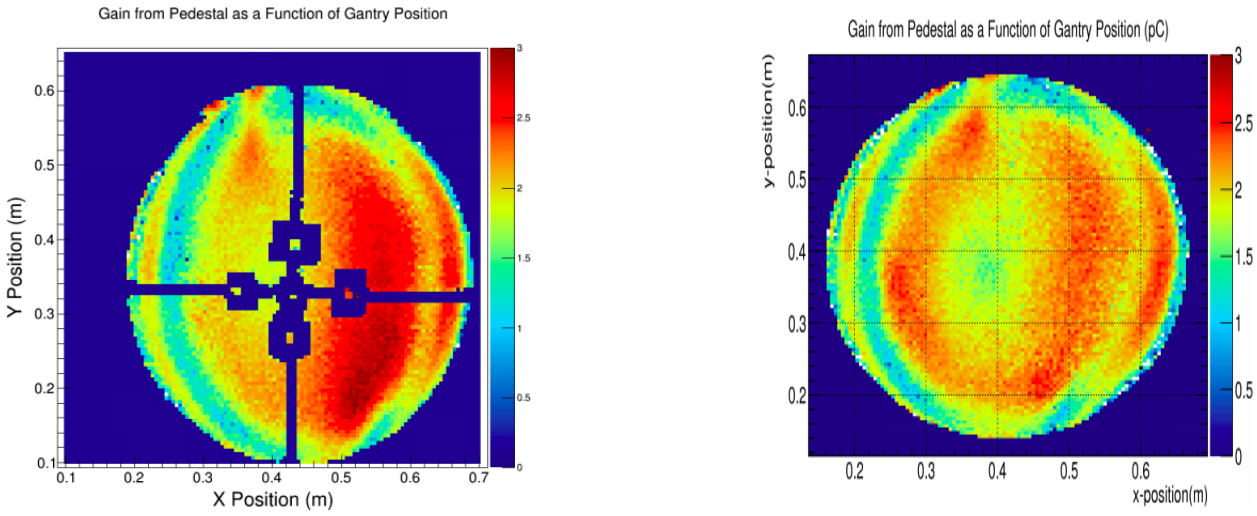

(a) (b)

Figure 3.11: (a) Gain over the full surface of the Super-K PMT with acrylic cover on it for low intensity laser injection. (b) Gain of the Super-K PMT without acrylic cover.

The periodic banding due to temperature is observed in the high-intensity laser injection scans as well, where a correction has not yet applied. A clear picture of 5 mm resolution of high-intensity laser injection scan is shown in Figure 3.12. Figure 3.11(a) and (b)shows that the right two quadrant does not show the same distribution as in the left quadrants. The asymmetrical distribution of the gain pattern throughout the PMT shows that there is either an effect due to the dynode structure, or something wrong with the dynode structure of this particular PMT. Thus it would be a good to repeat the measurements with a different 20-inch PMT to compare the results.

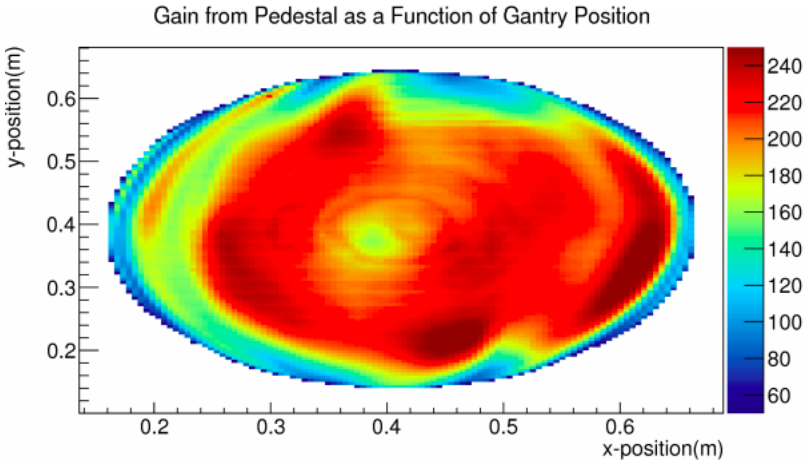

Figure 3.12: High intensity laser injection scan on Super-K PMT without acrylic cover. The banding in the plot above shows there is a temperature dependence to the observed gain.

3.5 Concluding remarks

The PTF facilitates the features required for an investigation of the properties of the various PMTs. The 20-inch Super-K PMT is the most well studied PMT in the PTF to date. The efficiency and gain of the PMT can be corrected for temperature drifts that were found to effect the measurements. The high intensity vertical injection scans shows banding in temperature, which is yet to be corrected.

4. Simulation of water Cherenkov detectors

WCSim is a simulation platform for water Cherenkov detectors with photomultiplier tubes setup on the sides, top, and bottom. Parameters in the simulation allow different configuration of detectors to be easily defined. The simulation uses Geant4 for specification of the detector and materials used in it. Additional details are added to fully specify the parameters of water as a function of optical photon energy.

4.1 Setting up a detector geometry in WCSim

WCSim simulates an upright cylindrical detector (in WCSimDetectorConstruction::ConstructCylinder()). The geometry defines the inner detector consisting of blacksheet and PMTs, which are organized into cells on all sides of cylinder. The outer detector can optimally be added and contains a blacksheet, a whitesheet, and PMTs. A steel structure can also be added to the outer detector, as needed.

As with most Geant4 detector geometries it is built in layers. The outermost layer is the experimental hall (ExpHall). The water volume is defined in the hall which includes a barrel (WCBarrel), which is filled with water. WCBarrel contains PMTs and structure. WCBarrel includes the annulus and the caps. The annulus is the main part of the detector and is composed of barrel ring (WCBarrelRing) made up of barrel cell (WCBarrelCell). The barrel cell is a flat modular section which contains one or more PMTs and the blacksheet as shown in Figure 4.1(b).

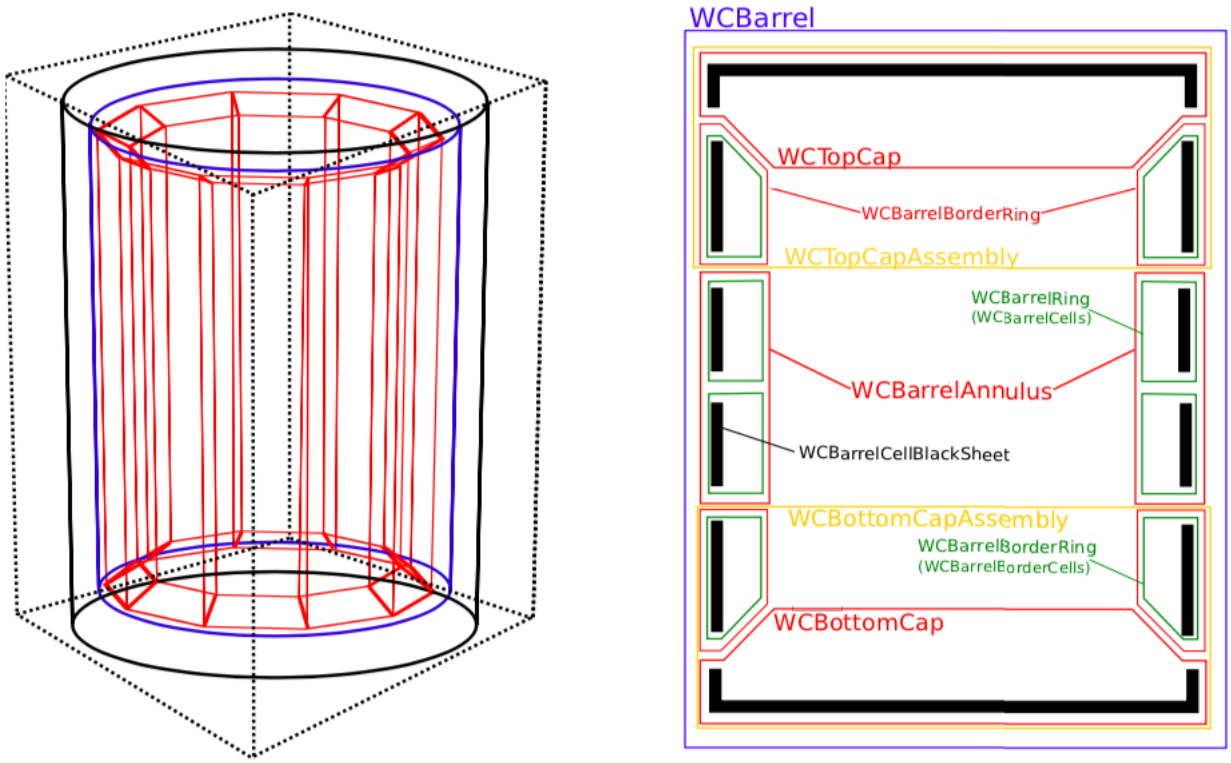

(a) (b)

Figure 4.1: (a) Drawing of cylindrical detector in WCSim. The dotted rectangle shows the ExpHall filled with air. The solid black shows the cylindrical volume returned by WCSimDetectorConstruction::ConstructCylinder(). The blue inner cylinder shows the shows the water-filled cylinder WCBarrel. The red cylinder shows the WCBarrelAnnulus, WCTopCap and WCBottomCap. (b) Figure shows a 2D diagram for logical volume contained in WCBarrel. This shows the labelled sub-volumes.

The top cap assembly (WCTopCapAssembly) and bottom cap assembly (WCBottomCapAssembly) are identical volumes at the end of the barrel as shown in yellow rectangles in Figure 4.1(b). The cap PMTs (WCPMT) have a blacksheet (WCCapBlackSheet) behind them and are extended at the cylindrical edges to connect to border barrel ring of the PMTs at the border (WCBarrelBorderRing) as shown in red boxes in Figure 4.1(b). WCBarrelBorderRing is the uppermost or lowermost ring of PMTs, which connects the corners with the caps. The border rings also contain border cells (WCBarrelBorderCell) which holds individual PMTs and the blacksheet as shown in green boxes in Figure 4.1(b).

Each single PMT is contained in a cylindrical volume (named WCPMT in WCSim), and is repeated many times to cover the dimensions of the detector. The coordinate origin of each PMT inside the cylinder is defined by the intersection of the PMT cathode axis with the blacksheet. The PMT contains two volumes, the hollow glass outer face of the PMT (GlassFaceWCPMT) and the inner vacuum (interior WCPMT). The inner surface between glass and vacuum is modeled as an optical surface (GlassCathodeSurface).

WCSim provides an option to add data acquisition using DAQ classes. One can also introduce the effect of dark noise. A photon hitting a PMT produces a photoelectron and charge is deposited on a PMT is defined as a 'Hit'. The number of photons is integrated including electronics threshold effects to produce a 'Digit'. The raw Geant4 hits are stored in a collection of the hits (WCRaw-PMTSignalCollection) and the output the digits is given in WCSimWCDigitsCollection. There is a class to take a collection of hits as an input and return a collection of triggered digits as an output.

One of the nice features of WCSim is that it allows a detector with the desired dimensions to easily be setup. The detector dimensions are set in the code (in WCSimDetector Configs.cc). Some parameters of the detector are set up to be modifiable at run time by editing in a macro file[for more details ref. to [33]]. The detector geometry also selects what type of the PMT to be used, including the radius of the cathode surface and its height above the blacksheet surface. The thickness of the PMT glass is also set. The other parameters can be set according to the desired needs to customize a detector of one's own choice.

4.2 Setting up the data acquisition in WCSim

Once the desired detector is selected, data acquisition is set up to the output PMT digits in a root file which contains two tables of data (TTrees in root). One table holds hits and digits of each event (WCSimT) and the other holds the detector geometry (WCSimGeoT).

The WCSimT stores the observed triggers in a branch called (WCSimRootEvent). There is minimum 1 trigger which holds the information of the initial particle tracks given to GEANT. The delayed decay particles are added as subevents.

Each WCSimRootEvent also holds branches for each trigger in WCSimRootTrigger. The truth

information about the Cherenkov photons that were generated is stored as well as the PMT digit information. Geant4 commands used in particular are mentioned in a table in appendix.

The information about the true tracks from particles generated in the simulation are also stored in a separate branch in the output (WCSimRootTrack). The truth information stored is the particle species, mass, momentum, the starting and the stopping positions, and the parent species.

Cherenkov photons generated are recorded in WCSimRootCherenkovHit before digitization. The number of true Cherenkov hits is given by GetNcherenkovhits(). It records the tube ID number of the hit.

The true time and parent IDs of each Cherenkov photon is stored in one branch of the TTree (WCSimRootCherenkovHitTime). The photoelectrons detected by a particular phototube are used to determine the true time of the light. The ID number of parent particle is also recorded, allowing each photon to be traced to a specific true particle. The digits record charge and time of each PMT in a branch named WCSimRootCherenkovDigiHit.

The geometry TTree holds the radius and length of the detector, as well as the number of PMTs, their locations, and facings.

The information for each PMT includes its ID number, and location. It also has a variable to say whether it is on the top cap (0), bottom cap (1) or on side wall (2). The location of the center of the sphere of the PMT in x, y, and z ordinates is what gets stored for the position of the PMT. The direction of the PMT facing as the x, y, and z direction vector is also stored.

4.3 WCSim for IWCD

The geometry of the IWCD was programmed into WCSim, and tests done in this thesis used Geant4 version 4.10.02. The code used is available for download from github [34].

4.3.1 IWCD Geometry setup in WCSim

The IWCD is a cylindrical water Cherenkov detector which has 15,808 PMTs. In particular, the PMTs used in this detector are 3-inch PMTs (R12199_02) [35]. The PMTs are arranged in a hexagonal matrix in multi-PMT modules and a single module contains 19 PMTs. The PMTs are

in an acrylic vessel, and are coupled to the dome using optical gel. The PMTs are held in a support structure. Figure 4.2 shows the arrangement of an mPMT module in WCSim. The origin of the mPMT is on the Inner detector blacksheet wall.

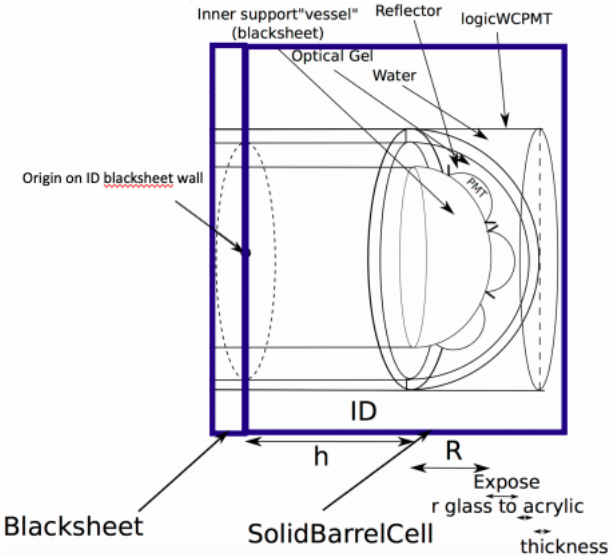

Figure 4.2: The schematic of mPMT module in WCSim [36].

4.3.2 Generating events in WCSim

For tests of timing calibration, a source of light is generated using Geant4's generalized particle source (GPS). A separate light source generator (LED) was written that add a timing distribution. The detector is centered at the origin to the light [37]. As shown in Figure 4.3 the z-axis is vertical along the axis of the cylinder and the x, y plane is in the center of the cylinder. The radius of the detector is 370.1 cm and the half height of the detector is 517.0 cm.

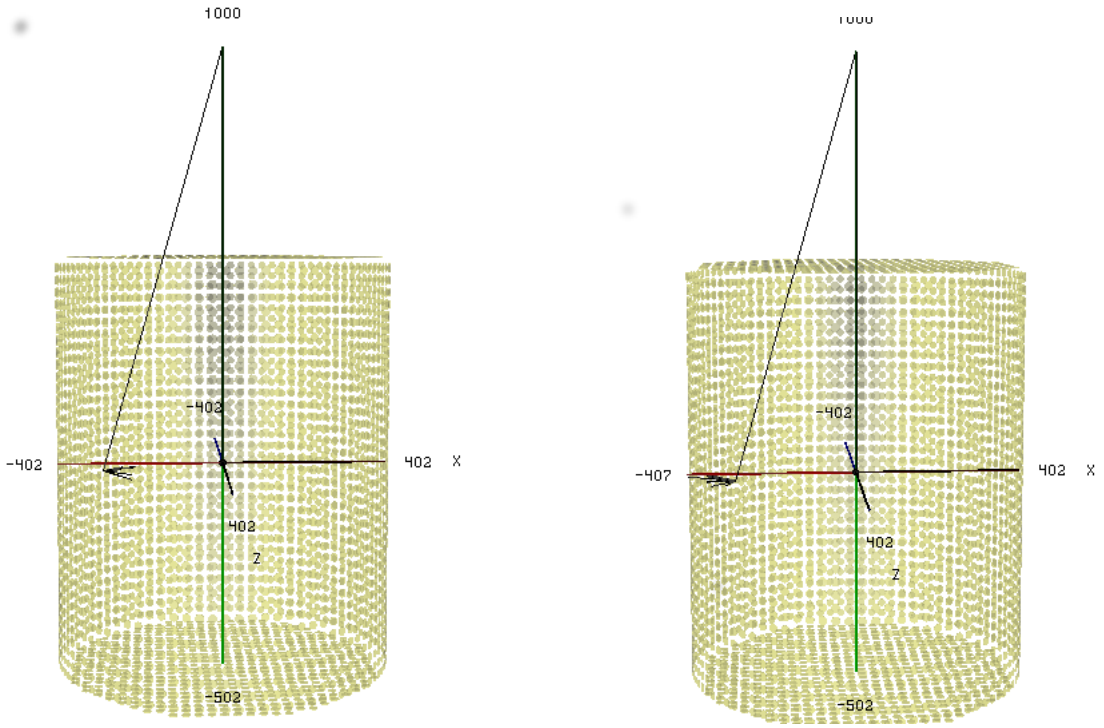

(a) (b)

Figure 4.3: Display of the WCSim geometry where the PMTs are shown in yellow. (a) The left figure shows a conic source light flash starting at (x=-290.7, y=-14.4, z=-14.3) cm and facing towards the +x-axis. (b) The right is for the same settings as (a), but with facing towards the -x-axis.

For digitization a new messenger class is added that allows time delays due to electronics in each PMT. This was done to enable studies of how well these delay could be found using light flashes.

5. Timing calibration for water Cherenkov detectors

The purpose of the timing calibration is to allow for the best possible physics measurements from the detector. Timing response of different PMTs is based on various factors such as their position in the detector, length of cables and the processing time of readout electronics. Timing is also affected by the amount of charge collected because larger pulses take a longer time to cross the discriminator threshold than shorter pulses. The calibration is done using an optical source which can produce a pulse of light with a width of $\lesssim$1 ns. The light is isotropic and placed in the center of the detector (or other location) which allow it to provide light to as many PMTs as possible. The number of photoelectrons registering in the PMTs is called the charge in the PMTs.

5.1 Geometry of calibration for a single PMT

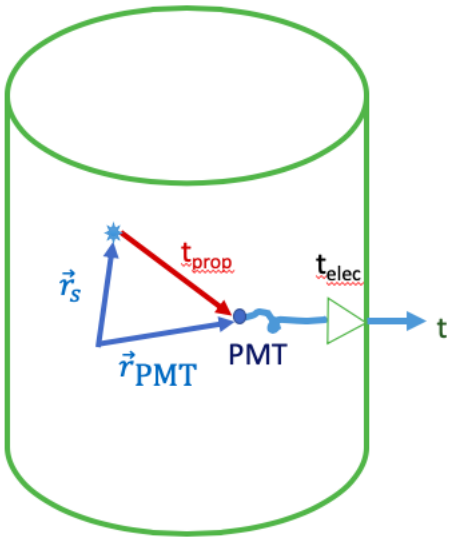

Figure 5.1: Geometry of IWCD used for calibration of time.

For timing calibration we use a single wavelength light pulse that is short enough in time that we can neglect its time spread in calibration each PMT channel. The isotropic light source is

placed at a location $\vec{r}_s$. The initial time for the emission of light is t_0, the light propagates through the detector, and reaches the j-th PMT, located at $\vec{r}^{j}_{PMT}$ at a time t^j_{prop}. Geometry of the source to the PMT path of light is shown in Figure 5.1.

The PMT introduces a random transit time spread of a few ns, which cannot be corrected. An average of transit time is denoted as t^j_{PMT}. Time delay is also added due to cables and electronic delays due to digitization as t^j_{elec}. The time recorded by the j-th PMT t_j is:

$$t_j = t_0 + t^j_{prop} + t^j_{PMT} + t^j_{elec}. \tag{5.1}$$

The propagation time depends on the index of refraction of water n(λ, T, $\vec{r}$), which is a function of wavelength of the light λ, and could also depend on water quality at each location in the detector $\vec{r}$, and temperature T. If the index of refraction were a single constant, the same for all locations in the detector, we could write the propagation time as:

$$t^j_{prop} = n\frac{|\vec{r}^{j}_{PMT} - \vec{r}_s|}{c}. \tag{5.2}$$

In this case we can calculate the PMT plus electronic delay for each channel and use group velocity instead of phase velocity:

$$t^j_{PMT} + t^j_{elec} = t_j - t_0 - n\frac{|\vec{r}^{j}_{PMT} - \vec{r}_s|}{v_g}. \tag{5.3}$$

Here the group velocity in a dispersive medium such as water is given by:

$$v_g = \frac{c}{n}\left(1 + \frac{\lambda}{n}\frac{dn}{d\lambda}\right) \tag{5.4}$$

.

Using the above relations, we can build a chi-squared χ^2 which can be minimized to fit for the parameters t_0, (t^j_{elec}, v_g, $\vec{r}_s$. This represents N^{PMT}+ 6 parameters. This will only work with more than one flash of light, as there would be more parameters than data points, which would nominally be N$_{PMT}$. If number of light flashes are labelled as i, then chi-square is given by:

$$\chi^2 = \sum_{i=0}^{N_{flash}-1} \sum_{j=0}^{N_{PMT}-1} \frac{1}{N_{flash} N_{PMT} \sigma^2_{t_0}} \Big(t_0 - t_{i,j} + t^j_{elec} + \frac{|\vec{r}_s - \vec{r}^{\,j}_{PMT}|}{v_g} n \Big)^2. \tag{5.5}$$

Constraints are added to χ^2 to account for having some information about the location of the source, and some information on the potential range of v_g and n. The exact values chosen for these constraints depends on the calibration system that gets built, and some study of the range of n/v_g that is possible in the detector. An initial guess is that the position a light source is known with uncertainty σ_r = 5 cm, and the index of refraction is $n_{nominal}$ = 1.3 $\pm$ 0.1, with the nominal value chosen depending on the wavelength of light being used. The χ^2 is minimized using the TMinuit2 framework [38].

5.2 Method of Analysis for minimizing chi-squared to determine each PMT's time offset

The motivation of the analysis is to know the time and difference in time after applying calculations, which will lead to calibration of time.The code for the analysis of the simulated IWCD data was written in C++ and, uses ROOT platform for output [39].

The analysis script starts by initializing constants like the speed of light, the position of the source in the detector (x, y, z), energy, wavelength, time-offset in WCSim (950ns), and refractive index used in the simulation. The refractive index is set per material in tables coded in the WCSim framework. The WCSim source code holds all the information about the materials (like water, acrylic, vacuum, steel, aluminum, etc) . through which the photons will pass along with their properties (like absorption constant, scattering constant, refractive index, energy, etc) [40]. Once the wavelength of the light source is chosen, one can look in the source file (WCSimConstructMaterials.cc, in particular) to see the respective refractive index used in the simulation.

The analysis script defines a singleton class (a class with only single instance) to hold the PMT time information needed to do the fit for the timing calibration. An important part of the analysis script is the function to read in the simulation output root file, and also read the time-offset text file containing the set of numbers generated by simulation as offset times for each PMT due to digitizers and cables. After reading these files, the analysis gets the detector geometry from the simulation output root file. The PMT radius, detector radius, cylindrical length of the detector, the offset of the origin (from which detector is centered), and extreme values of the detector in cm in x, y, and z directions are read.

Histograms are defined to plot distributions of number of hits, charge, true-time, the digitized time, corrected time (after applying corrections of transit time, offset time and time due to electronics), and 2D histogram to study the relations among the above-calculated parameters. The histograms are also plotted for each event and every single PMT to understand the problem fully.

The program loops over the total number of events, and for each event, loops over the total number of PMTs. Each event's digitized data could have several triggers. The first trigger contains information about the main event, from which the digitizer hits are loaded. Each digit read in has the digitized time that is used to study timing calibration. To know the position of the hit extracted, we use the information from the geometry tree based on the TubeID (PMT). The positions are used to fill in the histograms with charge or time as a function of position. The distance of the propagation is calculated between the position of the PMT and the source position. The propagation time t^j_{prop} for each PMT is calculated using propagation distance, refractive index and the speed of light.

The truth information about the photoelectrons reaching each PMT before electronics is also available (as nCherenkovHits). These recorded true times are used to plot histograms of true time and correction (due to propagation time taken by a photon to reach the PMT from the source) applied to the true time.

The next part of the analysis fits a Gaussian peak to the true time, corrected true time and digitizer time to get the mean and sigma of the distribution. The times observed in each PMT

shows very few late hit times which causes the mean of the PMT to be away from the prompt distribution of time (which contributes to the main peak). The analysis also provides an option of the cut on the number of hits observed in the PMTs. The cut is made to choose only the PMTs that observes the prompt light in earlier time and contributes to the main distribution of time in a PMT. If the number of hits due to photoelectron production (before recording in digitizer) observed in a PMT are less or greater than a certain number then the PMT is included, otherwise rejected. Using this cut is completely optional and used more for observing the location of PMTs which observe the enough light for calibration.

The next step in the analysis to fill 2-D histograms of variables as a function of position. The variables plotted are true-time, corrected true time, corrected digitizer time, and number of hits in the PMTs. Separate histograms are made for the top, bottom and sides of the detector.

The next and most important part of the analysis is to minimize the chi-squared as defined in eq. 5.1. The minimization is done in steps. First the five parameters, the position of the source in x, y and z-direction, group velocity, and overall time-offset is determined by minimizing the χ^2 using root Migrad minimizer in Minuit2. These five parameters are then fixed and the time-offset due to electronics in PMTs. Minimization is done to determine the time-offset for all of the PMTs. Ten PMTs are fit at a time and the fitting continues until all of the time-offsets are determined.

The main idea is to get 10 PMTs from far away points in each fit. This allows the source position to be determined from the timing. The technique used for choosing random PMTs is as follows.

1. The detector is divided into five sections as one for top, one for the bottom, and three for the side. This is done by looking at the tube number and storing these PMT numbers into named vectors, representing the location of a section in the detector. In total there are 15,808 PMTs which are divided as 3161 in the top and bottom each, and 3162 in each section of the side.

2. Ten PMTs are, are then randomly selected two from each section, without replacement until there are fewer than two PMTs remaining in any section.

Once the five parameters are determined by the minimization of the χ^2, the time-offset due to the electronics of the PMTs are found ten PMTs at a time. The minimization continues until all the time-offset of all of the PMTs are found. When minimization ends, the time-offset are histogrammed and compared to known true time-offset.

To see the minimization behavior of five parameters, i.e., source position in x, y and z, group velocity, and any time-offset due to the PMT, the minimization steps are repeated for the desired number of times. The repeated steps include first finding the five parameters and then these minimized parameters are fixed while the electronic time-offset in PMTs are determined at a count of 10 PMTs at a time.

5.3 Rayleigh scattering and its effects

When an electromagnetic wave propagating in matter interacts with an atom, molecule or particle, the electrons move back and forth, and the oscillating electric field E creates an oscillating dipole moment, μ such that

$$\mu = \alpha E, \tag{5.6}$$

where α is the polarizability.

In 1871, Lord Rayleigh published a paper describing a phenomenon of dispersion of electromagnetic radiation by particles that have a radius much smaller than the wavelength of the radiation. The dipole oscillates at the same frequency as the incident radiation frequency, E = $E_0 \sin 2\pi\nu$ and the light scatters symmetrically in the forward and backward scattering from a single particle [41].

The original implementation of WCSim for IWCD used 8-inch PMTs. The simulations study of the effect of Rayleigh scattering was done with the 8-inch PMTs in the detector. The photocoverage of the detector using 8-inch PMTs is the same as the 3-inch mPMT detector.

The photons traversing the detector are subject to the interactions in water. A conic light source was placed at one point in the middle of the y-axis near one of the sidewalls facing away to the

opposite side of the wall in order to study the effect of Rayleigh scattering. The energy of the photons used in this simulation was 3.101 eV which is $\approx$ 400 nm in wavelength. This specific simulation involved 1000 light flash events where each flash has 50000 photons. Figure 5.2 (a) shows the distribution of digitized times when the light hits the wall (950-960) ns. Three peaks in the timing distribution are clearly visible. The earliest peak is the direct light reaching the close wall of the detector, the middle peak is the direct light reaching the farther side of the detector and the latest light, in the third peak is the reflected light. The light of wavelength with incident intensity I_0 scatters in all directions to form the light intensity I which is given by:

$$I = I_0 \frac{8\pi^4\alpha^2}{\lambda^4 R^2\big(1 + cos^2\theta\big)}. \tag{5.7}$$

where, α is the molecular polarizability, λ is the wavelength, R is the distance to the particle and θ is the scattering angle.

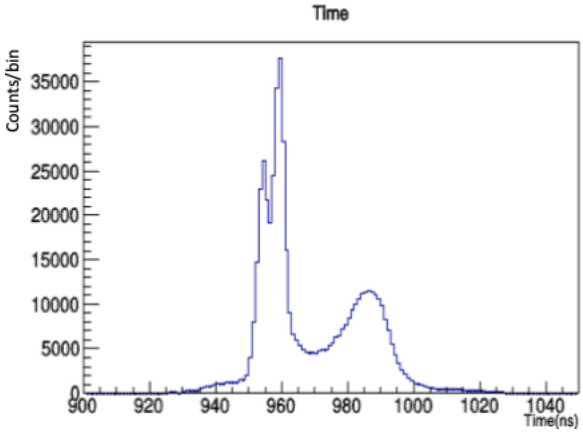

Figure 5.2: Time distribution due to travel of photons from the source to the digitizer.

The timing distribution was further investigated by turning off various physics processes in the simulation. WCSim holds the information about all the physics processes involved in the simulation. By default, all these processes are on. Rayleigh scattering and Mie scattering were found to be the processes of interest. Both of these scattering processes occur when the traveling

light scatters. Rayleigh scattering occurs when the particle size of the scatter is much smaller than the wavelength of the incident light. Mie scattering occurs due to particles with size larger than the wavelength of light.

The process of Mie scattering was turned off to see if it makes a difference to the time distribution. Figure 5.3 shows that turning off the Mie scattering process does not make any significant difference. Thus Mie scattering is not contributing much. This makes sense because the wavelength of light used, the Mie scattering interaction length is

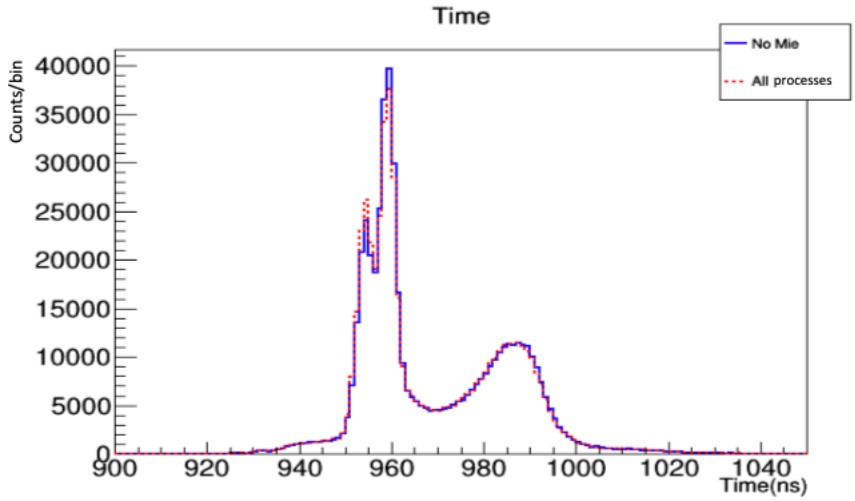

Figure 5.3: A figure to show the difference between the time distribution with all physics processes in red dashed line and without Mie scattering in blue line distribution. Turning off of Mie scattering does not show any significant difference.

Figure 5.4 shows that turning off the Rayleigh scattering removes the double peaks in the earlier time for the direct hits. This makes sense because the Rayleigh scattering distribution includes a large number of back scatter events, causing light in the cone to return to the rear wall.

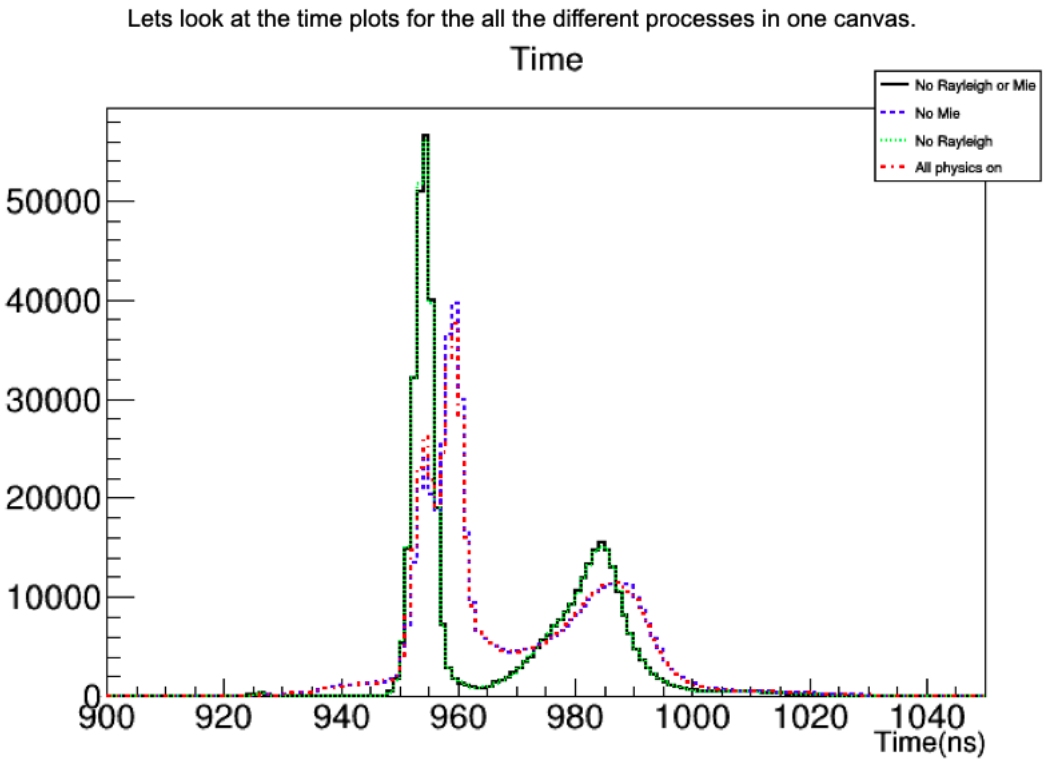

Figure 5.4: Turning off the Rayleigh scattering in simulation removes the double peaks. Light scattered by the water molecules in the tank affects the behavior of light observed by the PMTs. The red dotted line shows the original distribution. The blue dotted line shows the distribution without Mie scattering involved. The green dotted line distribution appears when Rayleigh scattering is turned off. The solid line appears when both Rayleigh and Mie scattering are turned off.

In the newer version of WCSim with a detector containing 3-inch mPMT modules, the physics lists were changed, and the method of turning off physics processes changed. Because of these changes the Rayleigh scattering study was not repeated for the 3-inch mPMT detector simulations.

5.4 Group velocity and phase velocity

A one-dimensional plane wave ψ propagating in +x direction can be represented as

$$\psi = Z \exp i(kx - \omega t). \tag{5.8}$$

In the above equation, ω is the angular frequency of the wave; k is the wavenumber, and Z is the amplitude. The light waves travel at constant velocity c, thus

$$\omega = ck \tag{5.9}$$

The wave can be written as:

$$\psi = Z \exp ik(x - ct). \tag{5.10}$$

In general, the phase i(kx-ωt) is constant. Thus from eq. 5.4

$$\frac{dx}{dt} = \frac{\omega}{k} = v_p, \tag{5.11}$$

where v_p is the phase velocity. The refractive index, n can be defined as a ratio between the speed of the light, c and the phase velocity, v_p,

$$n = \frac{c}{v_p} = \frac{ck}{\omega} v_p = \frac{c}{n}. \tag{5.12}$$

The group velocity is defined as the superposition of many simple plane waves of varying frequencies, resulting in a wave propagating at a velocity of an envelope and a carrier wave within the envelope. The group velocity of a wave of wavelength λ is given by:

$$v_g = \frac{\partial \omega}{\partial k} \tag{5.13}$$

where ω is the angular frequency of the wave, and k is the wavenumber. The group velocity and phase velocity are related by:

$$v_g = v_p \left(1 + \frac{\lambda}{n} \frac{\partial n}{\partial \lambda} \right), \text{or} \tag{5.14}$$

$$v_g = \frac{c}{n}\left(1 + \frac{\lambda}{n}\frac{\partial n}{\partial \lambda}\right). \tag{5.15}$$

In terms of energy, this can be written as:

$$v_g = \frac{c}{\left(n + \frac{1}{n}\frac{\partial n}{\partial E}\right)}. \tag{5.16}$$

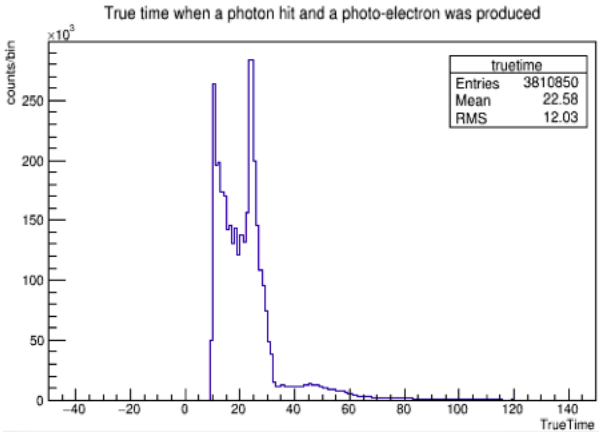

Figure 5.5: True time distribution. This represents the time when photoelectrons were captured by PMTs in the detector before passing through electronics.

5.5 Studies of True time distribution

A study of IWCD containing 3-inch mPMT modules, revealed the effect of the group velocity and the phase velocity. The light waves traveling from the source to the PMT are in the form of superimposed waveforms and therefore should propagate at the group velocity. A simulation, with 200000 optical photons in an event at a wavelength of 400.1 nm and 3.1 eV was done. At this energy the water's refractive index is 1.34. In the mPMT simulation the tank contains 15808 3-inch PMTs. This particular study was done by placing a source of 400 nm wavelength at position (x=150.0, y=0.0, z=0.0) cm in the detector. The true times of the photoelectrons produced in

the PMTs corrected for the propagation time from the source to the PMT are histogrammed in Figure 5.5.

The propagation time correction applied to the time of photo-electron production in PMT should end up with a single narrow Gaussian peak distributed near zero. Blue distribution in Figure 5.6 shows two peaks in the corrected time distribution when using phase velocity. Figure 5.6 shows the distribution when group velocity (red line distribution) and phase velocity (blue line distribution) is used.

The value of v_g is used from eq. 5.4. Using this calculation in the correction to the true time, red peak in Figure 5.6 shows that the double peak vanishes and the time distributes narrows. The comparison of the corrected time when using group velocity and phase velocity is shown in the overlayed histograms in Figure 5.6. Clearly using the group velocity, which correctly describes the physics gives a better result. Also this shows that Geant4 must be using the group velocity as it should be.

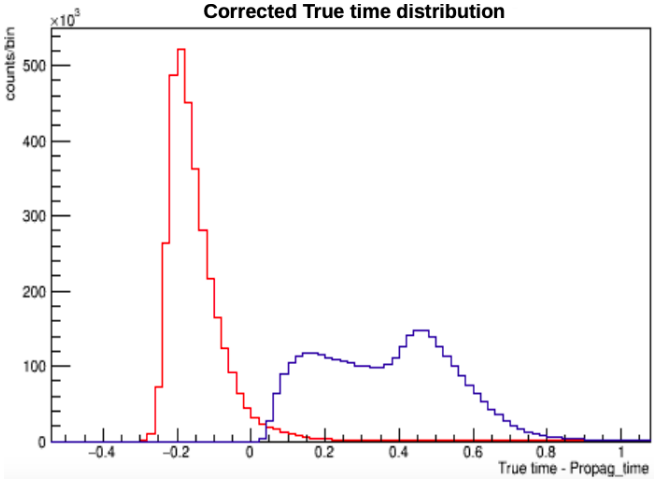

Figure 5.6: The blue line shows the corrected true time distribution when phase velocity is used and the red line is the corrected true time distribution with group velocity used in propagation time calculations.

The formula used in the Geant4 for calculation of group velocity is:

$$v_g = \frac{c}{\frac{n_0+n_1}{2} + \frac{dn}{dlogE}} \tag{5.17}$$

where, n_0 and n_1 are the refractive indices at two energies nearest to the photon being simulated.

The group velocity is given by

$$v_g = \frac{c}{n_0 + \left(\frac{n_1-n_0}{log\frac{E_1}{E_0}}\right)}, \tag{5.18}$$

where c is velocity of light, E_0 is the energy of simulated light source, E_1 is the next energy in the table of refractive indices used by Geant4, n_0 is the refractive index corresponding to the simulated energy, and n_1 is the refractive index corresponding next to the energy. Clearly the table of refractive indices should contain enough points in energy to provide a realistic representation of the group velocity. This allows only normal dispersion, thus the above calculations only works in dispersive media where

$$\frac{dn}{dlogE} > 0 \tag{5.19}$$

If this is not the case, the phase velocity and group velocity are the same and

$$v_g = v_p = \frac{c}{n_0}. \tag{5.20}$$

Normal dispersion occurs in the visible spectral region for transparent media when an increase in optical frequency decreases the group velocity.

5.6 Concluding remarks

The times when photons produce photoelectrons in the PMTs, and the times when the photoelectrons are recorded at the digitizer can be corrected for propagation times. This is done by calculating the chi-squared for all the PMTs over all the events and minimizing using ROOT Minuit2. The light observed by the PMTs is affected by the physics processes in the tank like Rayleigh

scattering, which could only be turned off in simulation. The true time calculation is affected by the group velocity of the photons traveling in the detector. Thus propagation time should be calculated using the group velocity of the photons.

6. Results of timing calibration study of IWCD

6.1 Studies using digitized time

Time is one of the most important parameters to be calibrated. The analysis of the time calibration starts from the basic parameters like time, and charge of the observed hits. As mentioned in Chapter 4, time is measured in two ways in WCSim. First the time when photoelectron is produced in the PMT, and second the time at the digtizer after conversion by the electronics. In real data only the final time is recorded at digitizer. Figure 6.1 shows the distribution of time, charge and hits recorded for the 8-inch PMTs in a detector when a conic light source of 100,000 photons is flashed N times at (x=281.6, y=-14.4, z=-13.9) cm.

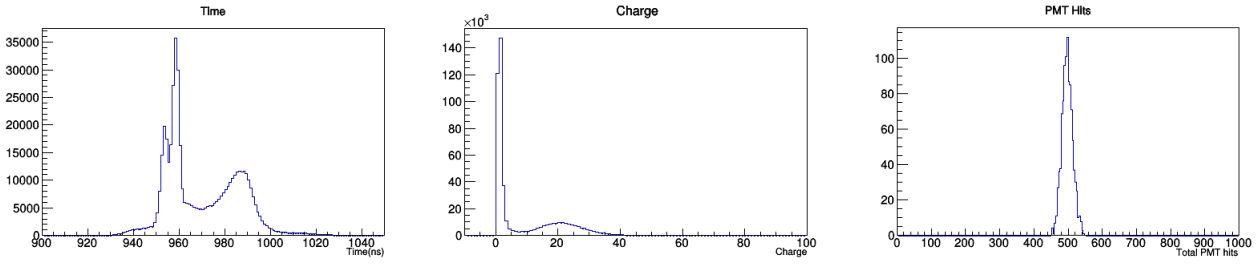

(a) (b) (c)

Figure 6.1: (a) Distribution of time recorded by the digitizer. (b) Distribution of digitized charge recorded by all the PMTs in the detector. (c) Total number of hits observed in all the PMTs during simulation.

The light source used in the simulation to produce Figure 6.1 had an opening angle of 20 degrees and was directed towards the -x-axis. A plot of the hit times observed when a conic light source was facing towards one of the walls of the detector is shown in Figure 6.2. The circle of hits at ϕ=0, y=-1000 cm and from Rayleigh scattering light reaching the PMTs at early times, and the circle of hits at ϕ=π are direct light from the conic source reaching the other side of the detector.

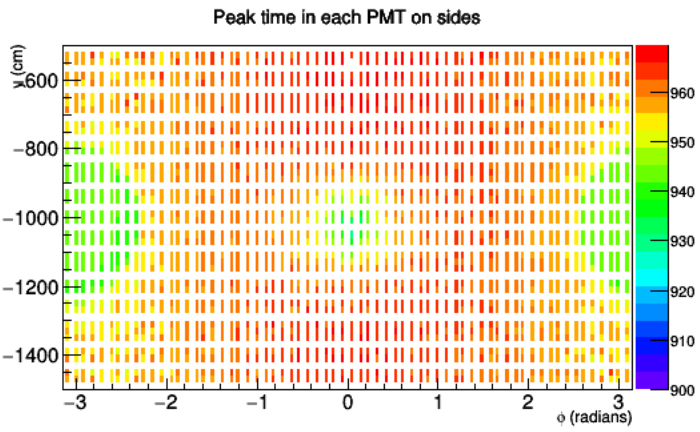

Figure 6.2: Distribution of time observed at the digitizer on the sides of the detector. A conic source of light with an opening angle of 20 degrees was placed at (x=281.6, y=-14.4, z=-13.9) cm in the detector. The source is facing towards the farther side of the detector. Earlier hits are observed at about 920-930 ns at 0 radians and later light in the form of reflections can be seen behind the source between 935 ns and 955 ns.

The choice of the source of light is an important factor for time calibration. The wavelength of the light source should be in the visible spectrum because the PMTs are sensitive to light in the 350-650 nm range. Initial studies were done to make sure the quantum efficiency of the PMT as a function of wavelength were implemented correctly. The rest of the timing calculation studies were done with 400 nm light.

Once the source of light is chosen, it could be placed at different positions in the tank.

6.1.1 Studies with the light source at the center of the detector

For a conic source the light is shone to one direction, and the PMTs facing towards the light source can see the light. The amount of light seen depends on physics of the optical photons. The photons could Rayleigh scatter in the water, be attenuated in the water, reflect, or refract from the acrylic PMT cover on the PMT glass. There could be some reflection from the glass top or the acrylic cover of the PMT.

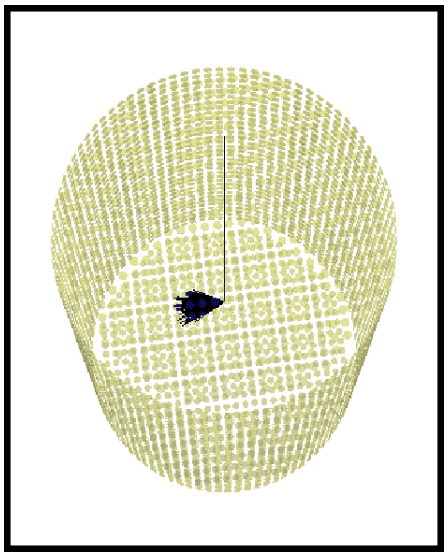

Figure 6.3: Geant4 drawing of the detector with PMTs shown in yellow and photon vectors drawn as black lines. This drawing is for a conic light source in the IWCD.

Studies of the digitized times were done with 8-inch PMTs in the detector. The light source with an opening of 20 degrees about x direction is placed at (x=0.0, y=-14.4, z=0.0) which is almost the center of the detector. The source is placed at the +x-axis near the wall facing towards the -x-axis to the farther end of the detector as shown in Figure 6.3. The source is configured using Geant4 generalized particle source commands in a macro file. Time, charge, and the number of hits distribution observed for this particular location, are shown in Figure 6.4.

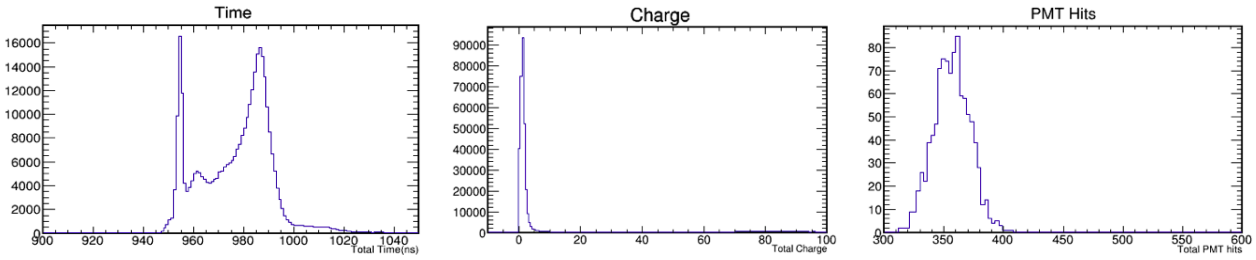

(a) (b) (c)

Figure 6.4: (a) Distribution of time recorded at the digitizer when the source is almost at the center. (b) Charge distribution recorded by all the PMTs for a source at the center of the detector. (c) Total number of hits observed in all the PMTs when a source is located approximately at the center.

Figure 6.4(a) shows that the earliest hits due to the direct light arriving at the PMTs in front of source are seen between 950 ns and 960 ns. There is a small peak at 960 ns that is due to Rayleigh scattering, as discussed in section5.4. The later light in the peak between 970 ns and 995 ns is due to reflected light reaching the PMTs at later times.

6.1.2 Studies of the 8-inch PMTs in IWCD with the source at offset positions

The studies in this detector are done with a conic source as described in the previous section. There are 2844 8-inch PMTs in the detector for these studies (40 per cent photo coverage). This study is done with dark mode ON in simulations, and no corrections to the times were added. First of all the source is placed near the wall of the detector on the positive x-axis, the source is facing the other end of the wall from the farther position.

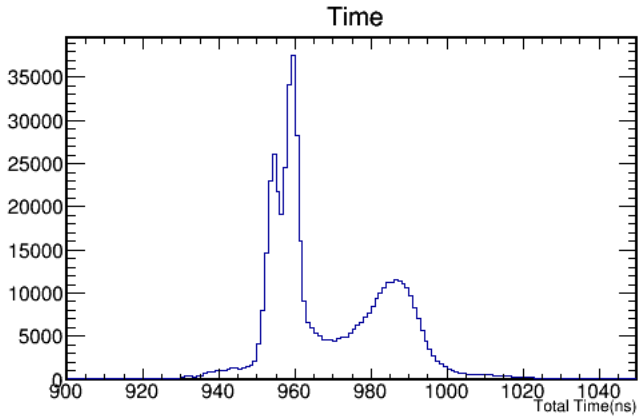

Figure 6.5: Distribution of time at x=290.7 cm

Figure 6.5 shows the source placed at position (x=290.7, y=-14.4, z=-14.3) cm. In time order, the first peak is due to light reaching the closest wall, the second peak is the light reaching the far wall and the broad, short, late peak is due to reflected light.

6.1.3 Timing corrections and isotropic light source

For time calibration, we need to correct the recorded time for the simulation described in 6.1.1. The total time [ref to eqn.5.1] is sum of initial time-offset, propagation time of photons from source

to the PMT, the additional time due to transit in the PMT, and time-offsets added due to electronics and digitizers. The propagation time can be calculated and applied as the first correction to the time. The response of two example individual PMTs can be seen in Figure 6.6. The two PMTs are corrected for propagation time according to their different positions in the detector. The PMTs are hit at different times after propagation time corrections, thus the correction due to electronics delays must be different between the two PMTs. There is a small distribution in time around the peak time which is due to the transit time spread of the PMTs. There is also a small tail at later times due to reflected light. A Gaussian is fit to the main peak and the mean of the Gaussian fit is about a nanosecond earlier than the mean of the histogram as shown in Figure6.6(a).

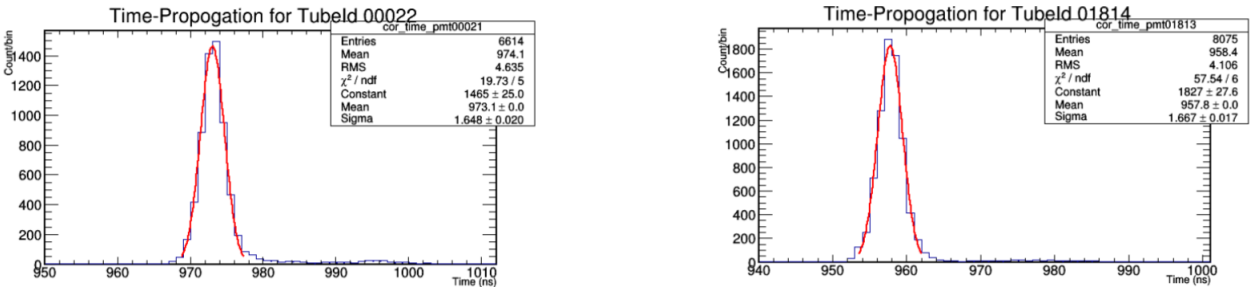

(a) (b)

Figure 6.6: (a) and (b) shows the correction of propagation time applied to the final time recorded at the digitizer for two randomly chosen PMT in the detector. The red line shows the Gaussian fit to the distribution.

Figure 6.7 shows the mean distribution in time in each PMT due to an isotropic source placed at the center of the detector as a 2-dimensional histogram. This figure shows that the light reaches the closer part of the detector before the corners.

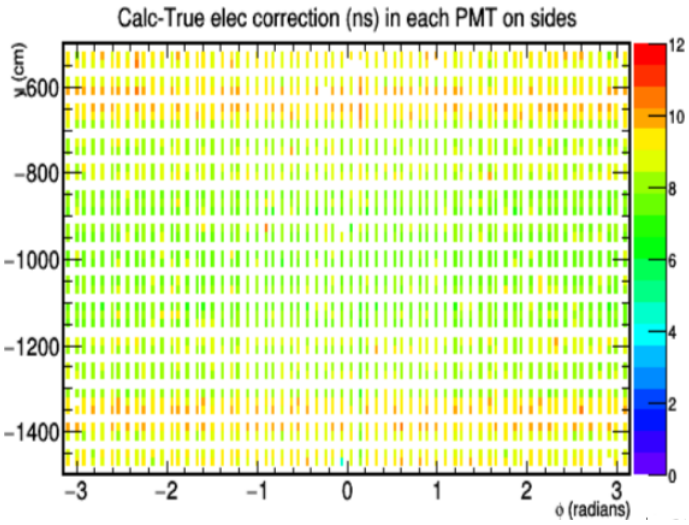

Figure 6.7: Digitizer time in each PMT on the sides of the detector (unrolled view) before the propagation time correction. PMTs observed light isotropically as expected.

The time corrections are applied in the following steps.

1. Correct the final digitizer time for propagation time by calculating.
2. Fit the corrected time distribution to a Gaussian.
3. Get the mean of the fitted peak.
4. Correct for the initial time-offset of the source.
5. Any remaining time offset must be due to electronic delays, which can then be stored in a database and used in subsequent data analysis.
6. Correct for electronic time-offset of each PMT.

After applying these corrections, Figure 6.8 shows the corrected time in the PMTs in the form of a 2-dimensional histogram. As expected the

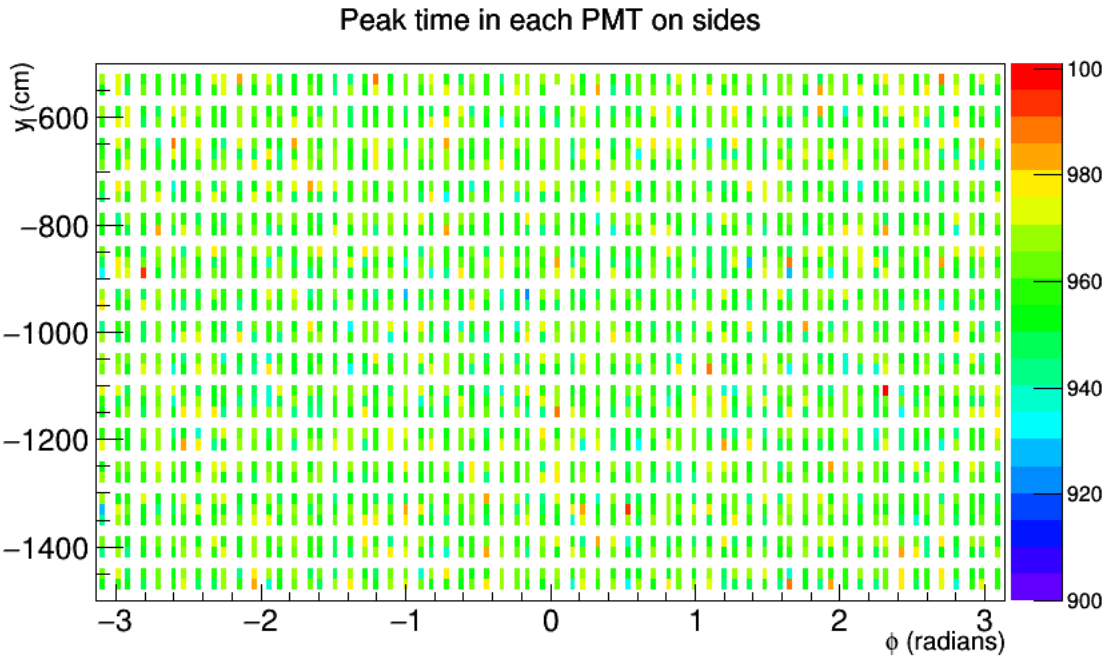

Figure 6.8: Distribution of fully corrected time in each PMT on the sides of the detector.

The fully corrected time is isotropic on the sides of detector, which was not the case in the Figure 6.8.

6.1.4 Studies with mPMTs

In a detector using mPMT modules with 40 per cent photo coverage, there are 15,808 PMTs. The PMTs assembled in modules show the same behaviour as observed for the detector with 8-inch PMT as shown in Figure 6.9. Figure 6.9 is for the corrected times, but as can be seen is non-isotropic throughout the detector. Figure 6.10 shows that the non-isotropic distribution in corrected times is not limited to the sides only but can also be seen on the top and bottom.

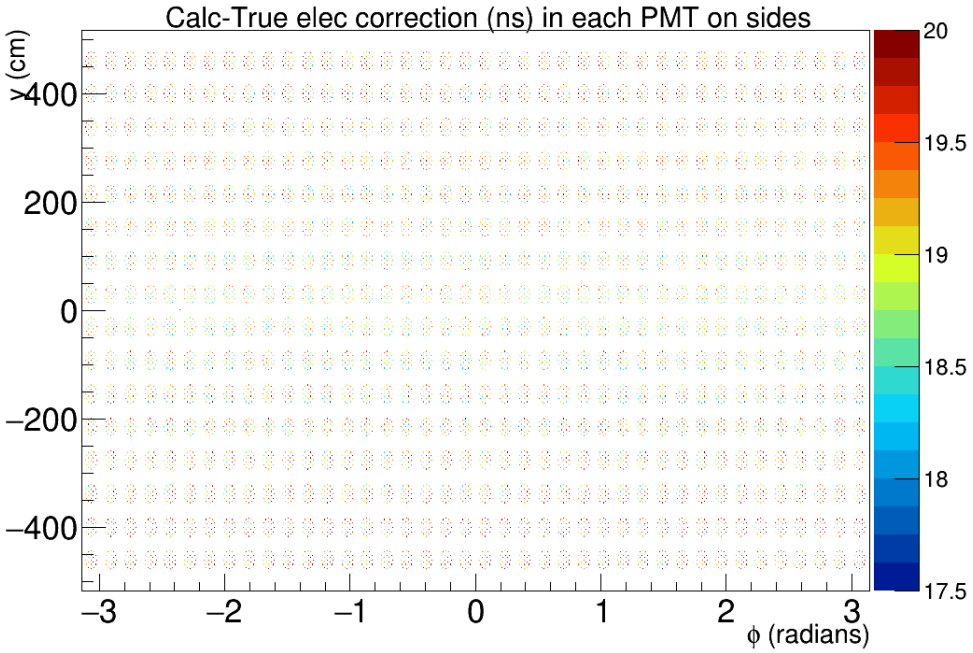

Figure 6.9: Corrected time in each PMT on the side of a mPMT detector. There is an-isotropic distribution on the sides.

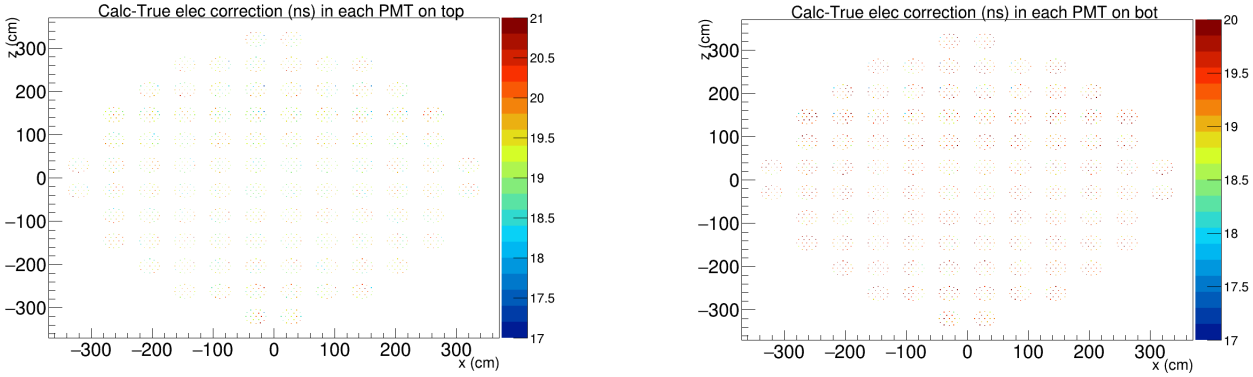

(a) (b)

Figure 6.10: (a) and (b) shows the 2-dimensional histogram with correction of propagation time applied to the final time recorded at the top and bottom in each PMT.

The corrected time of all the PMTs in the detector is shown in Figure 6.11. Most of the PMTs

in the detector have time around 19 ns, but a small number of PMTs were hit later in time. The larger peak at earlier time is fit to a Gaussian giving a sigma of 0.535 $\pm$ 0.003 ns. This is actually in line with the expected transit time spread of the 3-inch PMTs. The PMTs with later hit times are ones near the corners of the detector that see more reflected light than direct light

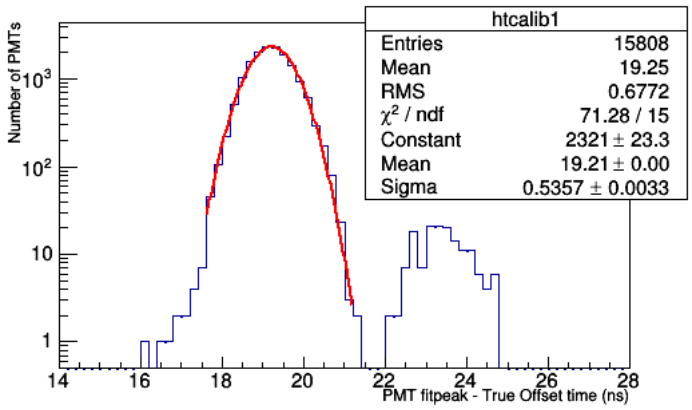

Figure 6.11: Corrected time in all the PMTs in the detector (Logarithmic y-axis).

To investigate the reason for the an-isotropic distribution of corrected digitizer time, the source was placed at different positions.

6.1.5 Studies of the IWCD with source at offset position

Changing the positions of the source changes where the three peaks in the time distribution appear. Figure 6.12(a) shows for the source of light moved to x=218.04 cm. Figure 6.12(b) shows the light source at x=145.4 cm. Figure 6.13(a) shows the time distribution when the light source is at x=72.7 cm and Figure 6.13 shows for the source at the center of the detector x=0.0 cm.

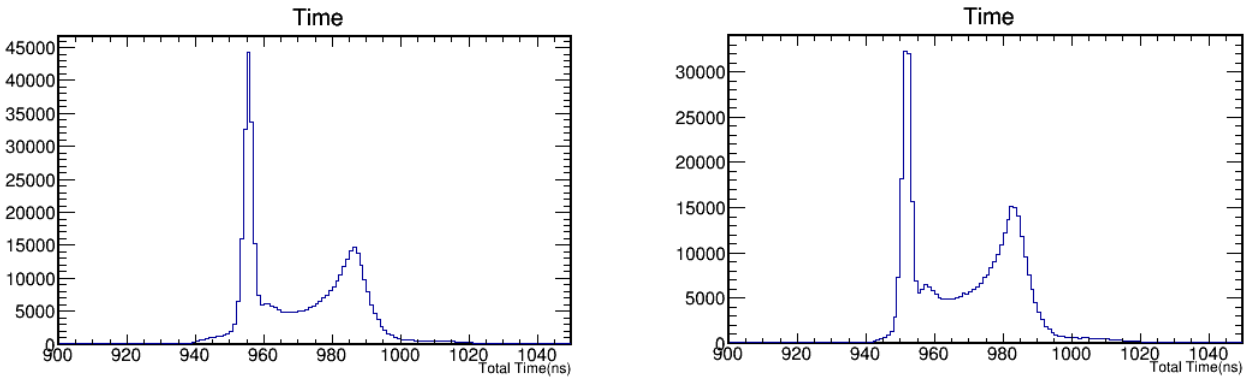

(a) (b)

Figure 6.12: The left panel shows the time distribution when the source of the isotropic light is placed at x=218 cm and the right panel has the light source at x=145 cm.

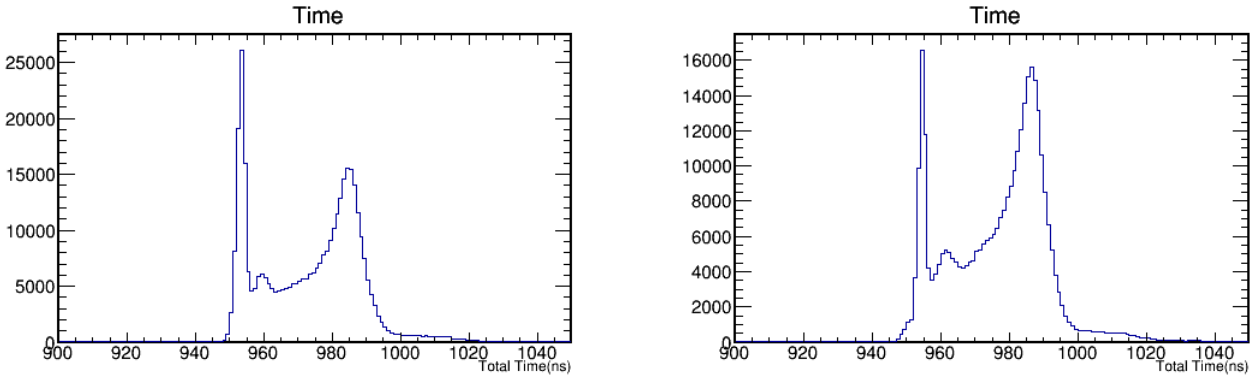

(a) (b)

Figure 6.13: (a), (b) shows the time distribution at x=72.6 cm and x = 0.0 cm respectively.

These plots show that the position of source in the detector makes a difference in the light observed by the PMTs. Looking at these distributions it looks like placing the source near one wall would allow reflected light to be cut more easily.

6.2 Studies of mPMT in IWCD with isotropic source at offset position

Two different positions of a source in the mPMT IWCD detector were studied. Figure 6.14(a) shows the digitizer time response of the PMTs when a source is placed at (x=150.0, y=0.0, z=0.0) cm. Figure 6.14(b) shows the calibrated time when the correction for propagation time, random time-offset of the PMTs and the initial time-offset are applied. The time should be close to zero but the over all global time zero offset is not exactly matching the time in the simulation.

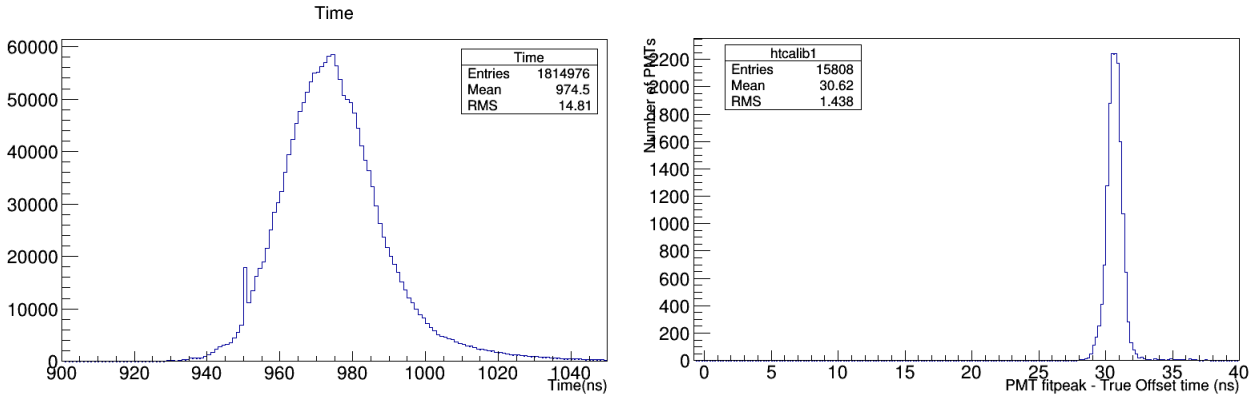

(a) (b)

Figure 6.14: For isotropic light source at (x=150.0, y=0.0, z=0.0) cm.(a)Digitizer time distribution in the all PMTs. (b) Calibrated Time after applying corrections to the final time at the digitizer.

Figure 6.15(a) shows the final time at the digitizer and (b) shows the calibrated time when the light source is placed at(x=150.0, y=0.0, z=0.0)cm.

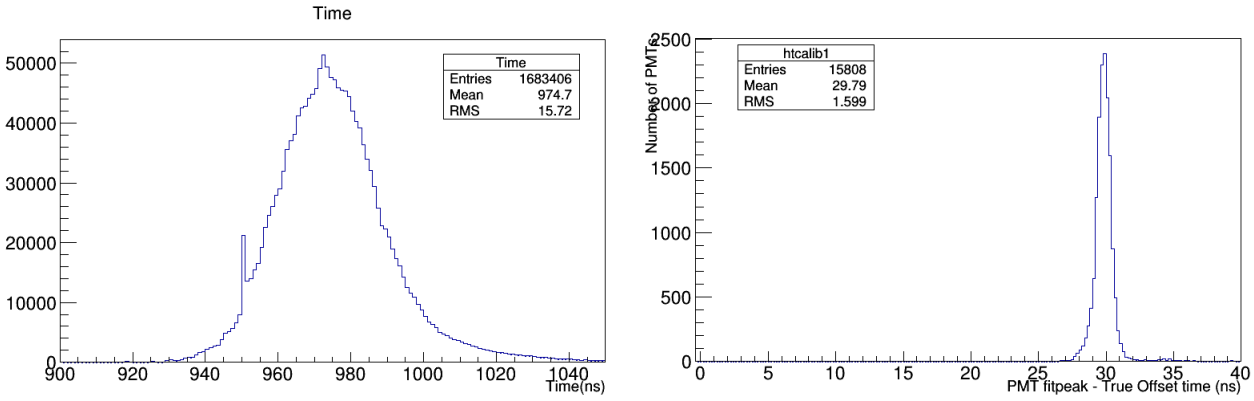

(a) (b)

Figure 6.15: For isotropic light source at (x=225.0, y=0.0, z=0.0) cm. (a)Digitizer time distribution in the all PMTs. (b) Calibrated Time after applying corrections to the final time at the digitizer.

Moving the light source to two different positions in the tank did not make a significant difference in the time observed at the digitizer. This is because the source is isotropic, and the PMTs all around the tank observe light.

6.2.1 Minimization of time using chi-squared

After studying the behaviour of the PMTs with the isotropic light source placed at different positions, the chi-squared given by equation 5.1 is minimized. The minimization routine discussed in section 5.2 is used to determine the source position, group velocity of the light and electronic time-offset for each PMT. The fit was done using 200 light flash events of 2,00,000 photons.

The corrected time distribution in each of the PMTs has a peak and a few later hits from a scattered light, which can be seen in Figure 6.16

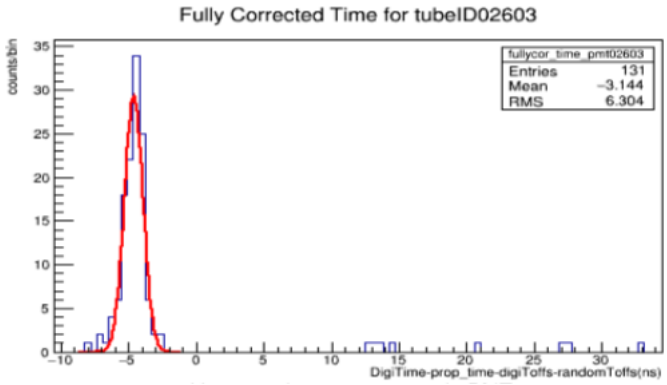

Figure 6.16: Distribution of corrected digitizer time in a randomly chosen PMT ID-02603. Red line shows a fit with Gaussian.

The later times are ignored, since they are from scattered light and only the time from the main peak of the corrected time distribution of each PMT is used in the minimization. Figure 6.17 shows the number of times that each PMT recorded charge for 200 light flashes.

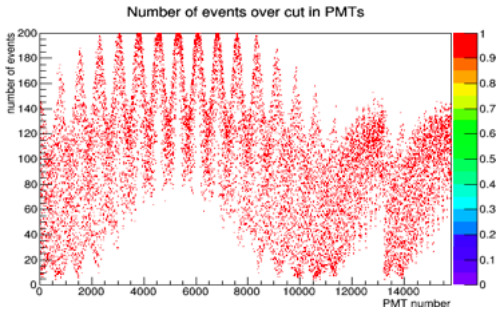

Figure 6.17: Number of times each PMT recorded a hit in 200 light flash events.

A study was done to look at the effect of putting a cut on the minimum number of hits in the PMTs being used in the minimization. This is done by looking in the number of events in each PMT. The position of the source (x, y, z), initial time-offset, and refractive index were minimized first and then the random time-offset of PMTs are minimized. Minimum of the chi-squared is expected to occur when the source is at the simulated source position. The corrected time is

calculated, the sigma is set to one, and we don't divide by the total number of PMTs or events, as we want to first study the distribution at every 10-th cm between the $\pm$ x-axis extents of the detector for all the PMTs and all the events.

All of the studies were done with the source of light placed at position (x=150.0, y=0.0, z=0.0). Figure 6.18 shows the plot for corrected digitizer time squared as a function of position. Figure 6.19(a) shows the corrected digitizer time versus the position between $\pm$x-axis extents. Figure 6.19(b) shows the projection of y-axis of corrected digitizer time for the simulated source position, where

$$\text{Corrected Digitizer Time} = t_i^j - (t_0 + t_{elec}^j + \frac{|\vec{r}_s - \vec{r}_{PMT}^j|}{v_g} n) \tag{6.1}$$

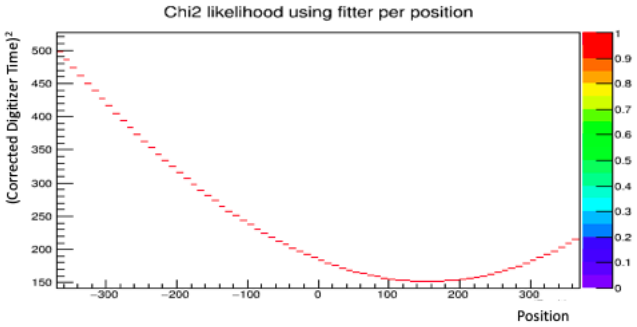

Figure 6.18: Scan of chi-squared for source x position over the extents of the detector using all of the data with all PMTs included.

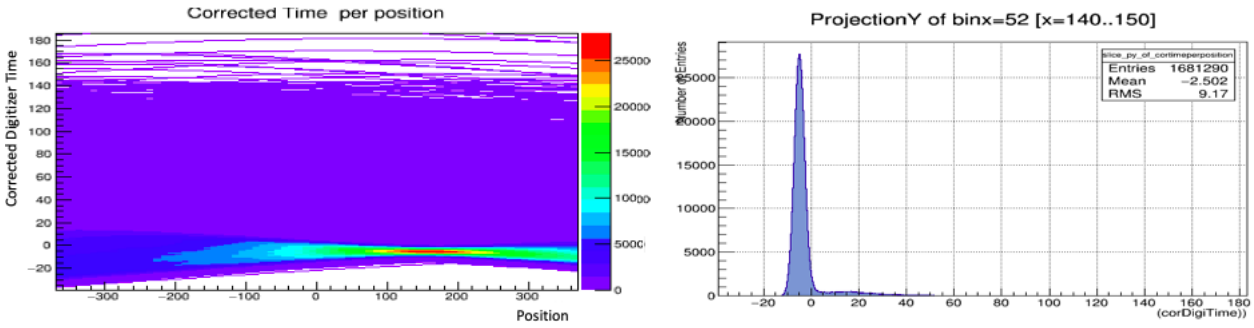

(a) (b)

Figure 6.19: (a) Two dimensional distribution of corrected digitizer time in all PMTs versus the source position. (b) Projection of y-axis (Corrected digitizer time) for the simulated position (x=150.0) cm.

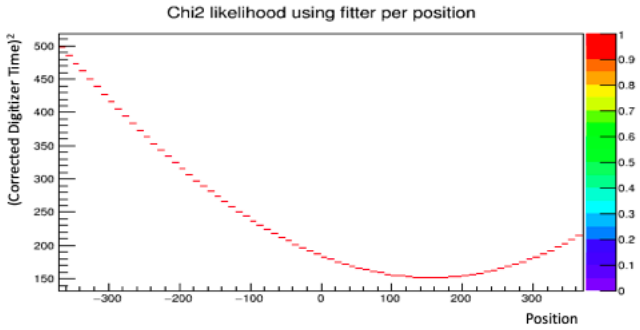

Figure 6.20: Scan of chi-squared for source x position over the ± extents of the detector with PMT having more than 50 events using all the data.

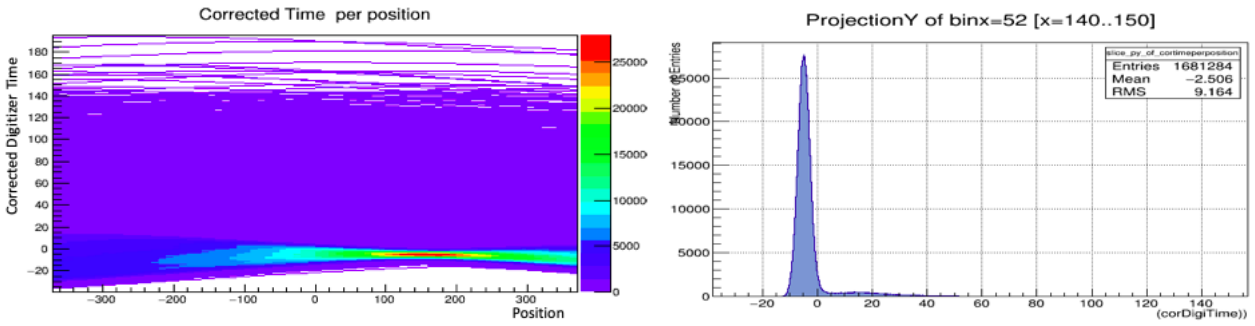

(a) (b)

Figure 6.21: (a)Two dimensional distribution of corrected digitizer time in all PMTs versus the source position. (b) Projection of y-axis (Corrected digitizer time) for the simulated position (x=150.0) cm.

The minimum of corrected digital time squared changes when the cut over number of events to include a given PMT is made. The distribution of corrected digital time when the source is placed at the expected position (x=150.0) cm has a Gaussian with a shoulder to more negative times. The mean is expected to be closer to zero, whereas it becomes more negative as the cut over PMTs is restricted tightly. As might be expected by looking at Figure 6.17, putting a cut on minimum number of hits in the PMT, selects a biased sample of PMTs which give rise to these changes. It is recommended to use all the PMTs in the fit.

After the studies of Figure 6.18 - 6.21 were completed, it was found that the digitizer time is not calculated relative to the source t in the detector but it is calculated relative to the first PMT in the detector that got hit. A chi-square calculation with that effect accounted for is given by:

$$\chi^2 = \sum_{i=0}^{N_{flash}-1} \sum_{j=0}^{N_{PMT}-1} \frac{1}{N_{flash} N_{PMT} \sigma_{t_0}^2} \left(t_0 - t_{i,j} + t_{elec}^j + \left(\frac{|\vec{r}_s - \vec{r}_{PMT}^j|}{c} n - \frac{|\vec{r}_{closestPMT}|}{c} n\right)\right)^2. \quad (6.2)$$

This chi-squared is used to study the timing calibration. The cut over events is removed as it was found to introduce further bias.

Figure 6.22 (a) shows the Corrected Digitizer Time as previously defined, but including additional offset to first PMT hit for the source placed at the center of the detector. Projection of Figure 6.22 (a) onto the y-axis at x=100 cm is in Figure 6.22 (b), at x=0 cm is in Figure 6.22 (c) and at x=100 cm is in Figure 6.22 (d). Figure 6.23 is the same set of plots as Figure 6.22 but for the light source at x=150 cm.

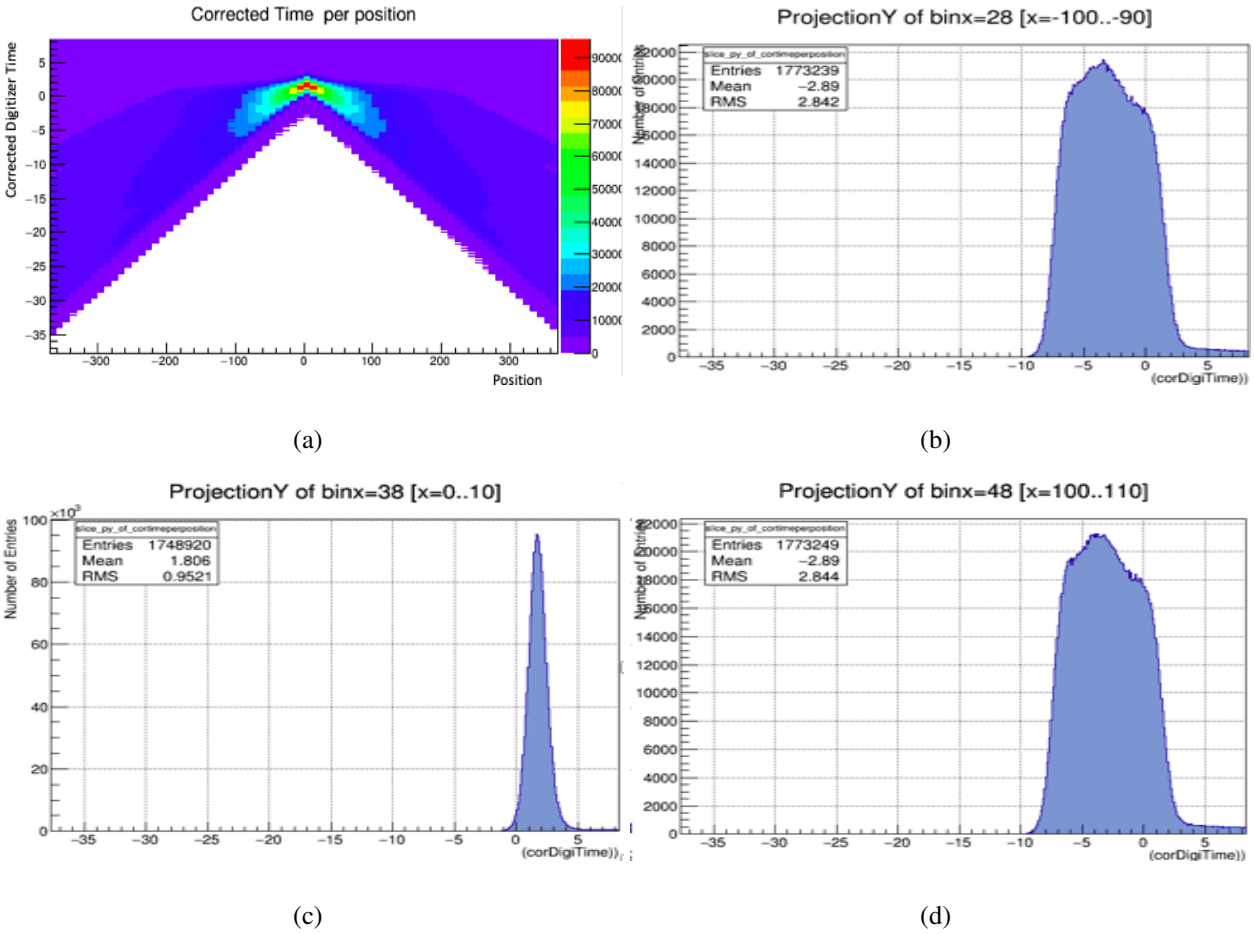

Figure 6.22: (a) Two-dimensional histogram for the corrected time versus the source position when a source is simulated at the origin. (b) Projection onto the y-axis (corrected digitizer time) for positions x=90-100 cm. (c) Projection onto the y-axis (corrected digitizer time) for the position (x=0-10) cm. (d) Projection onto the y-axis (corrected digitizer time) for positions x=100-110 cm.

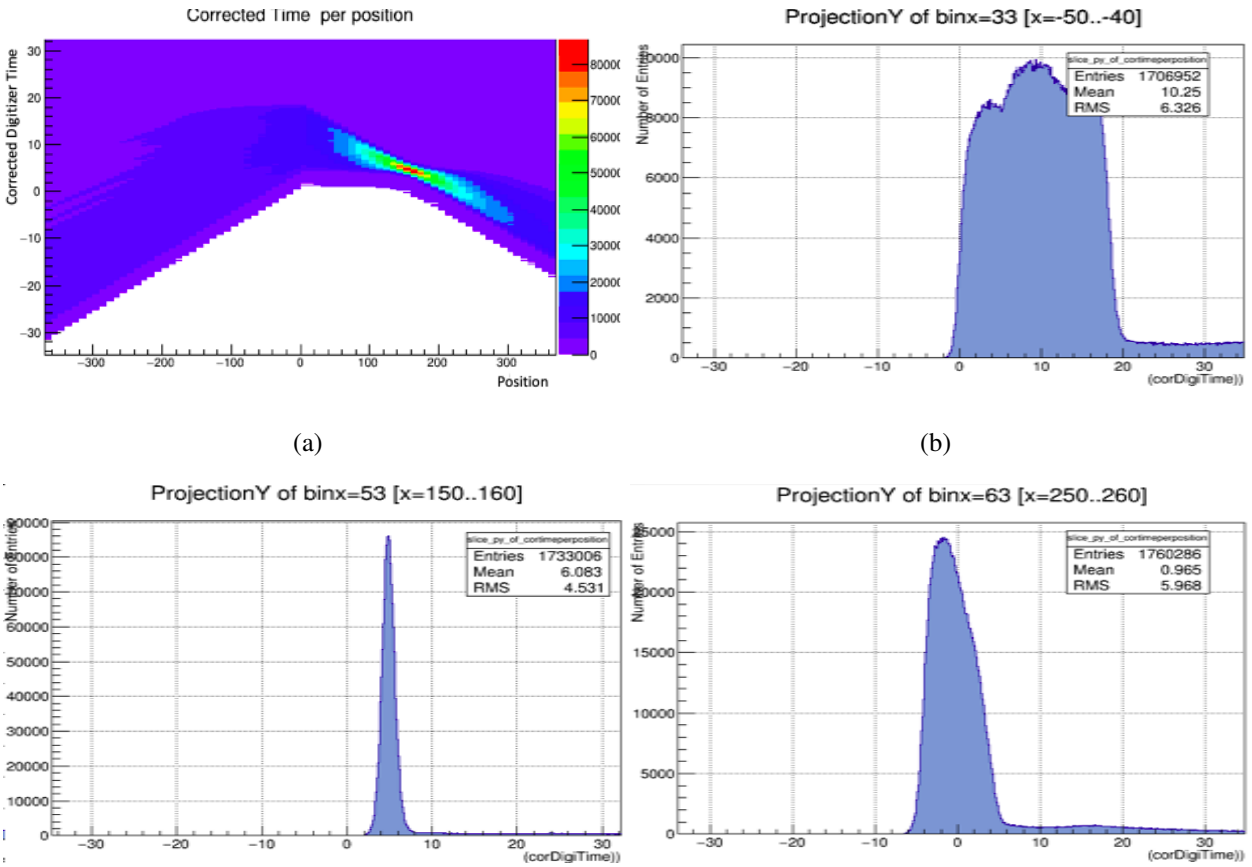

Figure 6.23: (a) Two-dimensional histogram for the corrected time versus the source position when a source is simulated at x=150 cm. (b) Projection onto the y-axis (corrected digitizer time) for positions x=40-50 cm. (c) Projection onto the y-axis (corrected digitizer time) for positions x=150-160 cm. (d)Projection onto the y-axis (corrected digitizer time) for positions x=250-260 cm.

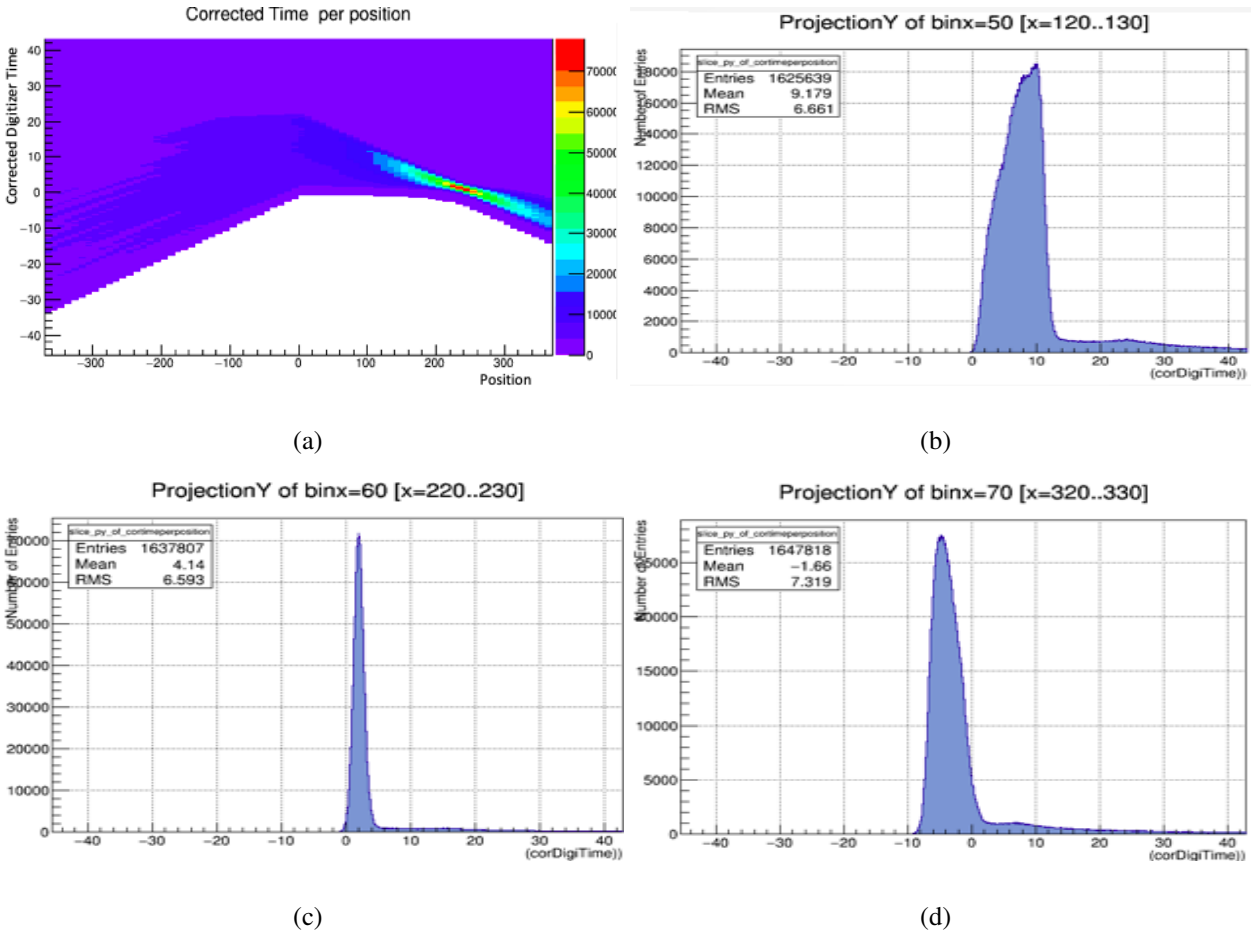

Figure 6.24: (a) Two-dimensional histogram for the corrected time versus source position when a source is simulated at x=225 cm. (b) Projection onto the y-axis (corrected digitizer time) for positions x=120-130 cm. (c)Projection onto y-axis (corrected digitizer time) for positions x 220-230 cm. (d)Projection onto the y-axis (corrected digitizer time) for positions x=320-330 cm.

Looking at different positions, using the newer calculations removed the shoulder from the corrected true distribution and narrowed it.

6.3 Studies using true time

This section will study the timing calibration up to the PMT when a photoelectron is produced in the PMT before it is actually recorded by the digitizer. This time is known as true time. The time taken by electronics to read out the photoelectron capture is not part of these studies. Thus random time-offset of PMTs is zero for all. The true time distribution and corrections applied were

already shown in Figure 5.5.

6.3.1 minimization of the chi-squared

The chi-squared in this study is given by:

$$\chi^2 = \sum_{i=0}^{N_{flash}-1} \sum_{j=0}^{N_{PMT}-1} \frac{1}{N_{flash} N_{PMT} \sigma_{t_0}^2} \left(t_{i,j}^{true} - \left(\frac{|\vec{r}_s - \vec{r}_{PMT}^{\,j}|}{v_g} - t_{elec}^{j}\right)\right)^2. \tag{6.3}$$

The time due to electronics is kept zero for all PMTs, shown in distribution in Figure 6.25.

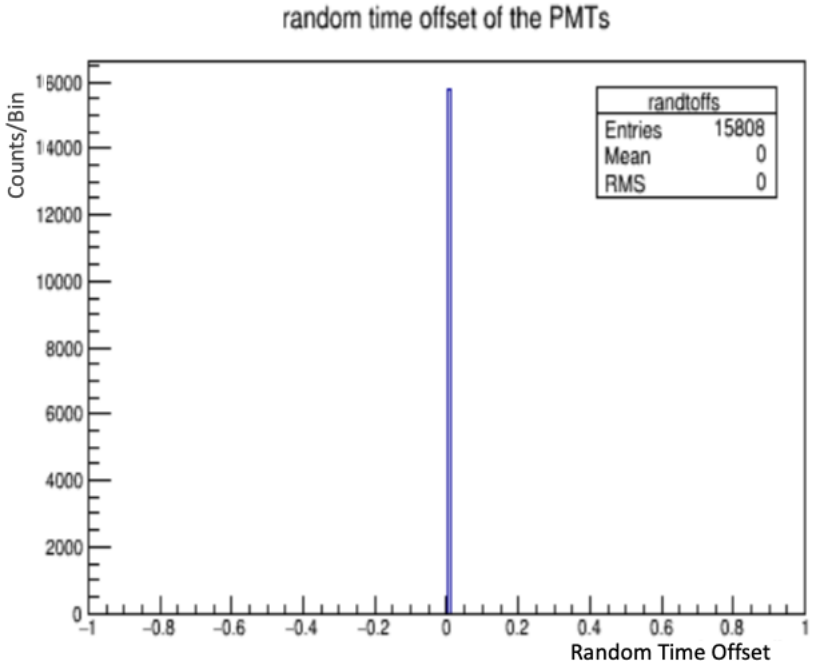

Figure 6.25: Time distribution representing the random time-offset of the PMTs. For true time the random time-offset was set to zero for all PMTs.

The minimization strategy as described in section 6.2.1 is used. First of all the source position (x,y,z), group velocity and propagation time-offset are fit. Using these minimized values, the random time-offsets of the PMTs are determined by minimization of the chi-squared (which are zero initially). The above two steps are repeated for desired number of times by using the last

minimized values of parameters. The minimized random time-offsets were calculated for two different datasets that differ only in the location of the light source.

Figure 6.26 shows the distribution of the minimized time differences after each 5 iterations going from (a) to (e). Figure 6.26 is for the light source placed at x=150 cm. Since the initial parameters are already close to the minimum χ^2, there is very little difference between the distribution as more iterations are done. The width of the time distribution, in this ideal case is still not a delta function. As we will see with further calculation most of the remaining width in this distribution (0.06 ns) is due to the uncertainty on where on the PMT face the photon hits. The fitted source as a function of iteration is shown in Figure 6.28. There is a small (6 mm) found after minimization in the source position at position (x=150.0, y=0.0, z=0.0) This is an offset position of the source from the center in the tank. The minimization routine was iterated for 5 times by using the parameters minimized in last iteration. Figure6.26 (a), (b), (c), (d) and (e) shows the minimized random time-offset over 5 iterations using the last minimized parameters.

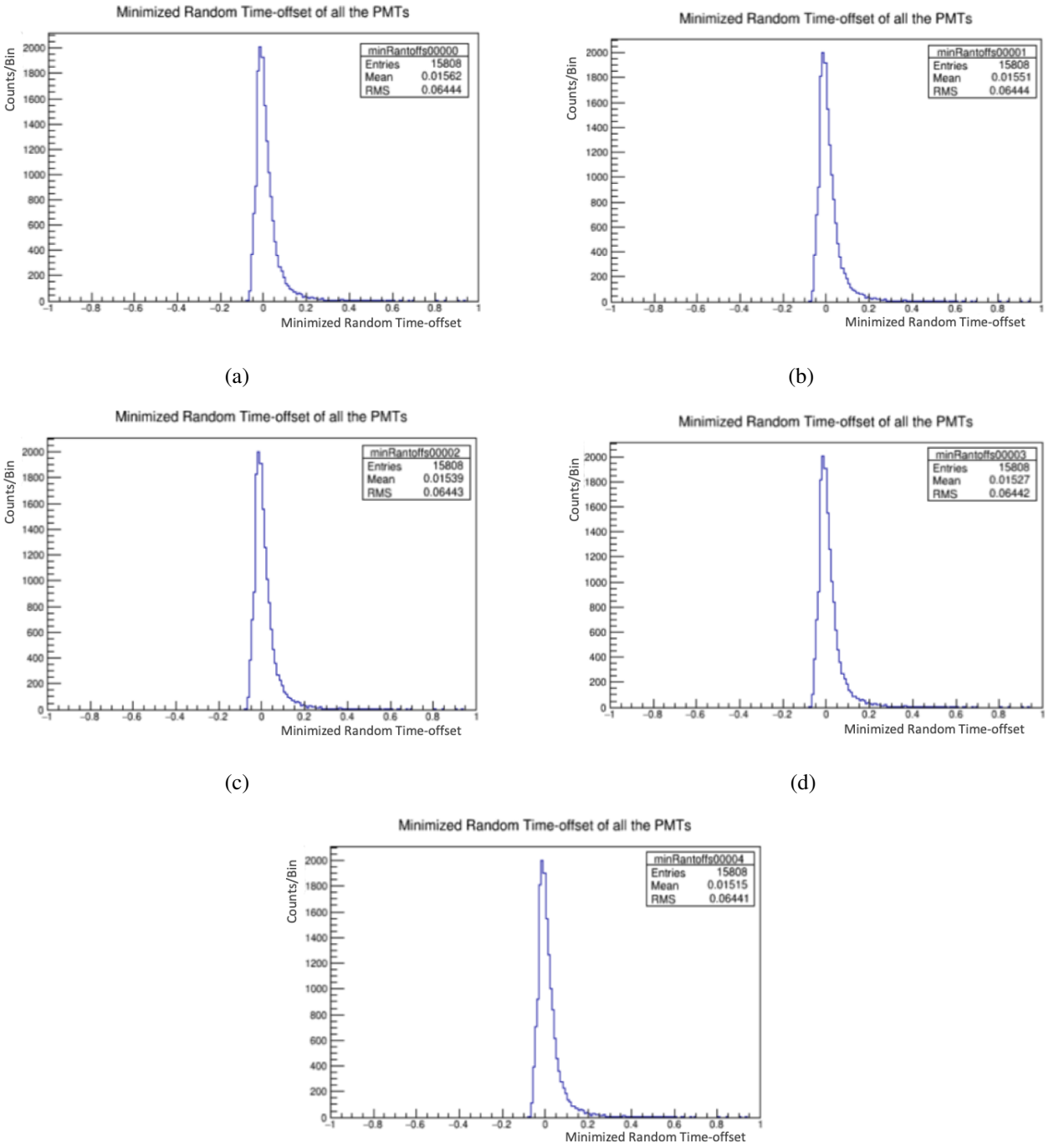

Figure 6.26: Corrected time after minimization of all the PMTs over subsequent 5 iterations.

The process was repeated with a source placed in the center of the detector. The mean remained

same over 5 repeated iterations. Figure 6.27 shows the distribution over one of the minimized iterations.

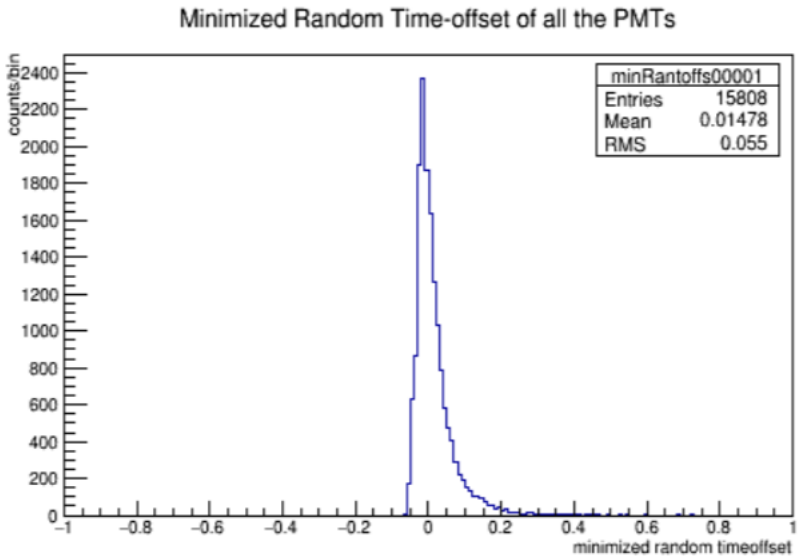

Figure 6.27: Corrected time after minimization of all the PMTs over an iteration when a source is placed at (x=0.0, y=0.0, z=0.0).

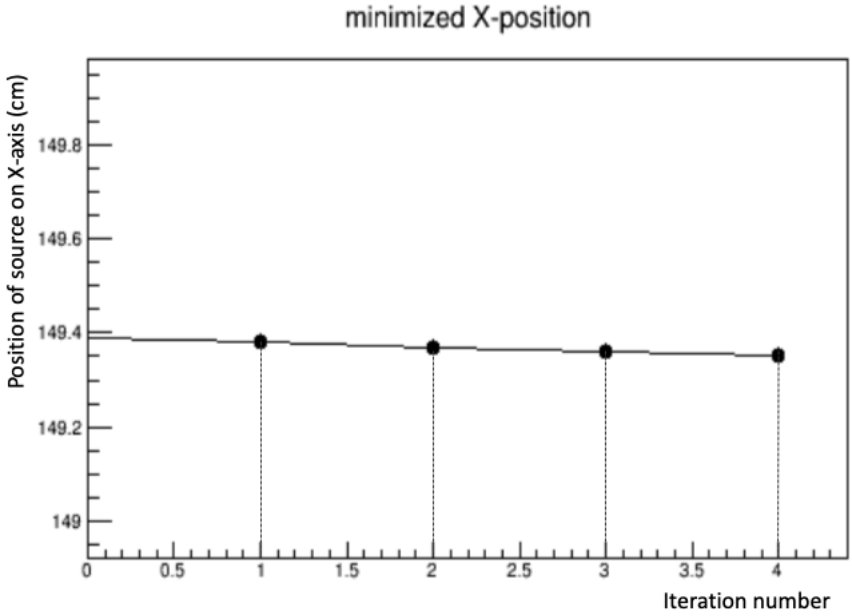

Figure 6.28: Fitted position of the source as a function of iteration. The true source position was 150 cm in x.

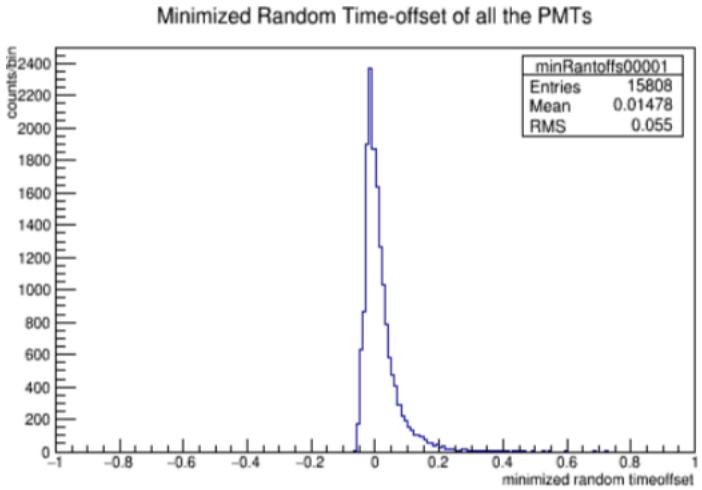

Figure 6.29: Distribution of random time offset i.e. fitted digitizer time offset (which should be zero) of all the PMTs observing light from an isotropic source placed at center.

Figure 6.29 is the same as Figure 6.26, but it is for the isotropic source placed at the center of the detector. The width of the distribution is identical showing that central position does not effect

the results.

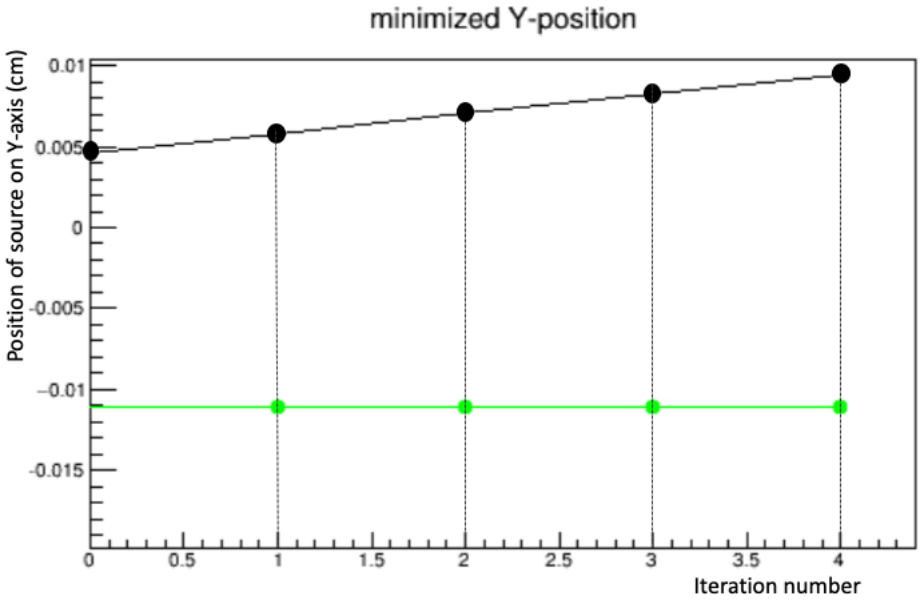

(a)

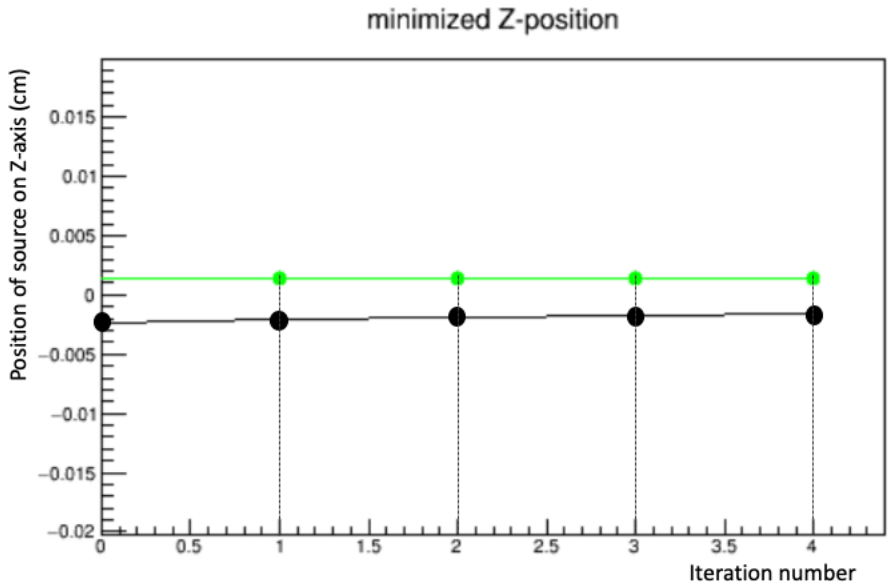

(b)

Figure 6.30: (a) and (b) shows the minimized values of position Y and Z respectively after each iteration for the light source true position at the origin.

The position of the source, group velocity and the propagation time-offset are also minimized. Figure 6.30 (a) and (b) show that there is very little bias in the parameters obtained from the first minimized Y and Z position respectively compared for a source simulated at two different positions. The figure shows the results for the fit using two different datasets, one with the light source at the origin and the other with light source at x=150 cm. Figure 6.31 shows the comparison of the fitted group velocity as a function of iteration for the two different simulated positions. Figure 6.32 shows the minimized values of propagation time as a function of iteration

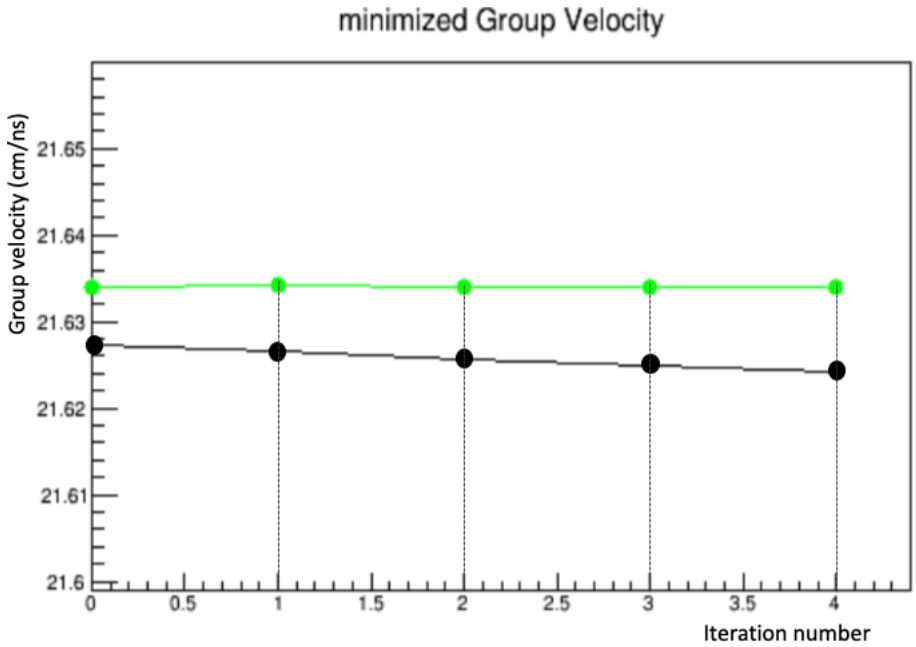

Figure 6.31: The graph shows the minimized values of the group velocity over 5 iterations with green for position (x=0.0, y=0.0, z=0.0) and black for (x=150.0, y=0.0, z=0.0)

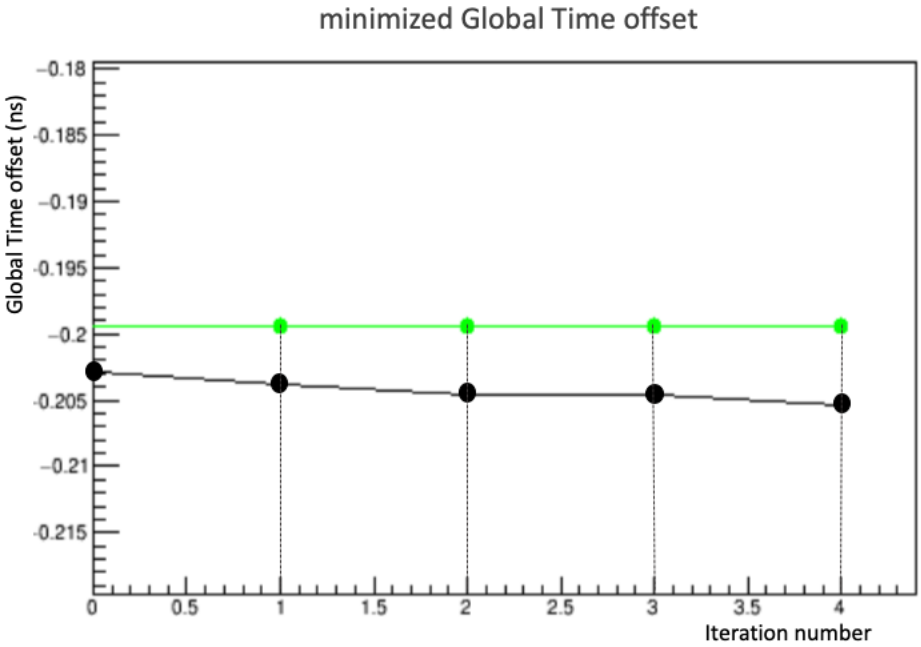

Figure 6.32: Green line shows the best fit global time-offset as a function of iteration for the light source at the origin (green) and at x=150 cm (black) when a source is simulated at (x=0.0, y=0.0, z=0.0) cm. The black line shows the minimized values of propagation time over 5 iterations when a source is placed at (x=150.0, y=0.0, z=0.0) cm

6.3.2 Determining the exact hit position of the photon on the PMT cathode

The corrected true time shows a negative bias [ref. Figure 5.6]. This bias has been forced to be due to the calculation used for the propagation of the photon to the PMT using the distance between the center of the PMT (the default hit position of the photon in the PMT in WCSim) and the source of the light. Instead of using the default hit position, the photon hit position is calculated on the basis of where the light source is placed in the detector and the direction the PMT is facing. The PMTs in an mPMT module face in the outward direction of the module. In some parts of the detector PMTs can only see part of the light. If the light source is in the center of the detector, then the modules on the top and the bottom of the detector have some PMTs which could see significantly less light. Then from the center of the PMT. The studies show the calculation of the distance between the light source and the PMT position where the light hit, instead of the center of the PMT.

Figure 6.33 shows the geometry used for calculation of exact hit position of the photon on the surface of the PMT. PMTs face in $\hat{n}$ direction and not towards the source of the light. The distance between the source and the center of the PMT is calculated relative to the center of the detector as:

$$\vec{r_n} = \vec{r}_{PMT} - \vec{r_s} \tag{6.4}$$

The distance from the source to the center of the PMT sphere with a radius R facing direction $\hat{n}$ is,

$$\vec{r_c} = \vec{r_n} - R\hat{n} \tag{6.5}$$

Thus the distance between the source and the closest point on the PMT is given as:

$$\vec{r'}_c = \Big(\frac{r_c - R}{R}\vec{r_c}\Big) \tag{6.6}$$

The magnitude $|\vec{r'}_c|$ is used to calculate the distance between the PMT and source instead of using $|\vec{r}_n|$. The angle of the light source relative to the PMT normal is calculated from cosθ = -($\hat{n} \cdot \hat{r'}_c$). The angle from the PMT normal to the edge of the cathode is β = $cos^{-1}\big(\frac{R-d}{R}\big)$. When $\theta < \beta$, the PMT sees direct light.

The chi-squared calculation with all of the correction to the true time becomes:

$$\chi^2 = \sum_{i=0}^{N_{flash}-1} \sum_{j=0}^{N_{PMT}-1} \frac{1}{N_{flash}N_{PMT}\sigma_{t_0}^2}\big(t_{i,j}^{true} - t_{elec}^{j} - \frac{\vec{r'}_c}{v_g}.n\big)^2. \tag{6.7}$$

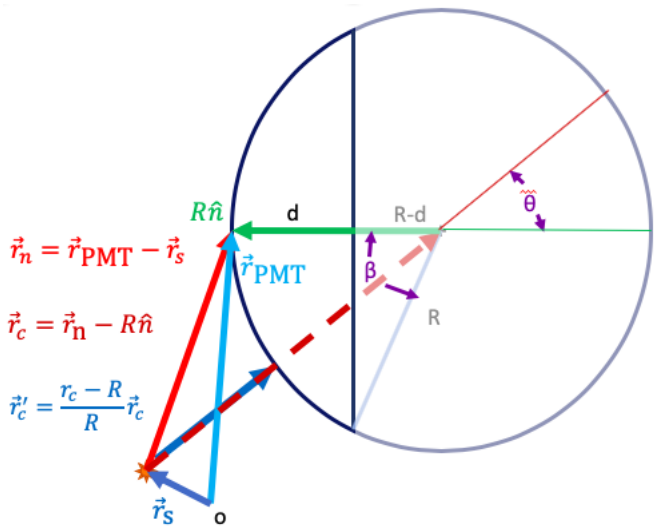

Figure 6.33: Geometry of photons from a source at $\vec{r}_s$ reaching the PMT cathode at $\vec{r}_c'$.

The time difference between photons reaching closest points on PMT and the cathode center, averaged over isotropically thrown photons at the center of the detector. Figure 6.34 shows the delta times for the shortest distance travelled by the photons in all the PMTs when simulated for 10000000 photons thrown isotropically from the center of the detector. The simulation simply calculated the integration between randomly divided lines (photons) and spheres (PMTs) travelling in a straight line intersecting with sphere, that is, PMTs.

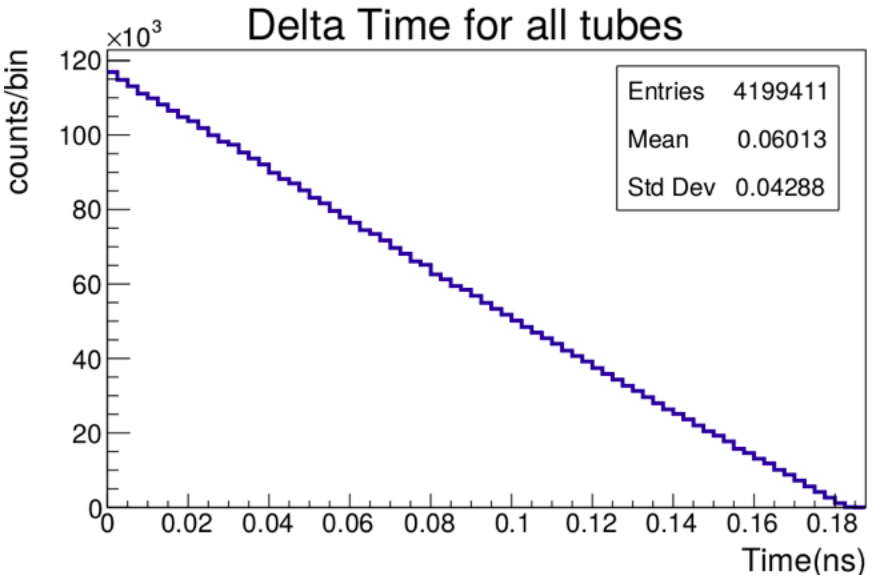

Figure 6.34: Delta time distribution for all the PMTs in the detector when calculated for the shortest distance travelled by a photon from a source to the PMT where it actually hit.

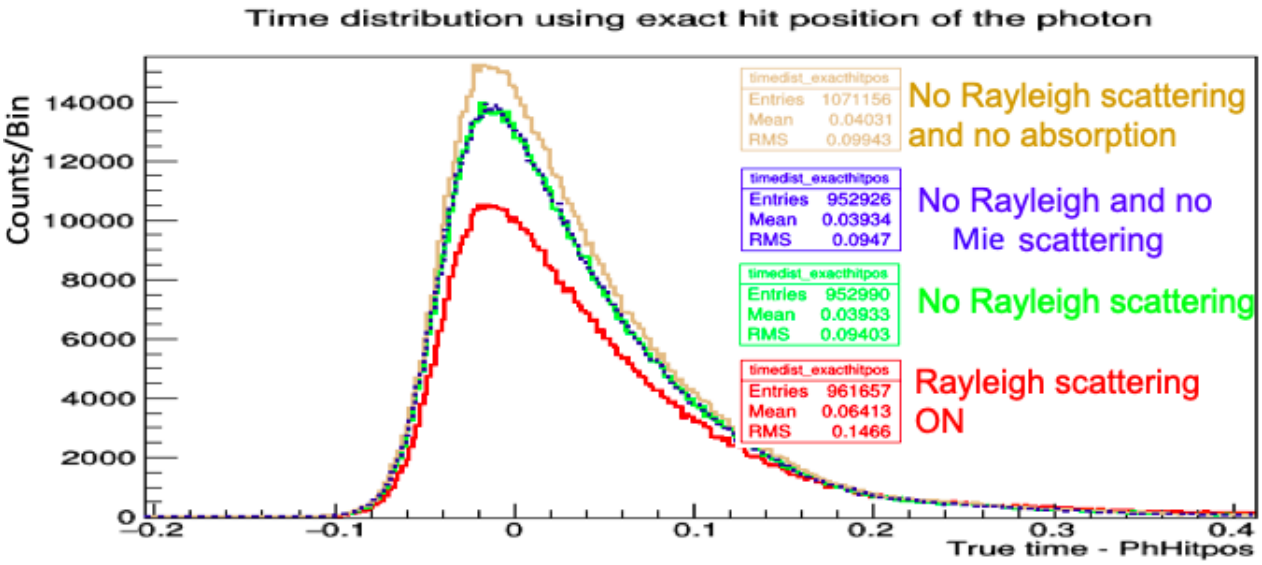

Figure 6.35: Corrected true time distribution including the exact hit position time correction. The golden curve shows the true time distribution if no absorption and Rayleigh processes are involved in the simulation. Blue distribution is for Rayleigh and Mie scattering exclusive processes. Green distribution overlaps the blue distribution when only Rayleigh scattering is turned off. Red distribution appears when the Rayleigh scattering process is involved in the simulation

Figure 6.35 shows the corrected true time introducing the newly calculated corrections. This Figure also shows the effect of timing of Rayleigh scattering, absorption, and Mie scattering. When there is no absorption or Rayleigh scattering in the simulation, then the RMS is more than in the other cases. The correction using newer calculations increases the RMS value, but the mean is closer to zero when compared to red distribution in Figure 5.6.

6.4 Concluding remarks

A light source was placed at various positions in the detector. A conic light source produced two peaks of light showing the prompt hits observed in the PMTs in front of the source and the late light seen at the back of the source. The peaks shifted as the source moves closer or away from the PMTs. The isotropic source showed the light in the detector in a cylindrical strip around the sides of the detector. The height of the detector is more than the diameter of the detector, and the PMTs further away from the source see the light late.

The corrections are made to the true time and digitizer time, and a minimization of the chi-squared is done to determine the optical parameters. The digitizer time is studied first at different positions. A study using a cut on the number of PMT hits was conducted. The studies showed that the corrected digitizer time using all the PMTs has a negative bias in time. Further investigations determined that the digitizer time for a PMT is not calculated from the source, but rather is calculated from the first PMT got hit in the tank. These calculations removed the negative bias. But the corrected digitizer time is not a Gaussian centered at zero in the distribution.

The true time was studied for better understanding of time. The source position, propagation time-offset, group velocity and the random time-offset(that is zero in case of true time) for all the PMTs was minimized. The minimization of random time-offset showed that the random time-offset is a Gaussian centered at zero and it does not change significantly on subsequent iteration of the fit. The studies are taken further by studying the exact hit position of the photon on the surface of the PMT instead of using the regular calculation of propagation time-offset. These calculations show a mean of distribution to be best at 0.04 ns with RMS value of 0.099 ns.

7. Conclusions

The thesis described the timing calibration of IWCD using two different kind of PMTs, i.e., 8-inch and 3-inch PMTs. In addition to timing calibration other studies of physics processes of optical photons in water were carried out.

Measurements of neutrino oscillations will be limited by systematic uncertainties. The IWCD is planned to reduce the systematic uncertainties in neutrino oscillations measurements. The PMTs used in the upcoming detector must be well-calibrated for precise measurements. Thus the photosensor test facility at TRIUMF provides a platform and facilities to test the PMTs and test the environmental affects on the PMTs. The 20-inch PMT used in Super-Kamiokande detector is the first PMT studied in the facility. The gain and the efficiency show a periodic banding due to temperature affecting the amount of light reaching the PMT. Applying a temperature correction clears the periodic banding.

The design of the IWCD is being studied using Geant4 and (WCSim). The simulation can detect the time when a photoelectron is produced in the PMT and the time when the the charge is registered by digitizer. The cylindrical detector is simulated with two different kinds of PMTs. The earlier studies are done with 8-inch PMTs and later 3-inch PMTs are also simulated. The light travelling in the tank is affected by various physics processes (Absorption, Rayleigh scattering, and Meigh scattering). The digitizer time is observed to have more prompt hit times when the source is at the far end facing towards the wall and fewer hits at late times due to reflections. The prompt hit time decreases with a rise in the late light as the source moves closer to the wall.

An isotropic source is placed in the center of the detector to have light reach as many PMTs as possible. From this location light does not directly reach at the corner joining the sides to the top and the bottom of the detector. The digitizer time on each PMT appears as a single Gaussian distribution with mean related to how far away the PMT is from the isotropic light. The digitizer time is corrected for light propagation time by minimizing a time difference χ^2, which includes a random time-offset due to electronic delays. The minimization uses Minuit2 and MIGRAD. These

studies conclude that including fewer PMTs in the fit moves the fitted position of the source away from the simulated position. Thus all of the PMTs should be used in doing the minimization. The propagation time in WCSim is calculated relative to the first PMT got hit in the detector, which moves the distribution to negative time rather than centered at zero.

To study the simulation the true time of the PMT was used. A chi-squared fit for the position of the source in x, y and z, group velocity, propagation time-offset, and random time-offset (i.e. zero for true time studies). The time-offsets determined by the fit are Gaussians centered at zero, which is the expected result. The trend of minimized source positions remains very close to the simulated source position. The minimized group velocity matches the one in the simulation.

To be more precise calculations for the exact hit position of the photon are done to the surface of the PMT. The calculations are done using the position of the PMT from the WCSim, which determines the center of the PMT as the hit position. Instead of using the WCSim position, the position closest to the light source on the PMT surface is used. Using this hit position and turning off the Rayleigh scattering and absorption process in the detector leads to the mean of the corrected time to be 0.0403 ns and the RMS of 0.099 ns. This RMS value is comparable to the difference in the time (ns) between different locations on the face of the PMT.

There are still a few studies that need to be carried out to develop the timing calibration for the IWCD. The fits have been shown to converge when starting at the expected timing offsets, however in the real data there will be unknown timing offsets. Studies of how the fits behave when given the wrong starting point should be made. Also, the studies have been carried out using true time information. It should be studied how the answer changes as the true times are smeared to different levels (from perfect to about the level expected from the PMTs being decided amongst). Finally, the fits should be performed using the digitized times.

Additional systematic tests should be carried out to see if we can also learn about the water properties. For example the real detector may have a different attenuation, amount of Rayleigh scattering depending on where you are in the detector. SK for example sees a difference in behaviour at the bottom of the detector relative to at the top. It would be interesting to put in position

dependent water properties and see if the fit can see these differences.

Another aspect of these studies that could be done is to find additional locations where the light source should be placed for different uses. The isotropic source at the centre of the detector works well for the timing calibration of many of the PMTs, but PMTs at the top and bottom of the tank may need additional data with the light source moved closer to the top or bottom of the tank.

The cone light source was initially studied, but additional studies with a cone light source on the sides of the tank should be done. This type of light source has been installed in SK by the UK group. These light sources could remain in the detector and periodically flashed to continuously obtain calibration data. It would be interesting to develop methods of fitting for the light attenuation and Rayleigh scattering parameters using these data. In order to do that additional studies using simulated data should be carried out to better understand what we might be able to achieve.

REFERENCES

[1] Paul A. M. Dirac. The quantum theory of the electron. *Proc. Roy. Soc. Lond.*, A117:610–624, 1928.

[2] F. W. Stecker. The Matter - antimatter asymmetry of the universe. *14th Rencontres de Blois on Matter - Anti-matter Asymmetry Chateau de Blois, France, June 17-22, 2002*, pages 5–14, 2002.

[3] A. D. Sakharov. Violation of CP Invariance, C asymmetry, and baryon asymmetry of the universe. *Pisma Zh. Eksp. Teor. Fiz.*, 5:32–35, 1967. [Usp. Fiz. Nauk161,no.5,61(1991)].

[4] David Griffiths. *Introduction to Elemtary Particles*. Wiley VCH Verlag GmBH, 2008, 2 edition, (2008).

[5] Klaus Winter. *Wolfgang Pauli's Public Letter(1930) reprinted in 1990*. Cambridge University Press, 2 edition, (2000).

[6] James Chadwick. The existence of a neutron. *proceedings of Royal Society*, 136:692–708, (1932).

[7] Raymond Davis, Harmer Don S., and KennethC. Hoffman. search for neutrinos from the sun. *Physical Review Letters*, 20:1205–1209, (1968).

[8] Ziro Maki, Masami Nakagawa, and Shoichi Sakata. Remarks on the unified model of elementary particles. *Prog. Theor. Phys.*, 28:870–880, 1962. [,34(1962)].

[9] B.Pontecorvo V.Gribov. Neutrino astronomy and lepton charge. *Phys. Lett. B*, 28:493–496, (1969).

[10] W.Hampel et al. Gallax, solar neutrino observations. *Physical Review Letters*, 447:127–133, (1999).

[11] SAGE collaboration:J.N.Abdurashitov et al. Measurement of solar neutrino capture rate. *J.Exp.Theor.Phys.*, 447:181–193, (2002).

[12] K. S. Hirata. Observation of $^{8}\mathrm{B}$ solar neutrinos in the kamiokande-ii detector. *Phys. Rev. Lett.*, 63:16–19, (1989).

[13] K. S. Hirata. Real-time, directional measurement of $^{8}\mathrm{B}$ solar neutrinos in the kamiokande ii detector. *Phys. Rev. D*, 44:2241–2260, 1991.

[14] Q. R. Ahmad. Direct evidence for neutrino flavor transformation from neutral-current interactions in the sudbury neutrino observatory. *Phys. Rev. Lett.*, 89:011301, (2002).

[15] M. V. Diwan, V. Galymov, X. Qian, and A. Rubbia. Long-Baseline Neutrino Experiments. *Ann. Rev. Nucl. Part. Sci.*, 66:47–71, 2016.

[16] K. Suzuki et al. Measurement of the muon beam direction and muon flux for the T2K neutrino experiment. *PTEP*, 2015(5):053C01, 2015.

[17] K. Abe et al. Measurement of Neutrino Oscillation Parameters from Muon Neutrino Disappearance with an Off-axis Beam. *Phys. Rev. Lett.*, 111(21):211803, 2013.

[18] P. A. Amaudruz et al. The T2K Fine-Grained Detectors. *Nucl. Instrum. Meth.*, A696:1–31, 2012.

[19] N. Abgrall et al. Time Projection Chambers for the T2K Near Detectors. *Nucl. Instrum. Meth.*, A637:25–46, 2011.

[20] A. Kaboth. Systematic Uncertainties at the T2K Experiment for Oscillation Measurements. *arXiv*, 2013.

[21] K. Abe et al. The T2K Experiment. *Nucl. Instrum. Meth.*, A659:106–135, 2011.

[22] et al. Beavis D. Brookhaven National Laboratory Report No. BNL-52459. *unpublished*, 1995.

[23] (T2K Collaboration). Search for cp violation in neutrino and antineutrino oscillations by the t2k experiment with 2.2×10^{21} protons on target. *Phys. Rev. Lett.*, 121:171802, Oct 2018.

[24] K. Abe et al. Letter of Intent: The Hyper-Kamiokande Experiment — Detector Design and Physics Potential —. *arXiv*, 2011.

[25] S. Bhadra et al. Letter of Intent to Construct a nuPRISM Detector in the J-PARC Neutrino Beamline. *unpublished*, 2014.

[26] Melanie Day and Kevin S. McFarland. Differences in Quasi-Elastic Cross-Sections of Muon and Electron Neutrinos. *Phys. Rev.*, D86:053003, 2012.

[27] Mark Scott. An Intermediate Water Cherenkov Detector at J-PARC. *JPS Conf. Proc.*, 12:010039, 2016.

[28] Hyper-Kamiokande Working Group. A long baseline neutrino oscillation experiment using j-parc neutrino beam and hyper-kamiokande, 2014.

[29] K. Abe. Measurements of neutrino oscillation in appearance and disappearance channels by the t2k experiment with 6.6×10^{20} protons on target. *Phys. Rev. D*, 91:072010, Apr 2015.

[30] Alexandar Jaffray. Photosensor test facility operations manual.

[31] Re edited by S-O Flyckt and Carole Marmonier. Photomultiplier tubes principles & applications, 2002.

[32] Kevin Sing Xie. 20-inch sk-pmt plots for ptf.

[33] Johannes Hoppenau Joseph Lozier Thomas Dealtry, Alexander Himmel. Simulating water cherenkov detectors using wcsim, 2016.

[34] WCSim code. Geant4.10.02.

[35] Hamamatsu. 3-inch pmt r12199_02.

[36] Tomoyo Ushida. Development of detector simulation and event reconstruction for j-parc e61 experiment.

[37] WCSim LEDbranch. Geant4.10.02.

[38] CERN by Fred James. minuit2, 1975-1980.

[39] CERN programming team. Root 5.34/36, 2016.

[40] WCSim. Wcsim source files.

[41] The editors of Encyclopaedia Britannica. Rayleigh scattering.

APPENDIX A

FIRST APPENDIX

Table for Geant4 commands.

Table 4.1

Sr. no.	Geant4 commands	Used to get:
1	GetTrigger(int i)	i number of triggers.
2	GetNumberOfEvents()	total observed triggers.
3	GetNumberOfSubEvents()	total number of sub-event triggers.
4	HasSubEvents()	For more than one trigger.
5	GetHeader()	the header with run and event number.
6	GetTriggerType()	the trigger type enumeration.
7	GetTriggerInfo()	the additional trigger information.
8	GetPi0Info()	the Pi0 information to be stored in the macro file, if needed.
9	GetMode()	the interaction mode code number.
10	GetVtx(int i)	the event vertex, 0=x, 1=y, 2=z.
11	GetNPar()	the number of true particles.
12	GetNTrack()	the number of true particle tracks.
13	GetTracks()	TClonesArray of true particle tracks.
14	Get NumTubeHit()	the number of tubes with a true hit.
15	GetNCherenkovHits()	the true PMT hits in each PMT.
16	GetNCherenkovHittimes()	the number of true hits.

Table 4.1		
Sr. No.	Geant4 commands	Used to get:
17	GetCherenkovHitTimes()	the true times of all the hits.
18	GetNCherenkovDigihits()	the number of digitized hits.
19	GetSumQ()	the sum of digitized charge.
20	GetCherenkovDigiHits()	the digitized hits e.g. charge read out by the simulated electronics.
21	GetNcherenkovhits()	the number of true cherenkov hits.
22	GetTotalPe(0)	the position in the array of HitTimes.
23	GetTotalPe(1)	the number of true photons that hit the PMT.
24	GetTubeID()	the tube ID number.
25	GetTrueTime()	the true time of the hit.
26	GetParentID()	the ID number of parent particle to trace a true particle.
27	GetQ()	the total charge measured by the PMT.
28	GetT()	the measured time of the hit.
29	GetPhotonsIds()	the raw hits that contributed to the digit.
30	GetTubeId()	the ID number of the PMT.
31	GetCylLoc()	0 for a PMT on the top cap, 2 for PMT on thr bottom and 1 for a PMT on the wall.
32	GetPosition(j)	the coordinated of the center of the sphere that forms the PMT. j=0, 1, 2 represents the x, y and z -axis respectively.
33	GetOrientation(j)	the vector describing the direction of the PMT. j=0, 1, 2 returns the x, y and z components respectively.